UNIVERSIDAD DE CHILE
FACULTAD DE CIENCIAS FÍSICAS Y MATEMÁTICAS
DEPARTAMENTO DE INGENIERÍA ELÉCTRICA

ASSEMBLY, INTEGRATION AND VERIFICATION OF AN ASTRONOMY EXPERIMENT FOR GALACTIC FAST RADIO BURST DETECTION

TESIS PARA OPTAR AL GRADO DE MAGISTER EN CIENCIAS DE LA INGENIERÍA,
MENCIÓN ELÉCTRICA

FRANCISCA ANDREA SOLÍS GARRIDO

PROFESOR GUÍA:
RICARDO FINGER CAMUS

MIEMBROS DE LA COMISIÓN:
TOMÁS CASSANELLI ESPEJO
MARILYN CRUCES CRUCES

Este trabajo ha sido parcialmente financiado por ANID bajo los subsidios de Basal ACE210002, FB210003 and FONDECYT 1221662.

SANTIAGO DE CHILE
2024

RESUMEN DE LA TESIS PARA OPTAR
AL GRADO DE MAGISTER EN CIENCIAS DE LA INGENIERÍA,
MENCIÓN ELÉCTRICA
POR: FRANCISCA ANDREA SOLÍS GARRIDO
FECHA: 2024
PROFESSOR GUÍA: RICARDO FINGER CAMUS

ENSAMBLE, INTEGREACIÓN Y VERIFICACIÓN DE UN EXPERIMENTO ASTRONÓMICO PARA LA DETECCIÓN DE RÁFAGAS RÁPIDAS DE RADIO GALÁCTICAS.

Los telescopios del mundo están dedicados a la observación y estudio de diferentes fenómenos de interés astronómico, tales como búsqueda de planetas, agujeros negros, galaxias, etc. En Chile, no hay tecnología dedicada a la búsqueda y análisis de ráfagas rápidas de radio (*fast radio bursts*, FRB) en tiempo real.

Las FRBs se caracterizan por poseer corta duración del orden de los ms y alto flujo de densidad espectral ∼100 Jy (1 Jy = 10^{-26} Wm^{-2} Hz^{-1}). Se observan como pulsos de alta energía que barren un determinado ancho de banda en un breve instante de tiempo.

Esta tesis pretende ensamblar e integrar equipos desarrollados específicamente para la búsqueda, análisis y detección en tiempo real de FRBs Galácticas.

Astronomical Radio Transients Experiment (ARTE) es el nombre que recibe el radiotelescopio diseñado para seguir el centro de la Galaxia, en busca de FRBs. El objetivo es poner en marcha una versión mejorada del *Survey for Transient Astronomical Radio Emission* 2 (STARE2) [1].

La primera luz fue al detectar una llamarada solar reportada por el *Expanded Owens Valley Solar Array* (EOVSA) [2], el 09-05-2023T18:58:00, con densidad de flujo superior a 10^4 kJy, además de tránsitos de satélites, radares y diferentes eventos de interferencia de radiofrecuencias (RFI).

RESUMEN DE LA TESIS PARA OPTAR
AL GRADO DE MAGISTER EN CIENCIAS DE LA INGENIERÍA,
MENCIÓN ELÉCTRICA
POR: FRANCISCA ANDREA SOLÍS GARRIDO
FECHA: 2024
PROFESSOR GUÍA: RICARDO FINGER CAMUS

ASSEMBLY, INTEGRATION AND VERIFICATION OF AN ASTRONOMY EXPERIMENT FOR GALACTIC FAST RADIO BURST DETECTION

Telescopes in the world are dedicated to the observation and study of different phenomena of astronomical interest, such as the search for planets, black holes, galaxies, etc. Chile has no technology dedicated to the search and analysis of fast radio bursts (FRB) in real-time.

FRBs are characterized by having a short duration of the order of milliseconds and a high flux density $\sim$100 Jy (1 Jy $= 10^{-26}$ Wm^{-2} Hz $^{-1}$). They can be observed as high-energy pulses which sweep a certain bandwidth in a short instant of time.

This thesis seeks to assemble and integrate equipment specifically developed for the search, analysis, and real-time detection of FRBs, particularly Galactic events. Astronomical Radio Transients Experiment (ARTE) is the name given to the radio telescope designed to track the Galactic center in search of FRBs. The goal is to implement and commission an improved version of Survey for Transient Astronomical Radio Emission (STARE2) [1].

Our first light was a solar flare reported by the Expanded Owens Valley Solar Array (EOVSA) [2], on 09-05-2023T18:58:00, of a flux density higher than 10^4 kJy. In addition, satellites, radars, and many events like RFI have been detected.

To the little girl, I was

Acknowledgments

I would like to thank my professor Ricardo Finger, who gave me the opportunity and support to study and work in a different field of electronics, which I have no previous experience in. And gave me the challenging responsibility of being the engineer in charge of the ARTE radio telescope.
I am very thankful for my committee, composed by Tomás Cassanelli and Marilyn Cruces, who were always open to sharing their knowledge and experience in a very proactive way with me.

I want to thank my coworkers at the millimeter wave laboratory (MWL), Sebastián Antonio, Max Prieto [1], Diego, Camilo Espinoza, Pascualito, Diana, David, Franco, Rafa, Felipe, Walter and Leo. A special thanks to Joaquin Alfredo Alfonso. Thanks to the mechanical engineering team José, Camilo, and Juan, for their help.

I want to give a special thanks to Steven, who developed ARTE detection algorithm during his internship.

I would like to thank the Calán Football Association, for the assistance and for letting me be the goal scorer... sometimes.

Finally, I want to thank my family and friends, for their unconditional support.

This work was supported by the Chilean National Agency for Research and Development (ANID) through its grants Basal ACE210002, FB210003, and the National Fund for Scientific and Technological Development FONDECYT 1221662.

---

[1] https://n9.cl/cjip9

Table of Content

List of Tables

List of Figures

Chapter 1

Introduction

1.1 Motivation

In 2007 Duncan Lorimer [8], discovered the first fast radio burst (FRB), which opened a new area of study for the scientific community. Over time, these signals have remained a subject of interest for researchers. More than 600 FRBs [9] [10] have been documented to date, yet their origins and mechanisms remain largely unknown.

FRBs are characterized by their brief, millisecond-scale durations, and high spectral density flux, typically around $\sim$100 Jansky (1 Jy = 10^{-26} Wm^{-2} Hz^{-1}). These bursts appear as short-lived, high-energy pulses spanning a wide spectrum from frequencies lower than 400 MHz to 8 GHz [11]. Additionally, due to their passage through ionized media, these signals undergo dispersion.

Two key factors motivate this research. First, the absence of Chilean radio telescopes dedicated to real-time FRB detection. The second is limited knowledge of their origins. In this way, detecting these kinds of signals gives information about the magnetars, the Milky Way, and the radio sky and at the same time enriches scientific knowledge. Moreover, when charged particles travel through a curved path, they emit electromagnetic radiation which is called synchrotron radiation and it is the principal source of knowledge of the interstellar medium magnetic properties.

ARTE seeks to observe the Milky Way in search of Galactic FRBs. Stronger signals are expected due to its proximity to the observation points, which allows the use of smaller antennas, among other benefits. Estimates suggest that FRBs occur frequently, in the hundreds to thousands each day per full sky. Although they often occur, unlike pulsars, FRBs lack a consistent periodic pattern and are not known to repeat except in rare cases such as the FRB 20190520B [12].

Unlike STARE2, which employs horn antennas to probe a wide expanse of the sky, with the drawback of compromised accuracy in determining source position due to temporal variations in phase between distant antennas, ARTE presents an innovative approach. ARTE uses a single antenna, composed of three subarrays, two of them align their radiation pattern with the central region of the Milky Way for detection. On the other hand, ARTE has a third subarray, which lets the source localization.
This choice not only saves financial resources but also significantly strengthens our ability to

determine the origin of the detected signals.

1.2 Background

Radio astronomy is a subdiscipline of astronomy focused on the detection, analysis, and interpretation of radio emissions from celestial objects (from $\sim$ 20MHz above 950GHz). These radio signals are a form of electromagnetic radiation that falls outside the visible spectrum as shown in 1.1 and is, therefore, not detectable by the human eye.

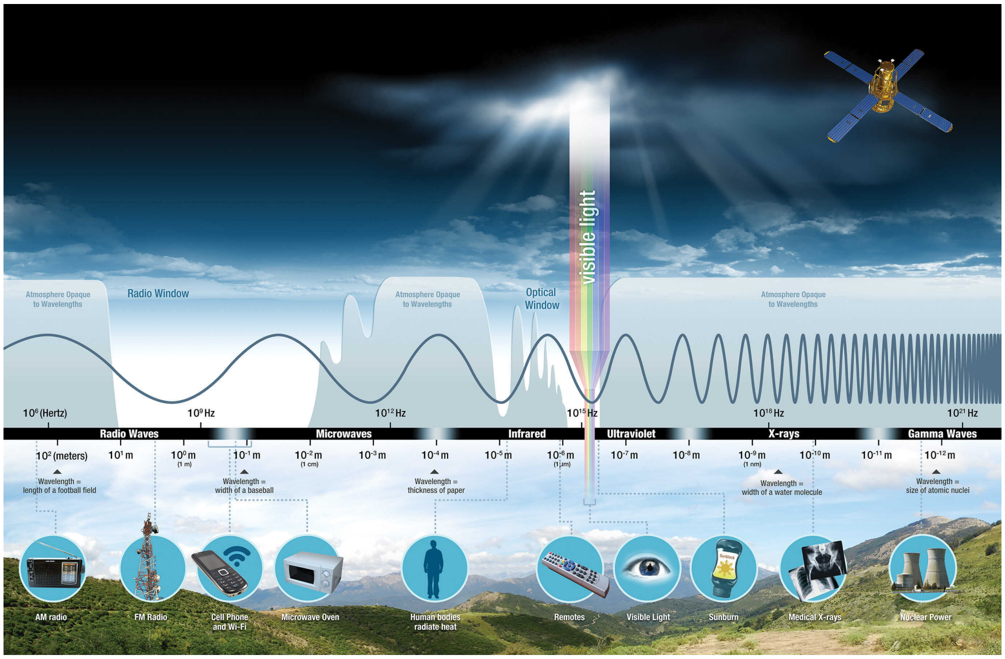

Figure 1.1: In its simplest form, the electromagnetic spectrum is a diagram that displays electromagnetic radiation at various frequencies, along with their corresponding wavelengths. Typically, these are arranged from the shortest wavelength (radio waves) to the longest (γ- rays). Additionally, the Earth's atmosphere acts as a selective filter, allowing certain frequencies to pass through while blocking others [13].

To observe and study these signals, radio astronomers employ specialized instruments known as radio telescopes. These instruments are designed to detect and record radio waves emitted by various radio sources, including galaxies, energetic quasars, pulsars, and even the cosmic microwave background radiation.

Each of these radio sources emits radio waves in a unique way, providing valuable insights into their composition, motion, and physical properties. Radio astronomy allows us to characterize and better understand these objects through their radio emissions, expanding our knowledge of the Universe.

In radio astronomy, the operation of telescopes is based on the radiometer equation, a fundamental formula that allows quantifying the signals received by radio telescopes from astronomical sources. In this equation, the conditions of the observing system and the noise present in the measurement are considered.

The equation is given by the following expression [14]:

$$\Delta \mathrm{T} = \frac{\mathrm{k_c} \cdot \mathrm{T_{sys}}}{\sqrt{(2\Delta\nu\tau)}} \tag{1.1}$$

Where,

1. $\Delta \mathrm{T}$: Corresponds to the intrinsic noise temperature standard deviation.
2. $\mathrm{T_{sys}}$: It's the system temperature, which includes all components of the observing system. Generally, it corresponds to the receiver temperature and the rest of the elements. It is measured in Kelvin. $\mathrm{T_{sys}} = \mathrm{T_{rx}} + \mathrm{T_a}$
3. $\Delta\nu$: This is the effective bandwidth of the radio telescope, i.e., the observing frequency range.
4. τ : Corresponds to the integration time.

Another important relation is given by:

$$\mathrm{SNR} = \frac{\mathrm{T_a}}{\Delta \mathrm{T}} \tag{1.2}$$

Where,

1. SNR: Corresponds to the signal-to-noise ratio.
2. $\mathrm{T_a}$: Corresponds to antenna temperature.

1.3 Description of the general problem

Based on the radiometer equation outlined in reference 1.1, it becomes evident that the attainment of a favorable noise temperature standard deviation necessitates the optimization of specific parameters, such as the observation bandwidth and the integration time. Additionally, a high system noise temperature can have a detrimental impact on $\Delta \mathrm{T}$ affecting the overall observation quality.

The signal-to-noise ratio (SNR) is a crucial metric to consider for valid detection and for quantifying the quality of the observation. Following this logic, when dealing with a weak signal, one can enhance SNR by increasing the integration time. However, in the case of transient events, the integration time can be dominated by noise, rendering the signal undetectable to the system.

Fast Radio bursts are signals that suffer temporal dispersion due to their interaction with the intervening medium, resulting in a temporal sweep where higher frequencies arrive before lower frequencies, this characteristic is called Dispersion Measure (DM)[15].

ARTE has been designed to employ the method of incoherent dedispersion. In simple terms, it compensates for the dispersion effect by dividing the incoming frequencies into different independent frequency channels using a spectrometer. To each of these channels, a temporal delay is applied so that the pulse reaches the output of each channel simultaneously. This results in the attainment of a distinctive power peak that stands out above the system noise [15].

The delays can be calculated using the following expression, which depends on the DM and the dispersion constant $\mathcal{D}$ [16].

$$\Delta \mathrm{t} \simeq 4.1488 \cdot 10^{6} \cdot \left(\mathrm{f}_{\mathrm{ref}}^{-2} - \mathrm{f}_{\mathrm{chan}}^{-2}\right) \cdot \mathrm{DM} \tag{1.3}$$

1.4 Hypothesis

This work is carried out under two important premises.

1. The radio telescope will be able to operate with sufficient sensitivity to detect Galactic FRBs such as the one reported by STARE2, in addition to being able to detect in real-time due to the parallelization capability of the Field Programmable Gate Arrays (FPGA).
2. An appropriate behavior will be obtained by the time of integration of each subsystem as a whole system.

1.5 Objectives

1.5.1 General objective

The general objective of this thesis work is to assemble, integrate, and verify a centimeter wavelength, wide field-of-view (FoV) radio telescope for the detection of bright radio transient phenomena.

1.5.2 Specific objectives

1. Development of a calibration hot/ambient noise source.
2. Characterization of hardware at a component, subsystem, and system level.
3. Integration of the antenna arrays, noise source, mount, front end, and back end subsystems.
4. Develop and integrate observing for telescope pointing, receiver control, and data acquisition.
5. Telescope commissioning and first demonstration observations.

1.6 Outline of this thesis

- Chapter 2 first presents a summary of the state-of-the-art, briefly describing what a fast radio burst is and a description of STARE2. The project that has been the source of inspiration for the development of ARTE. In addition, certain fundamental concepts are explained to provide the reader a basic understanding of the thesis.
- Chapter 3 presents the development of the assembly and integration process of each of the subsystems, detailing, and characterizing the system and results of the different tests to which it was submitted to evaluate its performance.

- Chapter 4 deals with problems that occurred during the commissioning, documented to avoid their repetition in the future.
- Chapter 5 shows the early results obtained from stable operation during months of observation.
- Chapter 6 presents general conclusions about the work carried out, emphasizing future work.

Chapter 2

Literature Review

2.1 Fast radio burst

Fast radio bursts [1] (FRBs) are exceedingly bright pulses, with spectral flux densities ranging from 50 mJy to 100 Jy, characterized by extremely short durations, often on the order of ms or less. They have been observed across a broad portion of the electromagnetic spectrum, spanning from 400 MHz to 8 GHz (Petroff, [11]). Despite their unknown origins, their behavior, reminiscent of pulsars, suggests an association with highly energetic astrophysical phenomena, primarily linked to celestial bodies such as compact stars. Furthermore, these signals undergo temporal dispersion due to their interaction with the intervening medium, resulting in a temporal sweep where higher frequencies arrive before lower frequencies, a phenomenon shown in Figure 2.1.

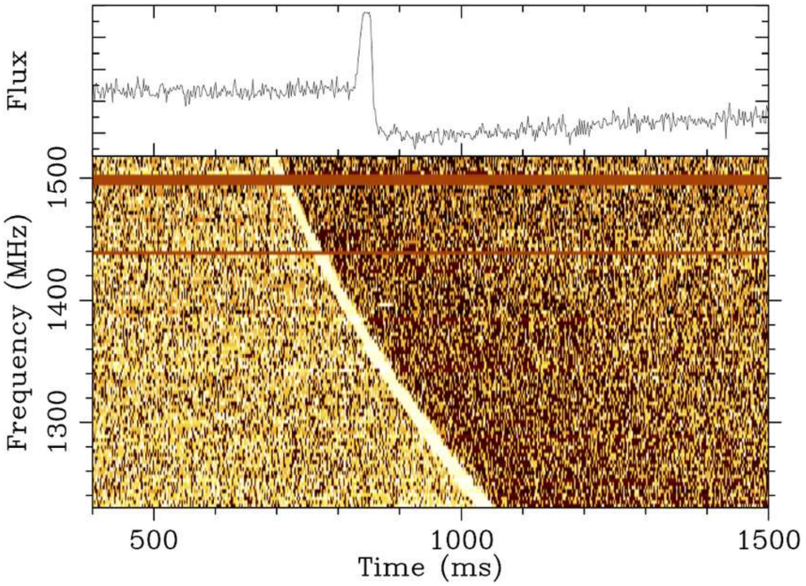

Figure 2.1: The Lorimer burst, also known as FRB 010724([8]).

In Figure 2.1 upper panel, the signal resulting from the summation encompassing all recorded frequencies is depicted. Following the occurrence of the phenomenon, there was a perceptible

---

[1] https://www.chime-frb.ca/catalog

decrease in power, which manifested itself as a reduction in background noise. This effect was mainly attributed to the signal strength, which caused the detector to saturate. The lower panel shows a spectrogram (dynamic spectra) in which color variations indicate the intensity of the event relative to the background noise. In addition, lines through the spectrogram denote areas contaminated by radio frequency interference (RFI). Consequently, their contribution is mitigated by frequency elimination procedures for the entire observation time [11].

2.1.1 Dispersion

2.1.2 Dispersion measure

Dispersion is the physical phenomenon that occurs when an electromagnetic signal passes through the ionized plasma that makes up the interstellar medium (ISM) or intergalactic medium (IGM), creating a relationship between the refractive index and the frequencies involved, both the signal and the plasma. In this way, a temporal variation in the arrival of the signal occurs, dependent on frequency, such that lower-frequency radio waves experience more significant delays compared to higher-frequency ones.

The frequency of the plasma is expressed as follows:

$$\mathrm{f_p} = \sqrt{\frac{\mathrm{e^2 n_e}}{\pi \mathrm{m_e}}} \tag{2.1}$$

Where,

- e: Corresponds to electron charge.
- $\mathrm{n_e}$: Corresponds to the electron number density.
- $\mathrm{m_e}$: Represent the electron mass.

Furthermore, it can be noted that the refractive index can be expressed as a function of both frequencies,

$$\mu = \sqrt{1 - \left(\frac{\mathrm{f_p}}{\mathrm{f}}\right)^2} \tag{2.2}$$

Subsequently, if we consider a propagation velocity given by:

$$\mathrm{v_g} = \mathrm{c} \cdot \mu \tag{2.3}$$

It is possible to obtain the time difference between a signal traveling a path of length 'd' compared to a signal of infinite frequency.

$$\mathrm{t} = \int_0^{\mathrm{d}} \frac{\mathrm{dx}}{\mathrm{v_g}} - \frac{\mathrm{d}}{\mathrm{c}} \tag{2.4}$$

$$\mathrm{t} = \int_0^{\mathrm{d}} \frac{\mathrm{dx}}{\mathrm{c}\sqrt{1 - \left(\frac{\mathrm{f_p}}{\mathrm{f}}\right)^2}} - \frac{\mathrm{d}}{\mathrm{c}} \tag{2.5}$$

$$t = \frac{1}{c}\int_0^d \left[1 + \frac{f_p^2}{2f_p^2}\right] dx - \frac{d}{c} \tag{2.6}$$

$$t = \frac{e^2}{2\pi m_e c} \cdot \frac{\int_0^d n_e dx}{f^2} \equiv \mathcal{D} \cdot \frac{DM}{f^2} \tag{2.7}$$

Lastly, it follows from 2.6 that:

$$\mathcal{D} = \frac{e^2}{2\pi m_e c} \approx 4.1488 \cdot 10^3 \tag{2.8}$$

$$DM = \int_0^d n_e dx \tag{2.9}$$

For more details about de dispersion constant $\mathcal{D}$ see [16].

2.1.3 Dispersion time

Therefore, the results presented in 2.8 and 2.9 are extended for the calculation of delay between two frequencies, f_{ref} and f_{chn}, both in MHz.

$$\Delta t \simeq 4.1488 \cdot 10^6 \cdot \left(f_{ref}^{-2} - f_{chan}^{-2}\right) \cdot DM \tag{2.10}$$

In this manner, it becomes possible to calculate the delay experienced by a specific pulse when comparing one frequency to another. It is worth noting that this delay is determined by the dispersion measure (DM).

Another application of this expression is to estimate the dispersion measure value based on a known delay for certain frequencies. Understanding the Dispersion Measure (DM) of an arriving pulse allows us to infer the source's distance, assuming a known electron density distribution.

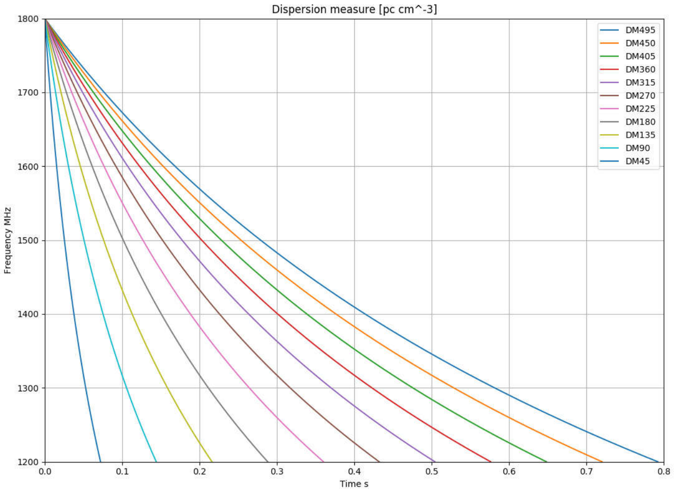

Figure 2.2: Dispersion measure curves

Using equation 2.10, it is possible to visualize various dispersion curves in Figure 2.2 for the desired dispersion measures (DM) and bandwidths. The image displays eleven curves representing the implemented dispersion measures in ARTE Back-End, all plotted for a bandwidth of 600 MHz within the operational frequency range.

2.1.4 Incoherent dedispersion

As previously discussed, the interaction of electromagnetic signals with the medium they traverse gives rise to the dispersion phenomenon outlined in the preceding subsections. To mitigate this phenomenon, various techniques are available, one of which is incoherent dedispersion, the focus of this section.
This technique operates by dividing the frequency band into multiple independent channels, requiring the use of a spectrometer. Subsequently, for each of the obtained frequencies, a time delay is applied, ensuring that for each post-delay frequency, the arrival of each frequency is observed within the same channel ([15]).

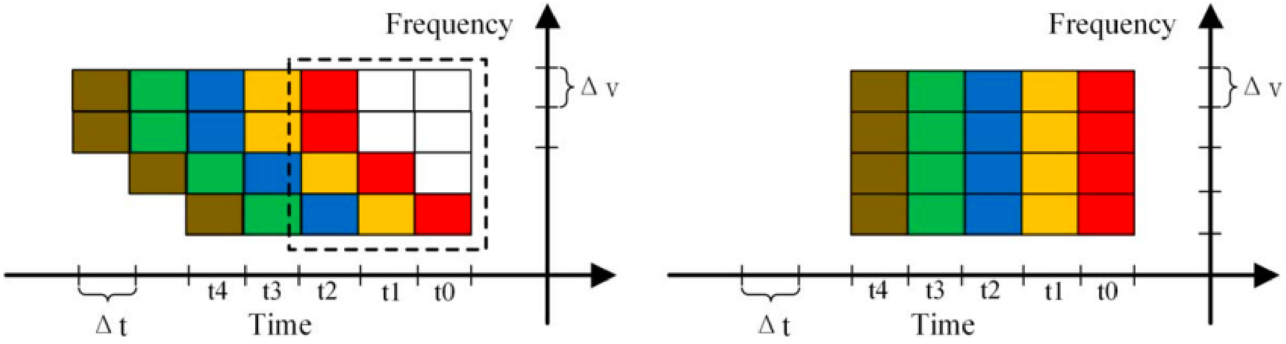

Figure 2.3: An illustrative example of the incoherent dedispersion technique.

In Figure 2.3, each colored block represents different spectral channels at various time instances. Left: A time-frequency plot is displayed, showing a dispersed signal. Right: By applying a delay proportional to Δt, dependent on the frequency of the signal, it becomes possible to obtain a completely undispersed signal within the same time interval [17].

2.2 ROACH

ROACH, an acronym for Reconfigurable Open Architecture Computing Hardware, is a reconfigurable hardware platform developed by the University of California, Berkeley. Its primary objective was to empower researchers to program digital circuits in real time for the analysis and processing of predominantly radiofrequency data. This platform comprises Field Programmable Gate Arrays (FPGAs), Analog to Digital Converters (ADCs), processors, PowerPC subsystem, and 10GBe (with CX4 mezzanine card), among other components.

In this particular case, ROACH2 was utilized, which is the second-generation version of the ROACH1 board (Xilinx Virtex-5 FPGA). ROACH2 is equipped with Xilinx Virtex-6 FPGA, offering improved performance in terms of processing capabilities and memory bandwidth, furthermore, it includes a unified JTAG interface provided through an FTDI FT4232H IC[2].

In Figure 2.4, the key components of the utilized board, which are mentioned below, are highlighted within yellow boxes.

1. Analog-Digital Converters (2 ZDOKs docking connectors).

---

[2] https://casper.astro.berkeley.edu/wiki/ROACH2

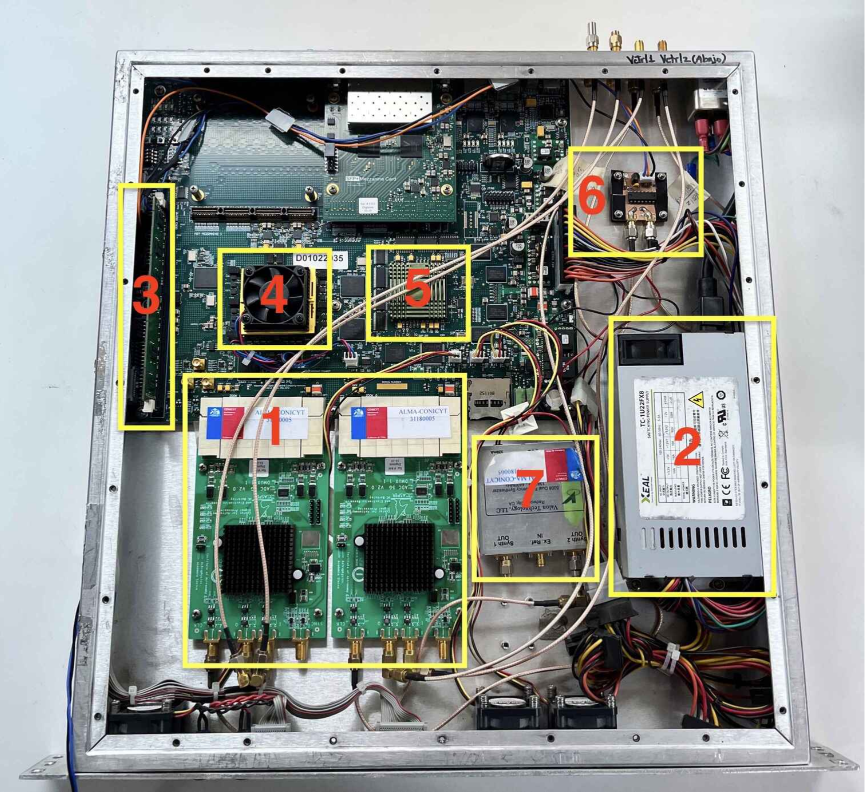

Figure 2.4: ROACH2 board with some key components highlighted in yellow boxes

2. Switching Power Supply Unit TC-1U22FX8.
3. A single 72-bit DDR3 RDIMM slot connected to the FPGA.
4. Virtex-6 SX475T FPGA (XC6VSX475T-1FFG1759C).
5. PowerPC 440EPx stand-alone processor to provide control functions.
6. Calibration switch control circuit, powered by ROACH2 GPIO.
7. Valon 5007 synthesizer to provide clock reference for ADCs.

2.2.1 FPGA

Field Programmable Gate Arrays (FPGAs) are integrated circuits distinct from conventional ones, as they are not pre-programmed at the factory. These chips contain programmable integrated circuits equipped with Configurable Logic Blocks (CLBs), known as logic cells, which can be interconnected as per the programmer's specific requirements through routing channels, as shown in Figure 2.5. Additionally, they have input and output pads that allow them to communicate with the external environment by receiving or sending signals.

The programmability of these arrays of logic gates provides greater flexibility in designing customized circuits, allowing for hardware modifications as needed, ranging from simple digital operations to complex digital signal processing circuits. They are configured using hardware description languages (HDL), such as HDL, VHDL acronym resulting from combining VHSIC (Very High-Speed Integrated Circuit) and HDL, or Verilog.

These FPGAs are characterized by their high computing capability, which is achieved through parallelization, as each logic block can operate independently. Moreover, they include other valuable resources, such as RAM blocks, high-speed multipliers, Analog-to-Digital Converters (ADCs), Phase-Locked Loops (PLLs), and more.

Regarding the programming of the FPGA in the context of the ARTE project, it was primarily accomplished using graphical programming tools based on Simulink, utilizing libraries developed by CASPER (Collaboration for Astronomy Signal Processing and Electronics Research). CASPER is a collaborative group that provides open-source resources to the community for electronic research and the digital signal processing of astronomical signals, as its name suggests.

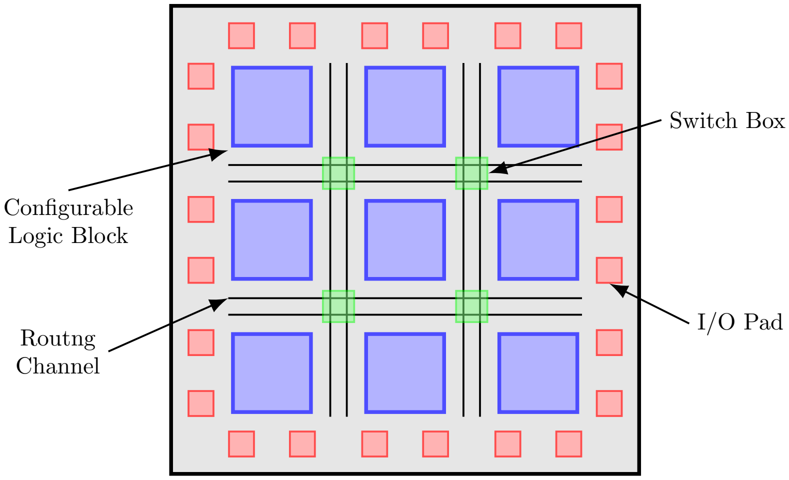

Figure 2.5: FPGA diagram [18]

2.3 Astronomical facilities

2.3.1 CHIME

The CHIME Telescope is located at the Dominion Radio Astrophysical Observatory, operated by the National Research Council of Canada.

The Canadian Hydrogen Intensity Mapping Experiment (CHIME) is an interferometric radio telescope initially designed to map hydrogen, the element with the highest prevalence in the universe, to generate a density map of this element. By analyzing these signals, it becomes possible to detect transient phenomena, such as Fast Radio Bursts (FRBs) or pulsars.

CHIME comprises four contiguous cylindrical reflectors, as illustrated in Figure 2.6. It operates within a frequency range spanning from 400 MHz to 800 MHz and provides an expansive field of view, covering approximately 200 square degrees.

To perform the search for Fast Radio Bursts (FRBs), CHIME continuously scans 1024 points in the sky. It operates at a sampling rate of 1 ms and additionally has 16,000 frequency channels.

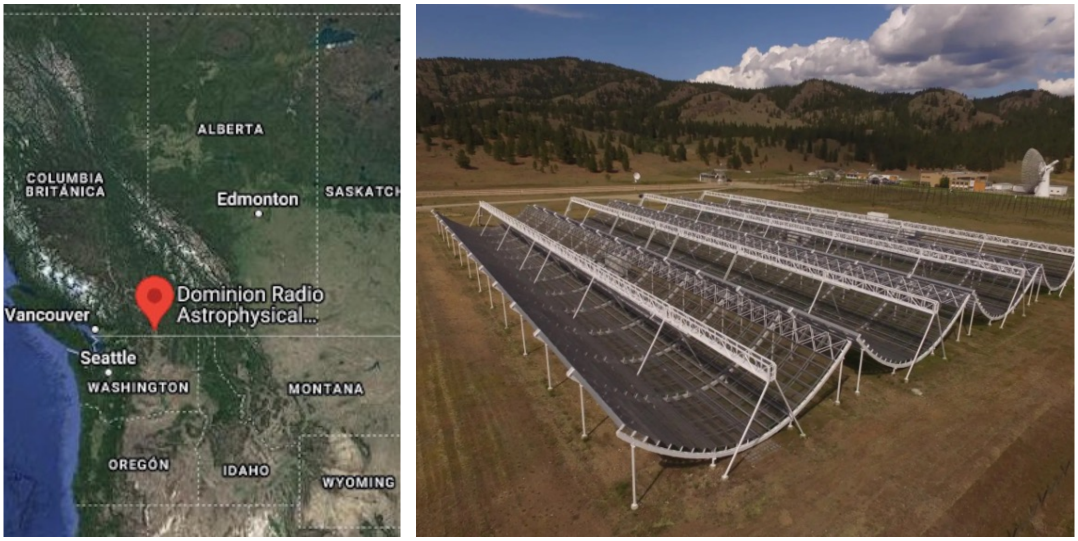

Figure 2.6: Left: Location map[19]. Right: The Canadian Hydrogen Intensity Mapping Experiment (CHIME) radio telescope.

As of 2020, it has detected more than 1,000 sources of FRBs.

2.3.2 STARE2

The project, Survey for Transient Astronomical Radio Emission 2 (STARE2) [1], is a collaborative research endeavor in the field of radio astronomy dedicated to the real-time detection and study of fast radio bursts (FRBs). It aims to contribute to the understanding of FRBs.

Their radio telescopes were designed to operate at low frequencies with a narrow bandwidth of 188 MHz, enabling the detection of transients out to 7 Mpc. The project operated for 18 months, covering 1546 different Dispersion Measures (DMs) ranging from 5 to 3000 $pc\ cm^{-3}$ and was sensitive to 1-millisecond transients with flux densities above 300 kJy.

To achieve this, zenith observations were conducted using two dual-polarization ring feeders positioned at the Owens Valley Radio Observatory (OVRO) and the Venus antenna at the Goldstone Deep Space Communications Complex (GDSCC) in the northeastern United States, as is shown in Figure 2.7.

Regarding Radio Frequency Interference (RFI) mitigation, a multi-station coincidence approach was employed to filter out unwanted interference signals.

Finally, the STARE2 telescopes reported an FRB-like event originating from the Milky Way, specifically from the magnetar SGR (soft gamma repeater) 1935+2154 [20].

Building on STARE2, another project similar to ARTE is the Galactic Radio Explorer (GReX), an all-sky monitor for searching fast radio bursts emitted from Galactic magnetars or nearby galaxies [21].

Figure 2.7: Left: The green zones, OVRO and Goldstone, represent operational sites with a travel time between them of 0.86 seconds. The red zones, on the other hand, are potential sites for future operational stations. Right: Choke-ring feed located at OVRO [1].

2.3.3 GMRT

The Giant Metrewave Radio Telescope (GMRT), is an array of parabolic radio telescopes located in Pune, India [22].

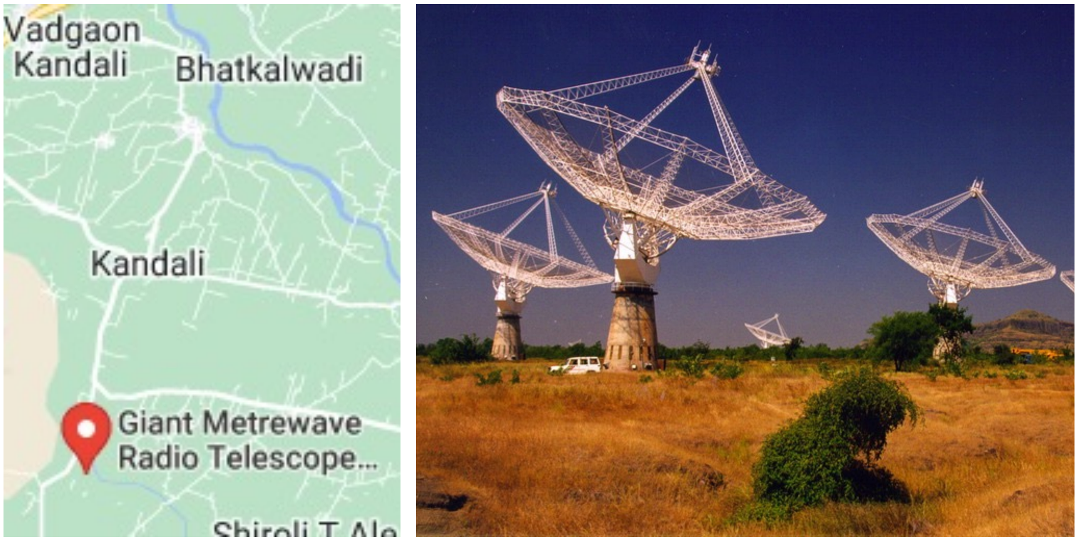

Figure 2.8: Left: Location map. Right: The Giant Metrewave Radio Telescope (GMRT)[22].

This observatory consists of an array of thirty fully steerable parabolic radio telescopes, each with a 45-meter diameter and sensitivity to metric wavelengths. It is situated 80 kilometers north of Pune, specifically in Junnar, Narayangaon, India, and is managed by the National Centre for Radio Astrophysics (NCRA).

Its receivers were upgraded, resulting in what is now known as the upgraded GMRT (uGMRT). The uGMRT has reported the detection of 15 bursts from the Fast Radio Burst 180916.J0158+65, which exhibits a 16.35-day periodicity [23]. The source was observed within a bandwidth of 550-750 MHz for two hours during three cycles, yielding varying quantities of bursts, each an order of magnitude higher in energy compared to the Galactic burst source SGR 1935+2154.

2.3.4 EOVSA

The Expanded Owens Valley Solar Array (EOVSA) is an astronomical radio telescope comprised of 15 antennas mounted in altitude-azimuth configuration, operating in microwave radio frequencies ranging from 1 to 18 GHz. Located at the Owens Valley Radio Observatory (OVRO) near Big Pine, California. EOVSA is managed by the New Jersey Institute of Technology (NJIT), which also oversees the Big Bear Solar Observatory [3]. It is funded by the National Science Foundation as part of the Geospace Facilities program.

EOVSA primarily focuses on the study of solar physics, aiming to understand solar activity and related phenomena, as well as space weather [2]. Additionally, it hosts instruments dedicated to the localization of Solar Radio Bursts (SRBL), including the FASR Subsystem Testbed (FST) and the Korean SRBL (KSRBL).

Figure 2.9: Left: Location map. Right: The Expanded Owens Valley Solar Array [2].

---

[3] https://www.bbso.njit.edu/

2.4 Fundamentals

Before proceeding with the development of the thesis, it is useful to explain certain fundamental concepts that will allow a better and simpler understanding in the future.

2.4.1 Electromagnetism

Electromagnetic waves are a manifestation of energy that travels through space in the form of a wave. It is composed of electric and magnetic fields, which are characterized by being orthogonal to the direction of their propagation. Like other waves, they can be characterized by their frequency, wavelength, propagation speed, polarization, and so on.

Below, Maxwell's equations are presented, which are fundamental for understanding the relationship between magnetic and electric fields as they propagate through space. These equations, formulated by physicist James Clerk Maxwell in the 19th century, are fundamental pillars in electromagnetic theory and play a crucial role in describing a wide variety of electromagnetic phenomena [24].

$$\nabla \cdot \tilde{\mathrm{E}} = \frac{1}{\varepsilon_{\mathrm{o}}}\rho \tag{2.11}$$

$$\nabla \cdot \tilde{\mathrm{B}} = 0 \tag{2.12}$$

$$\nabla \times \tilde{\mathrm{E}} = -\frac{\partial \tilde{\mathrm{B}}}{\partial \mathrm{t}} \tag{2.13}$$

$$\nabla \times \tilde{\mathrm{B}} = \mu_{\mathrm{o}}\tilde{\mathrm{J}} + \mu_{\mathrm{o}}\varepsilon_{\mathrm{o}}\frac{\partial \tilde{\mathrm{E}}}{\partial \mathrm{t}} \tag{2.14}$$

2.4.2 Polarization

Polarization is a property of a radiated electromagnetic wave that describes the variable direction over time, along with the relative magnitude of the electric field vector. There are three types of polarization: linear, circular, and elliptical, as illustrated in Figure 2.10.

Based on Maxwell's equations presented in 2.4.1 for an electromagnetic wave, it is possible to decompose the electric field into its two orthogonal components, denoted as $\mathrm{E_x}$ and $\mathrm{E_y}$, respectively, such that:

$$\varepsilon_{\mathrm{x}} = \hat{\mathrm{a}}_{\mathrm{x}}\mathrm{E_x}\cos(\omega \mathrm{t} + \varphi_{\mathrm{x}}) \tag{2.15}$$

$$\varepsilon_{\mathrm{y}} = \hat{\mathrm{a}}_{\mathrm{y}}\mathrm{E_y}\cos(\omega \mathrm{t} + \varphi_{\mathrm{y}}) \tag{2.16}$$

From expressions 2.15, it can be observed that $\mathrm{E_x}$ represents the magnitude of the electric field in the x-direction for a wave oscillating at frequency ω with a phase shift φ_{x} in the x-direction. Similarly, it is defined for the case of 2.16 in the y-direction.

For linear polarization, there are three possible scenarios. The first scenario involves one of the two electric field components (either x or y) having zero magnitude, as follows:

For $\mathrm{E_x} = 0$,

$$\varepsilon_{\mathrm{x}} = 0 \tag{2.17}$$

$$\varepsilon_{\mathrm{y}} = \hat{\mathrm{a}}_{\mathrm{y}}\mathrm{E}_{\mathrm{y}} \cos(\omega \mathrm{t} + \varphi_{\mathrm{y}}) \tag{2.18}$$

For $\mathrm{E}_{\mathrm{y}} = 0$,

$$\varepsilon_{\mathrm{x}} = \hat{\mathrm{a}}_{\mathrm{x}}\mathrm{E}_{\mathrm{x}} \cos(\omega \mathrm{t} + \varphi_{\mathrm{x}}) \tag{2.19}$$

$$\varepsilon_{\mathrm{y}} = 0 \tag{2.20}$$

The final case occurs when both components of the electric field are in phase, satisfying,

$$\varphi_{\mathrm{x}} = \varphi_{\mathrm{y}} = \varphi \tag{2.21}$$

Then,

$$\varepsilon_{\mathrm{x}} = \hat{\mathrm{a}}_{\mathrm{x}}\mathrm{E}_{\mathrm{x}} \cos(\omega \mathrm{t} + \varphi) \tag{2.22}$$

$$\varepsilon_{\mathrm{y}} = \hat{\mathrm{a}}_{\mathrm{y}}\mathrm{E}_{\mathrm{y}} \cos(\omega \mathrm{t} + \varphi) \tag{2.23}$$

Where the oscillation angle is obtained as,

$$\theta = \arctan\left(\frac{\mathrm{E}_{\mathrm{y}}}{\mathrm{E}_{\mathrm{x}}}\right) \tag{2.24}$$

The scenario depicted in Figure 2.10a.

For circular polarization, it must be satisfied that both components have the same magnitude, such that:

$$\mathrm{E}_{\mathrm{x}} = \mathrm{E}_{\mathrm{y}} = \mathrm{E}_{\mathrm{o}} \tag{2.25}$$

Additionally, a phase difference of 90 degrees must be satisfied, thus,

$$\varepsilon_{\mathrm{x}} = \hat{\mathrm{a}}_{\mathrm{x}}\mathrm{E}_{\mathrm{o}} \cos(\omega \mathrm{t}) \tag{2.26}$$

$$\varepsilon_{\mathrm{y}} = \hat{\mathrm{a}}_{\mathrm{y}}\mathrm{E}_{\mathrm{o}} \cos\left(\omega \mathrm{t} + \frac{\mathrm{n}\pi}{2}\right) \tag{2.27}$$

The scenario depicted in Figure 2.10b. **It is worth noting that circular polarization is a particular case of elliptical polarization.**

Finally, in the case of elliptical polarization, a 90-degree phase difference is satisfied, but in this case, the magnitudes are different from each other. As is shown in Figure 2.10c.

2.4.3 Antennas

An antenna is a passive, inherently bidirectional device designed to transmit or receive electromagnetic radiation from (or to) free space. In particular, radio telescopes are receiving antennas specifically designed to capture radio waves (Figure 1.1) emitted by various phenomena originating in space.

There are various figures of merit used to characterize antennas, including directivity (D), gain (G), radiation pattern $\mathrm{F}(\theta, \phi)$, efficiency (η), half power beam width (HPBW), polarization, and more, which will be further elaborated upon in subsequent sections.

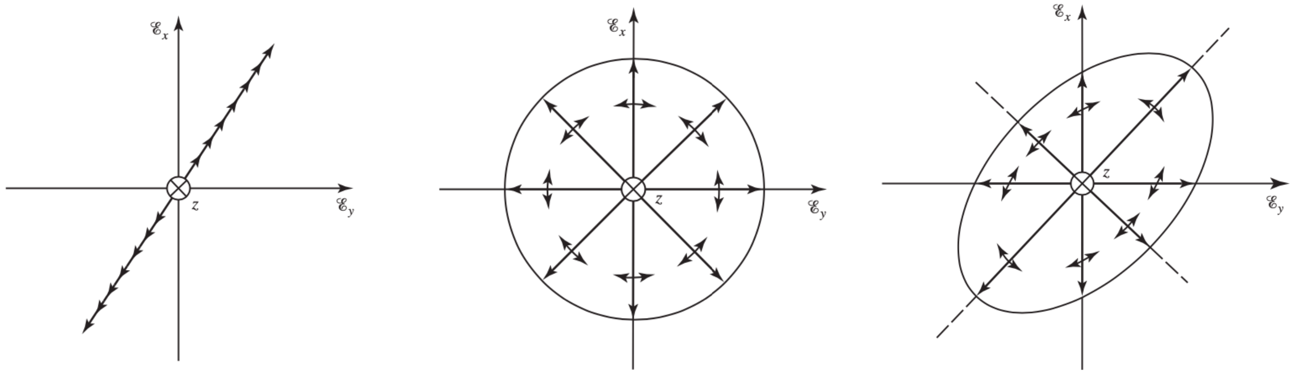

(a) Linear polarization (b) Circular polarization (c) Elliptical polarization

Figure 2.10: Polarization of the electric field as a function of time at a fixed position [4]

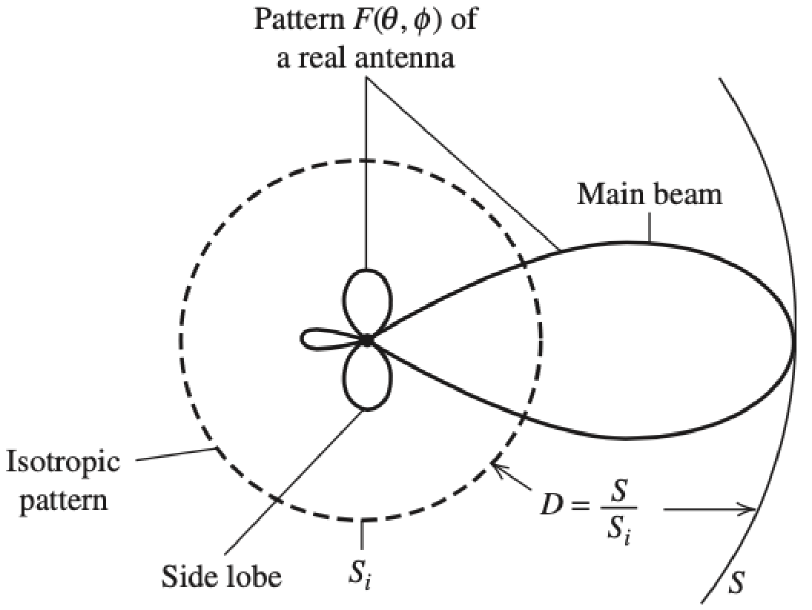

Figure 2.11: The image shows in a segmented line the radiation pattern for an isotropic antenna and in a continuous line for any antenna with high directivity (D), back lobe, and sidelobes. The radiation pattern is denoted with $\mathrm{F}(\theta, \phi)$. And the power densities with the letter S and $\mathrm{S_i}$ for the isotropic antenna [25].

Co-polarization

According to the IEEE Standard Definitions of Terms for Antennas, it is defined as the polarization that the antenna is intended to radiate (or receive) [26]. In simpler terms, for a single-port antenna, is sensitive only to one specific polarization, referred to as co-polarization or *copol*.

Cross-polarization

According to the IEEE Standard Definitions of Terms for Antennas, it is defined as the polarization orthogonal to a specified reference polarization, within a specified plane containing the reference polarization ellipse [26]. In other words, a single-port antenna that is sensitive to a single polarization is insensitive to the polarization orthogonal to the *copol* and is referred to as cross-polarization or *crosspol*.

2.4.4 Interferometry

Interferometry is a measurement technique that relies on the constructive or destructive interference of waves. It is commonly used for radio waves, light, and sound waves, among others.

2.4.5 Digital beamforming

Digital beamforming is a technique that involves sampling the RF signal and then digitally weighing it in both amplitude and phase. When these complex signals are summed together, they form the beam.

2.4.6 Arrays

An array is a regular collection of multiple antennas (i.e., 2 or more) arranged in a specific geometrical configuration such that, when connected, they function as a single antenna. **It is worth mentioning that a set of antennas is considered as an array only if their radiation patterns overlap in the far field.**

The arrangement of these antennas depends on the intended purpose, as it imparts different characteristics. For instance, it is possible to increase directivity, meaning an enhancement in gain at a specific point, allowing for more precise pointing and the detection of weaker signals.

In other words, different radiation patterns can be obtained, depending on the application, either achieving highly directional beams or omnidirectional coverage. By controlling the excitation phase and amplitude, it is possible to modify the orientation of the beam together with the size of the side lobes.

Furthermore, by combining the signals received by each element within the array, it becomes possible to reduce noise, contributing to an improvement in Signal-to-Noise Ratio (SNR), thus enhancing the quality and reliability of the signal of interest.

An illustrative example is presented using a simple case consisting of two antennas located at a distance **d** from each other. These antennas are then combined as depicted in Figure 2.12.

In Figure 2.12, four cases (a), (b), (c), and (d) are presented, respectively. For each of these

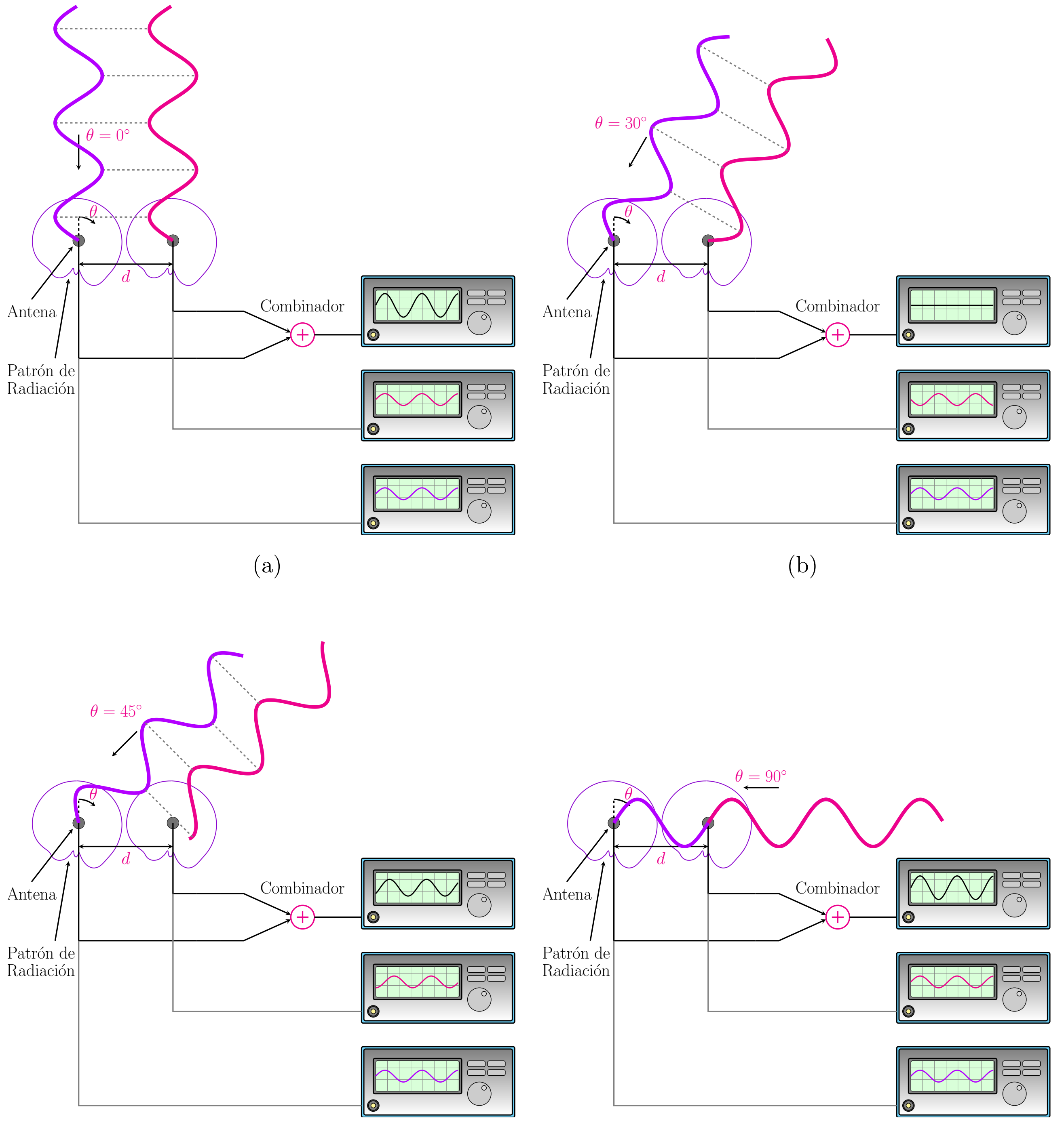

(a) (b)

(c) (d)

Figure 2.12: Illustrative example of antenna arrays for different angles of incidence for each wavefront [5].

cases, two antennas are symbolized by gray dots, separated by a distance **d**. Their radiation patterns are shown in purple as a function of the angle θ. It's worth noting that these antennas are considered identical. These antennas receive wavefronts that, depending on the case, arrive at different angles ($\theta = 0°$, $\theta = 30°$, $\theta = 45°$, and $\theta = 90°$), respectively. Subsequently, each incident signal is received by the antennas and combined using a combiner.

The type of interference produced depends on the angle of incidence of the wavefront, leading to the following cases:

- **Case a)** $\theta = 0°$: In this scenario, both waves arrive in phase at their respective antennas. Consequently, when these signals are combined, constructive interference occurs. This means that both signals add up in phase, positively contributing to their total power.

- **Case b)** $\theta = 30°$: In this case, as the signals have an incidence angle of $\theta = 30°$, the purple signal arrives first, followed by the magenta signal, with a specific delay of $\frac{\lambda}{2}$. Consequently, when combining the phased signals, complete destructive interference occurs. Therefore, for this angle of incidence, it can be concluded that no reception takes place.

- **Case c)** $\theta = 45°$: In this scenario, the waves arrive with a phase difference of $\frac{3\lambda}{4}$, resulting in destructive interference, although not complete. Therefore, there is reception, but it is not as strong as in **Case a)**.

- **Case d)** $\theta = 90°$: For this case, the same as in **Case a)**, total constructive interference is achieved. This is because the waves add up in phase, as the antennas are separated by a distance **d**, which coincides with λ.

Based on this explanation, two parameters that determine the total power reception in an antenna array emerge the Array Factor (AF) and the Element Factor (EF). The Array Factor is associated with the level of interference that occurs between waves arriving out of phase at the antennas, while the Element Factor is linked to the radiation pattern of the individual element comprising an array.

Therefore, in Figure 2.13, an illustrative example is presented, demonstrating the radiation pattern obtained when synthesizing an array, taking into account the contributions of both the Element Factor and the Array Factor. In the radiation pattern corresponding to the Array Factor (AF), the presence of four lobes with maximum gain ($\theta = 0°, 90°, 180°, 270°$) can be observed. The ones located at $\theta = 0°$ and $\theta = 180°$ are referred to as the main lobes, while the others are called grating lobes. It's important to note that this example is derived from 2.13. In this context, as the AF is purely associated with wave interference, the main lobes occur at angles θ where constructive interference takes place. This condition is also satisfied when the waves reaching the antennas have a phase offset that is a multiple of the wavelength.

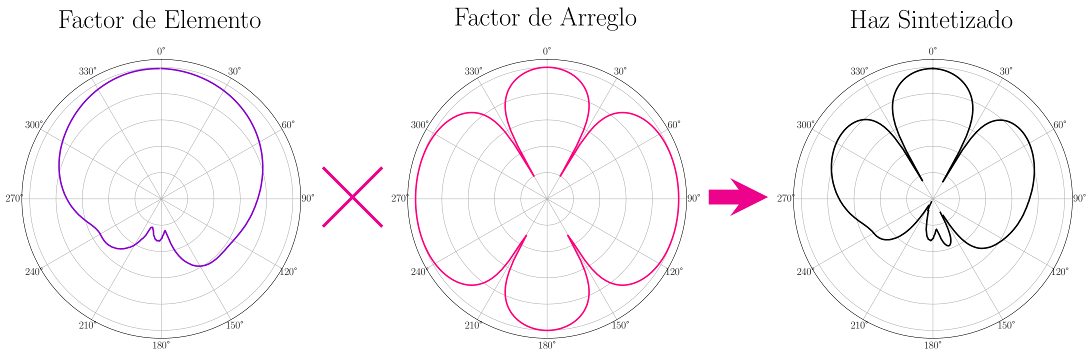

Figure 2.13: Radiation Patterns from left to right: Element Factor, Array Factor, Synthesized Beam [5].

Finally, in Figure 2.14, a specific scenario is presented in which, even though the wavefronts exhibit the same phase offset of $\frac{\pi}{2}$ for both case (a) and case (b), they differ in the angle of incidence θ. For the first case, the angle is $\theta = 45°$, while for the second case, it is $\theta = -17°$, this is referred to as **phase ambiguity**.

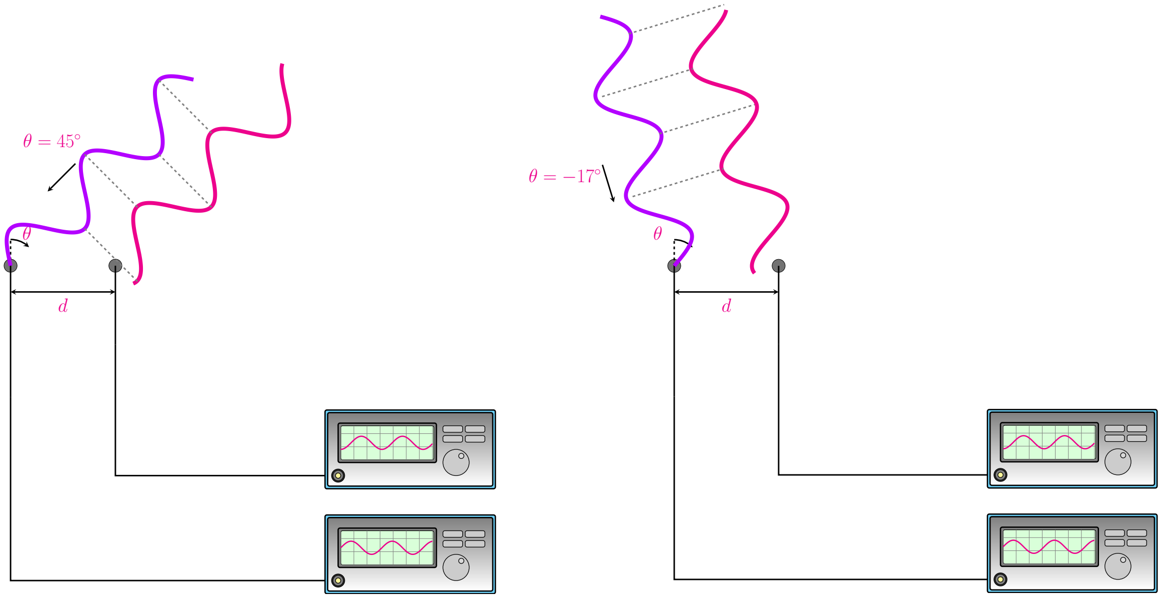

(a)

(b)

Figure 2.14: Illustrative example of **phase ambiguity** In both cases (a) and (b), the antenna on the left side receives a sine wave, while the antenna on the right side receives a negative cosine wave. In both cases, there is a 90° phase difference between antennas, but the angles of incidence are different ($\theta = 45°$ in (a) and $\theta = -17°$ in (b) [5].

This phase ambiguity plays a significant role when attempting to identify the source of a certain signal. In particular, as detailed in Chapter 3, to determine the location of FRB sources, it is necessary to have an array with specific qualities that, in turn, address the issue of phase ambiguity.

2.4.7 Direct microwave receiver

A microwave receiver is an electronic device designed to receive and process electromagnetic signals within the microwave radio frequency range, typically ranging from approximately 300MHz to 300GHz.

This device is employed to receive and condition signals emitted by an external antenna or source. It undergoes various stages, including amplification and filtering.

Amplification stages are necessary since microwave signals are often weak upon reception. Additionally, depending on the application, specific frequency ranges may need to be observed. In such cases, filters are used to select the desired operating range while reducing interference.

Finally, the processed analog signal is transmitted to the Back-End system, where it is digitized and subjected to various processing techniques.

2.4.8 Noise

Noise is a parameter that allows quantifying the noise power of electronic components. This noise can originate from various random processes, such as thermal noise from thermal vibrations. This parameter is directly related to the sensitivity of the device because it establishes a minimum threshold above which the desired signals must be for detection.

Noise Temperature and Y-Factor

From the circuit in 2.15, it is possible to establish a relationship between the equivalent noise temperature $\mathrm{T_e}$ and the noise power $\mathrm{N_o}$.

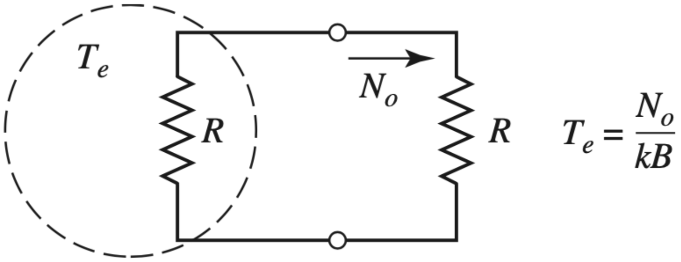

Figure 2.15: The image shows a noisy resistor of value R with an equivalent noise temperature $\mathrm{T_e}$ [27].

If we consider a noisy resistor that delivers a noise power of $\mathrm{N_o}$, it is possible to obtain the equivalent noise temperature $\mathrm{T_e}$ such that the same noise power is delivered to the load R. With this, we have:

$$\mathrm{T_e} = \frac{\mathrm{N_o}}{\mathrm{kB}} \tag{2.28}$$

It is possible to extrapolate this expression for cases where components with gains are present, such as amplifiers, assuming that it is a noiseless amplifier. In this manner, equation 2.28 becomes:

$$\mathrm{T_e} = \frac{\mathrm{N_o}}{\mathrm{GkB}} \tag{2.29}$$

The circuit shown in 2.16 allows for the characterization of the equivalent noise temperature of a system. To do this, two ideal loads with known and significantly different temperatures are presented. In this case, we have $\mathrm{T_1}$ as the temperature of the hot load and $\mathrm{T_2}$ as the temperature of the cold load. Additionally, it is known that the powers of each load are given by $\mathrm{P_1}$ and $\mathrm{P_2}$, respectively. Therefore, we can formulate the following system of equations:

$$\mathrm{N_1} = \mathrm{GkT_1B} + \mathrm{GkT_eB} \tag{2.30}$$

$$\mathrm{N_2} = \mathrm{GkT_2B} + \mathrm{GkT_eB} \tag{2.31}$$

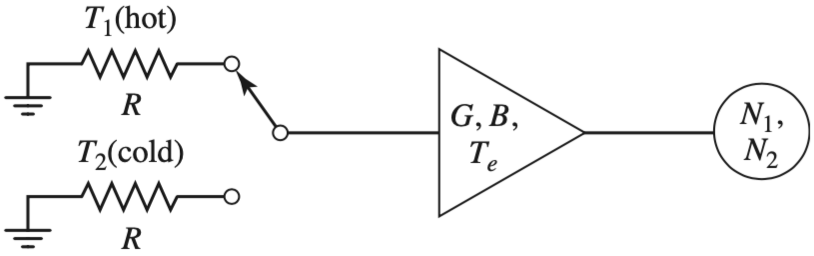

Figure 2.16: The method is called the Y-factor for measuring the equivalent noise temperature of an amplifier[27].

Where N_1 and N_2 are the noise powers measured at the output of the system, taking into account the contribution of both the load and the amplifier noise, then:

$$Y = \frac{N_1}{N_2} = \frac{T_1 + T_e}{T_2 + T_e} \tag{2.32}$$

$$T_e = \frac{T_1 - YT_2}{Y - 1} \tag{2.33}$$

Noise Figure

It is possible to characterize a noisy microwave component in two ways, as presented in 2.33. Another method of characterization involves using the noise figure (NF) of a component, which represents a measure of the reduction in the signal-to-noise ratio (SNR) between the component's input and output. The SNR can be understood as the ratio between the power of the desired signal and the power of the undesired noise.

In Figure 2.17, the equivalent circuit for a noisy network is depicted. When a network is noisy, the power of the output noise increases, and the SNR at the output of the network decreases. Therefore, the Noise Figure (NF) represents the quantification of the reduction in SNR that occurs when passing through a noisy network.

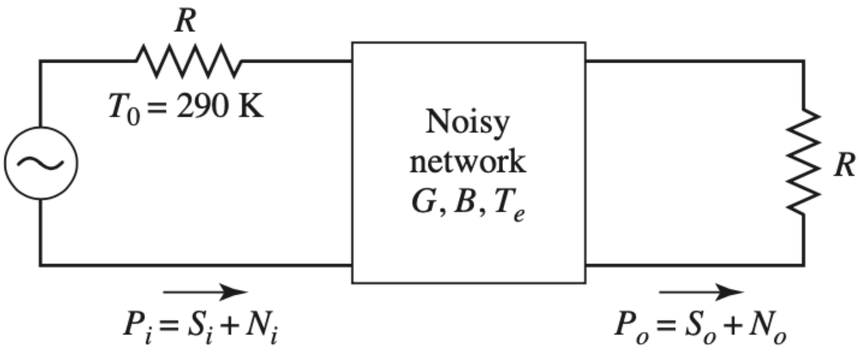

Figure 2.17: Noisy network [27].

Therefore, the Noise Figure (NF) is expressed by the following equation:

$$\mathrm{F} = \frac{\mathrm{S_i/N_i}}{\mathrm{S_o/N_o}} \geq 1 \tag{2.34}$$

Furthermore, it should be noted that

- $\mathrm{S_i}$ Input signal power, $\mathrm{N_i}$ Input noise power.
- $\mathrm{S_o}$ Output signal power, $\mathrm{N_o}$ Output noise power.

In Figure 2.17, an ambient-temperature resistor is depicted with $\mathrm{T_o} = 290$ K. Consequently, the input noise power can be expressed as:

$$\mathrm{N_i} = \mathrm{kT_oB} \tag{2.35}$$

Furthermore, since the noisy network is characterized by the parameters G, B, and $\mathrm{T_e}$ (Gain, Bandwidth, Equivalent Temperature), the output noise power is determined by the input noise power in addition to the contribution of the network's noise power. Consequently, it can be expressed as follows:

$$\mathrm{N_o} = \mathrm{kT_oB} + \mathrm{kGT_eB} \tag{2.36}$$

In this way, by generalizing the result of the Noise Figure and assuming that $\mathrm{S_o} = \mathrm{GS_i}$, it can be established that:

$$\mathrm{F} = \frac{\mathrm{S_i}}{\mathrm{kT_oB}} \frac{\mathrm{kGB(T_o + T_e))}}{\mathrm{GS_i}} = 1 + \frac{\mathrm{T_e}}{\mathrm{T_o}} \geq 1 \tag{2.37}$$

Finally, the equivalent temperature is defined as:

$$\mathrm{T_e} = (\mathrm{F} - 1)\mathrm{T_o} \tag{2.38}$$

Noise Figure of a Cascaded System

It is possible to generalize the result defined in 2.38 for a system connected in cascade, as illustrated in Figure 2.18. In microwave systems, the input signal typically passes through multiple components, which are interconnected in cascade and, in addition to their primary functions, act as noisy networks that degrade the signal-to-noise ratio (SNR), as previously mentioned.

If the noise figure or noise temperature of each stage within the cascaded system is known, it becomes possible to calculate the equivalent noise figure or equivalent noise temperature of the entire system. It is important to highlight that the first stage usually plays a dominant role as it significantly impacts the final result.

In this manner, it can be determined that the noise power at the output of the first stage is expressed as:

$$\mathrm{N_1} = \mathrm{G_1kT_oB} + \mathrm{G_1kT_{e1}B} \tag{2.39}$$

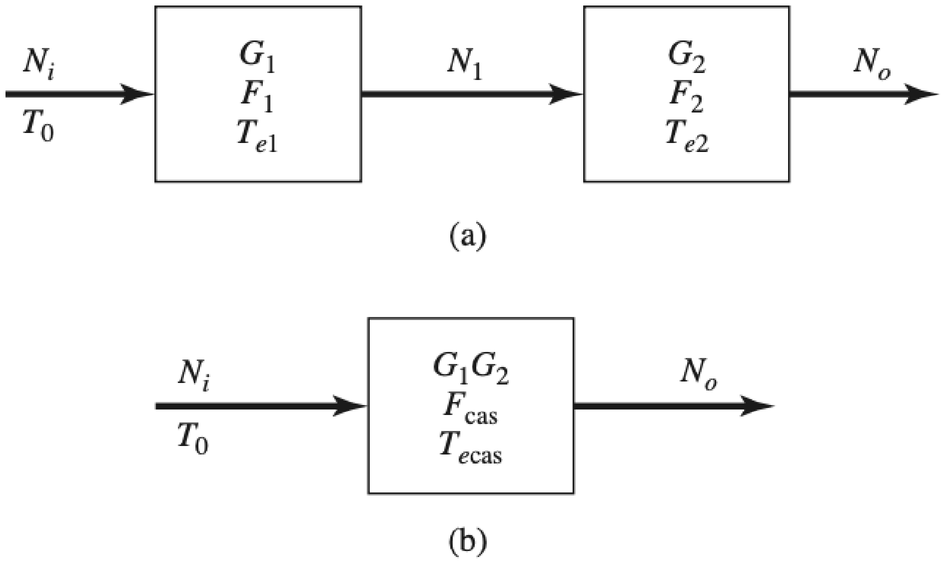

Figure 2.18: In (a), a cascaded system is depicted along with its respective characterization parameters. In (b), the equivalent network is shown with its corresponding equivalent parameters. [27].

Similarly, for the output of the second stage, one has:

$$\mathrm{N_o = G_2N_1 + G_2kT_{e2}B = G_1G_2kB}\left(\mathrm{T_o + T_{e1} + \frac{T_{e2}}{G_1}}\right) \tag{2.40}$$

Generalizing,

$$\mathrm{N_o = G_1G_2kB\left(T_{cas} + T_o\right)} \tag{2.41}$$

So, the Noise Temperature of the cascade system is given by,

$$\mathrm{T_{cas} = T_{e1} + \frac{T_{e2}}{G_1}} \tag{2.42}$$

In a generalized context, for a cascaded system of n-elements, the following expression holds for calculating the equivalent noise temperature

$$\mathrm{T_{cas} = T_{e1} + \frac{T_{e2}}{G_1} + \frac{T_{e3}}{G_1G_2} + ... + \frac{T_{en}}{G_1G_2...G_{n-1}}} \tag{2.43}$$

Harmonic and Intermodulation Distortion

Due to the nonlinearity of real-world components, in addition to incurring thermal noise due to their losses, they can exhibit nonlinear behaviors at low power levels.

Among these nonlinear behaviors, we find the occurrence of intermodulation distortion, which, in simple terms, refers to the appearance of undesired tones resulting from the interaction of specific frequencies, which can further combine with their harmonics. For a detailed mathematical

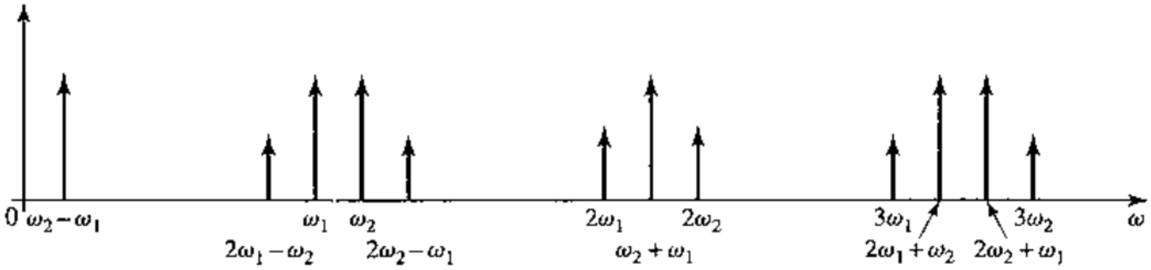

Figure 2.19: Spectrum of second and third-order products generated by the intermodulation of two tones at frequencies ω_1 and ω_2, respectively.[27].

explanation, it is recommended to consult **Chapter 10: Noise and Nonlinear Distortion** in [27]. Figure 2.19 shows, a particular case for the intermodulation caused by the interaction of two tones in different frequencies ω_1 and ω_2.

Crosstalk

This refers to the undesirable interference phenomenon that occurs between communication channels when any signal or circuit impacts the behavior of an adjacent channel. It can be conceptualized as an electrical coupling between desired and undesired signals.

Dynamic spectra or spectrogram

It is a plot to show the relationship between intensity per every frequency channel against time. In particular, in this thesis, the spectrograms display the intensity in Kelvin and the colormap is regarding the average of each frequency channel. Moreover, all spectrographs are plotted after subtracting the median value and then normalized by the standard deviation. For this reason, when presenting the plots the color bar represents the standard deviation over the data without the median, and it's measured in Kelvin.

Chapter 3

Assembly, characterization, and integration

3.1 Introduction

In this section, the primary ARTE subsystems are characterized, and the methodology used for the assembly process is presented. Firstly, to familiarize the readers with ARTE in a general context, a brief explanation is provided. This enables a more in-depth examination of each subsystem once their respective roles within the radio telescope are understood. Finally, a measurement of RFI is presented at two points of interest. Based on these results, the location for the operation of the ARTE radio telescope will be determined.

3.1.1 ARTE: astronomical radio transients experiment

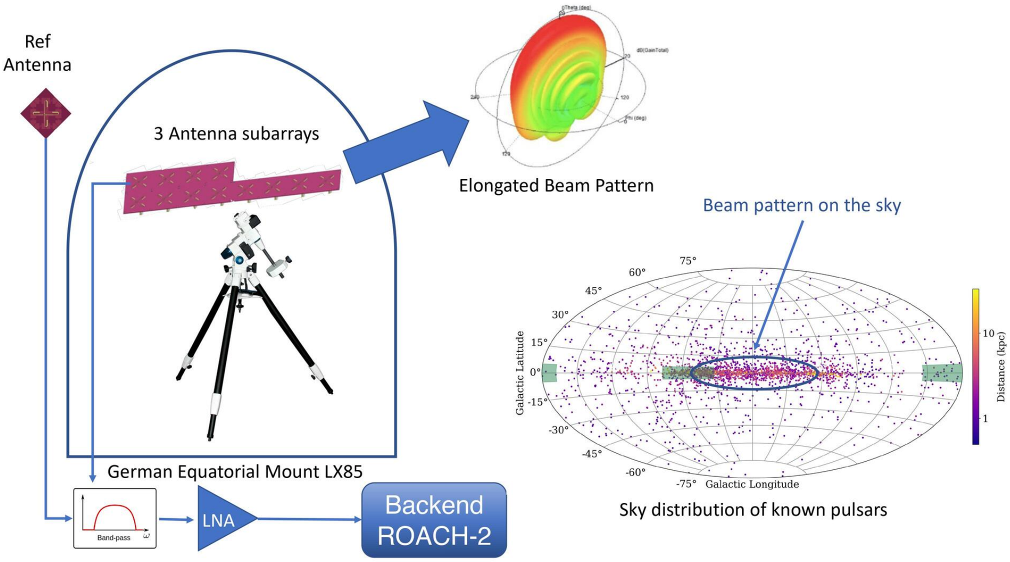

Figure 3.1: Left: A generic diagram of the ARTE radio telescope. Right: Galactic plane (l, b coordinates) showing the distribution of pulsars.

In Figure 3.1 on the left, the general diagram of the ARTE radio telescope is presented, where the following key elements can be identified:

- Antennas, consisting of a reference antenna and an array of antennas.
- Equatorial mount for Milky Way tracking.
- Front-end, comprising filtering and amplification stages.
- Back-end implemented in ROACH2

Furthermore, in Figure 3.1 on the right, the galactic plane is depicted using (l, b) coordinates, representing Galactic longitude and latitude, respectively. This figure illustrates the distribution of known pulsars, with a specific focus on their concentration within the central region of the Milky Way, delineated by a light blue ellipse. This concentration pattern plays a crucial role in determining the radiation pattern to be implemented for the main antenna of the radio telescope.

3.1.2 Antenna array

In this section, the key aspects of ARTE's antenna design will be discussed, focusing on essential qualities, and presenting radiation pattern characterization results. It's important to note that this section is based on the information documented in [5][28].

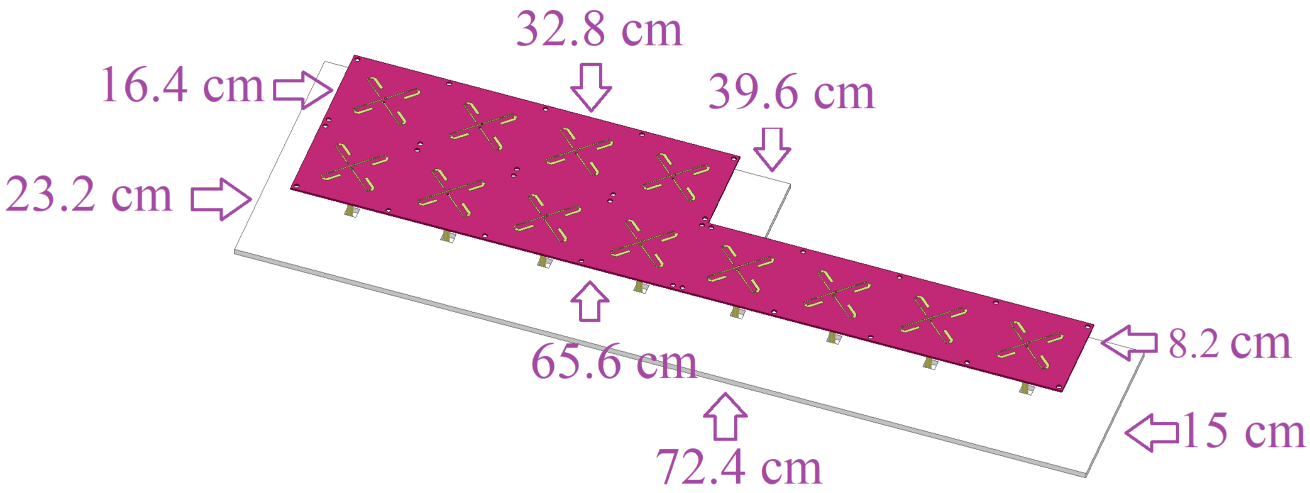

Figure 3.2: ARTE antenna consisting of three subarrays simulated in HFSS. Dimensions of the complete antenna (which are the same as those of the constructed antenna).

The design of the ARTE radio telescope's antenna was aimed at meeting the following requirements:

- Operation within the frequency range of 1.2 to 1.8 GHz, corresponding to a fractional bandwidth of 40 %.
- An elongated radiation pattern that, when projected onto the galactic plane, conforms to the particular elliptical shape of the Milky Way.
- Usability for source localization through the use of the direction of arrival (DoA) algorithm.
- Dual polarization.

- $S_{11} < -10\text{dB}$

- Front-back ratio (FBR) > 10 dB.

As mentioned earlier, there are several criteria that the antenna must meet. In this thesis, the focus will primarily be on the design elaborated to achieve the elongated radiation pattern and facilitate source localization.

Array Radiation Pattern, DoA, and Polarization

Firstly, the antenna must exhibit an elongated radiation pattern to align as closely as possible with the center of the Milky Way, as depicted in Figure 3.3 (where known pulsars are concentrated). To achieve this, considering the dimensions of the semi-axes of the ellipse, a Half Power Beam Width (HPBW) of 80° along the x-axis and approximately ~ 15 ° along the y-axis was established.

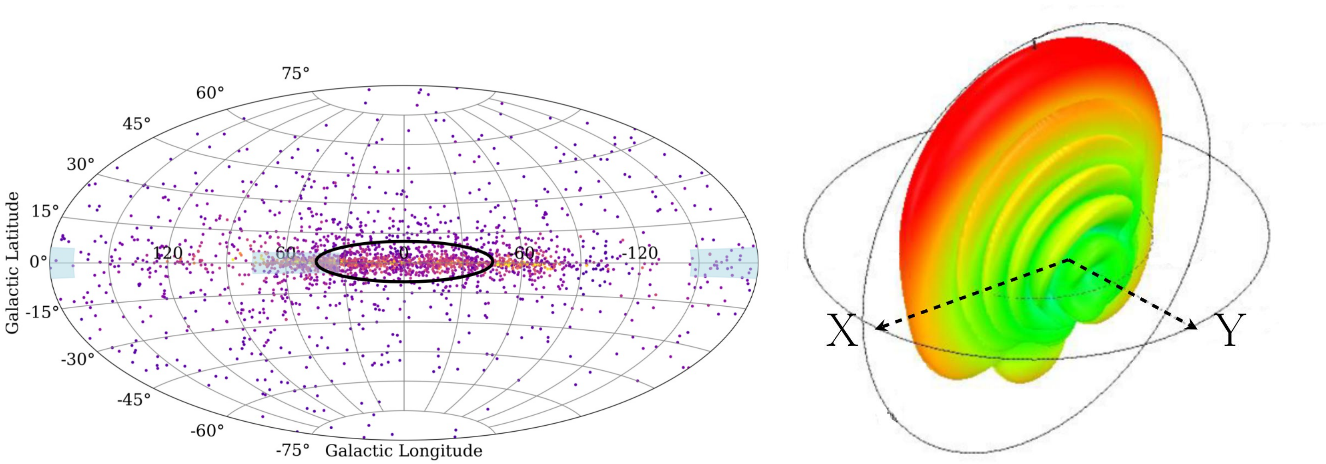

(a) Projection in the Galactic plane.

(b) 3D radiation pattern.

Figure 3.3: Expected radiation pattern of each sub-antenna.

To meet the HPBW requirements, a configuration of 8 × 1 elements is proposed, with each antenna having HPBWs of 80° × 80°. According to antenna array theory, doubling the number of elements results in a doubling of gain (i.e., 3dB increase), while the HPBW is halved. Consequently, with the suggested array dimensions, HPBWs of 80° × 10° are achieved, satisfying the initial requirements. Following this logic, the decision is made to form each sub-array with four individual antennas. By combining two in the y-axis, the desired radiation pattern is achieved, as is shown in Figure 3.4.

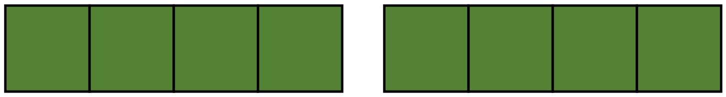

Figure 3.4: Two sub-array 4 x 1

Direction of Arrival requirement

In terms of positioning, it has been determined that the antenna should be configured in an **L** shape to enable the localization of the source, as illustrated in the example in Figure 3.5. This choice is based on the concept of phase ambiguity, as elaborated in Chapter 2, under the Arrays subsection. In simple terms, this concept involves having two signals with the same phase for different incident angles θ. Hence, the antenna array forming the primary ARTE antenna should be designed in the shape of an **L** to accommodate two sub-arrays, as shown in Figure 3.4, for synthesizing the elongated beam. Additionally, a third sub-array is required for signal localization in the sky.

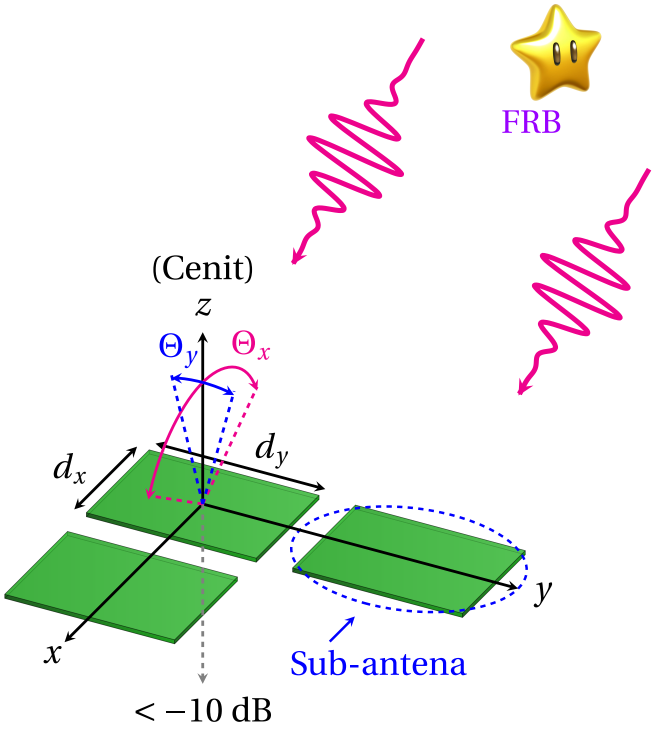

Figure 3.5: General design proposal to meet radiation pattern and DoA requirements

Dual polarization requirement

While the majority of reported FRBs are linearly polarized, the exact polarization of these signals remains uncertain. Thus, to guarantee sensitivity to signals of any polarization, a dual-polarization antenna is required.

Regarding the chosen antenna that fulfilled the $dual-polarization$ requirement, two dipoles were selected and positioned in an orthogonal arrangement to each other but in a diagonal orientation concerning the sub-arrays axis. This decision was made because if they were placed orthogonally but parallel to the sub-array, the radiation patterns would exhibit variations in the respective cuts within the X and Y planes, potentially affecting the radiation pattern for each polarization. This is illustrated in Figures 3.6 and 3.7.

To reduce costs and optimize space, it was determined that both orthogonal and diagonal dipoles should be constructed within a single element, as shown in Figure 3.7.

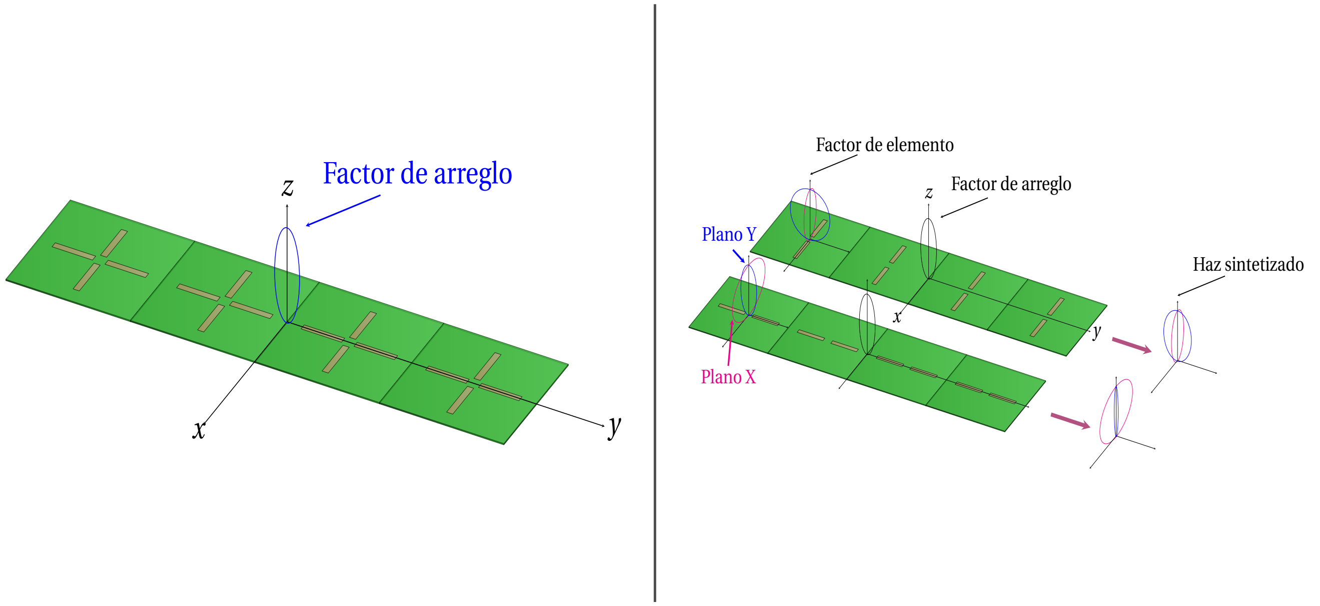

Figure 3.6: Left: a sub-array is displayed, comprising four antennas, with each single element consisting of two orthogonal dipoles. On the right, a breakdown of the radiation patterns is presented (assuming $z > 0$), illustrating patterns that vary depending on the dipole orientation, resulting in distinct radiation patterns for each polarization [5].

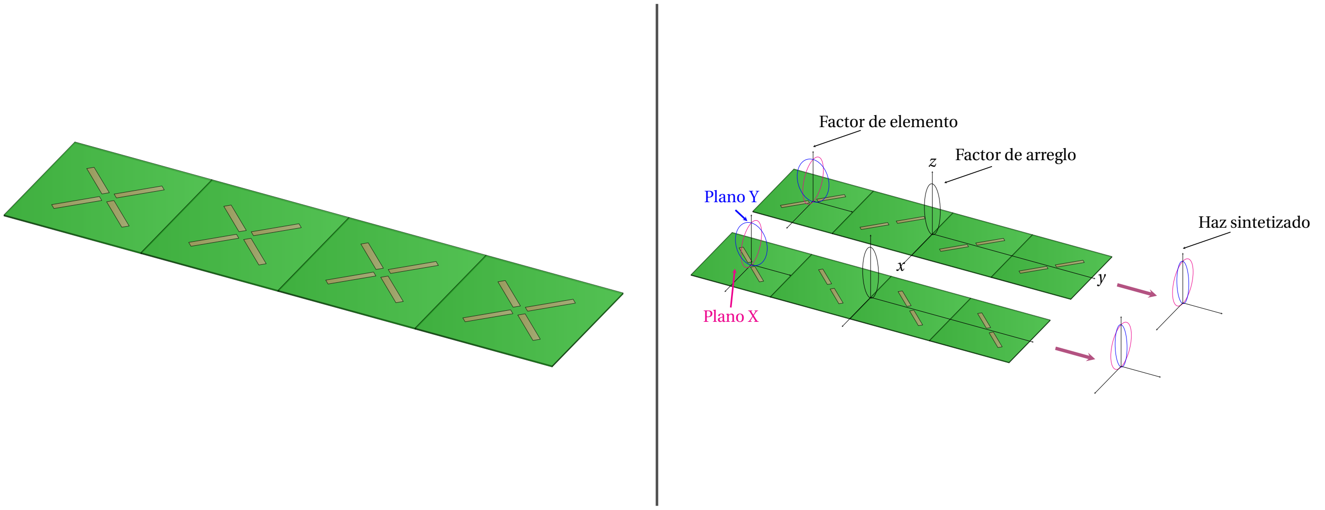

Figure 3.7: Left: a sub-array consisting of four antennas is displayed, with each single element comprising two diagonal dipoles. On the right, a breakdown of radiation patterns is shown (assuming $z > 0$), illustrating the patterns for different dipole orientations, resulting in identical radiation patterns for each polarization [5].

Finally, the proposed antenna is an array composed of three sub-arrays. Each element is comprised of four diagonal dipoles aligned with the array's axes, addressing the aforementioned challenges. The antenna was constructed on an R04003C substrate, with a thickness of 1.5 mm. Each antenna features dual feed lines for each polarization, utilizing IPEX connectors, as illustrated in 3.8.

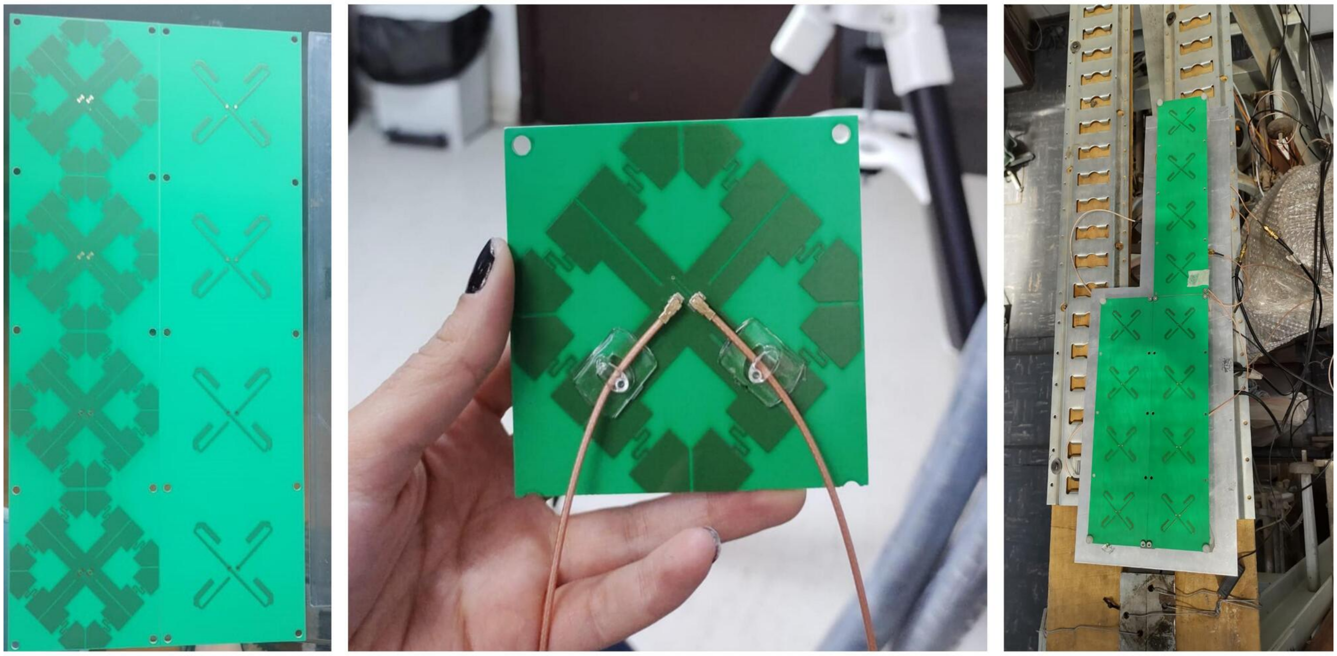

Figure 3.8: Left: Sub array. Centre: Single element. Right: Main array

It's worth mentioning that, at the moment ARTE is using just one antenna polarization for testing the whole system.
Lastly, for the characterization of the ARTE antenna, the anechoic chamber of the Millimeter-Wave Laboratory (MWL) was employed, following the setup depicted in Figure 3.9.

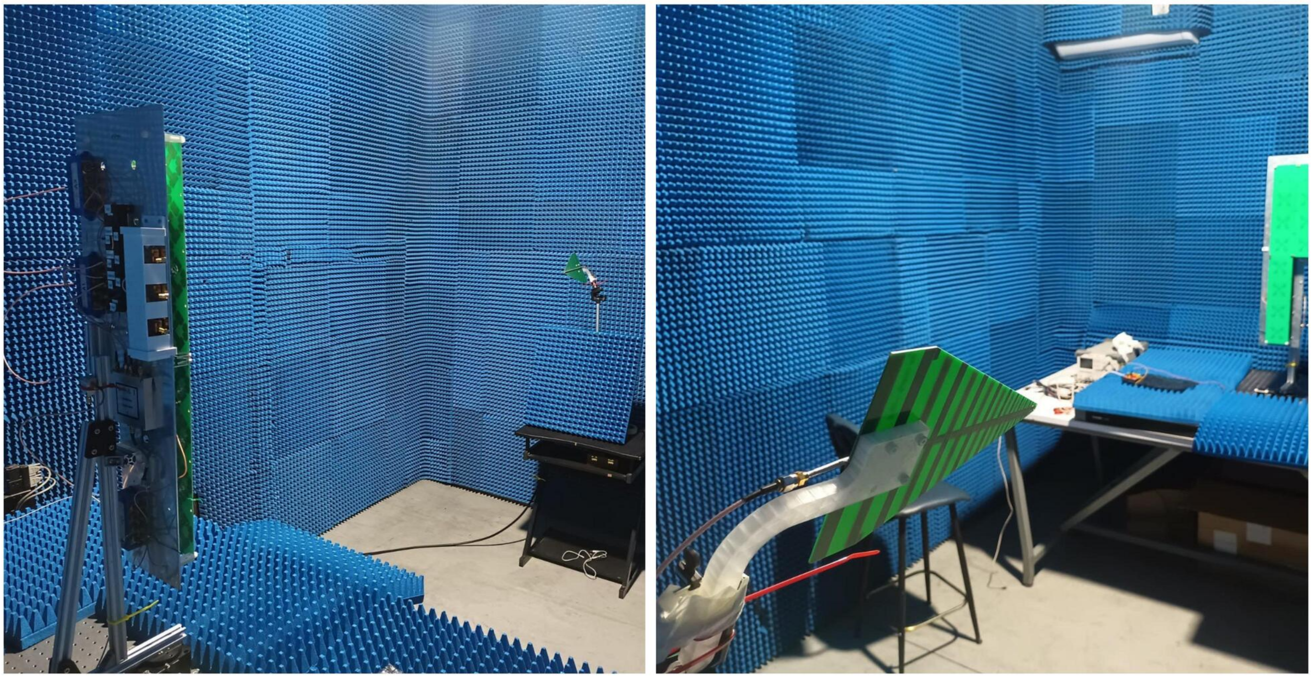

Figure 3.9: Measurement setup in the anechoic chamber.

Finally, the measurement results characterizing the radiation pattern are presented in Figure

3.10, along with the simulation outcomes from the HFSS software.

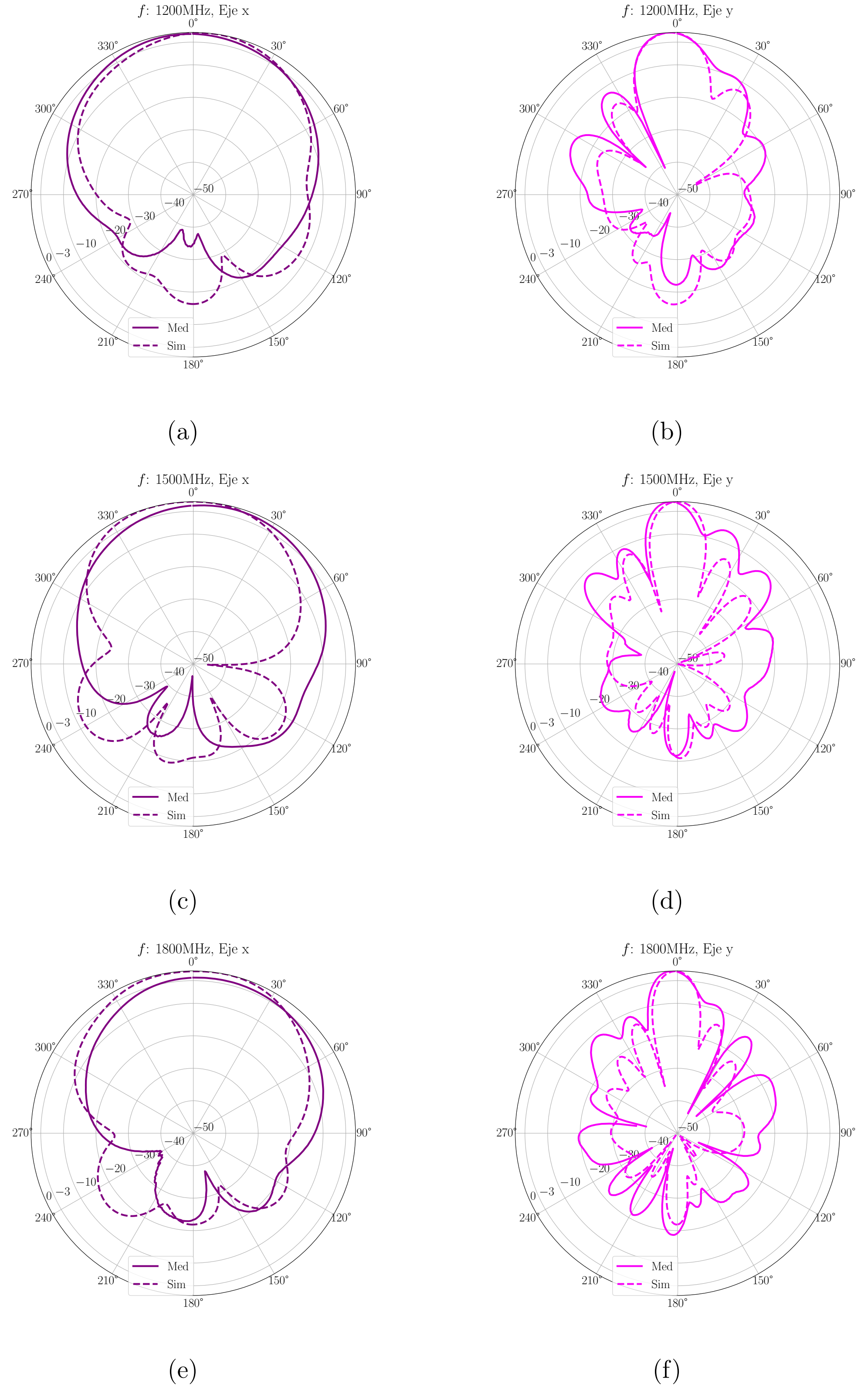

(a) (b) (c) (d) (e) (f)

Figure 3.10: Shows the normalized radiation patterns for 1.2, 1.5, and 1.8 GHz. The segmented line presents the simulation and the continuous line presents the measured radiation pattern [5].

The results presented in Table 3.1 are derived from Figure 3.10.

Parameter	**1.2 GHz**	**1.5 GHz**	**1.8 GHz**
HPBW x *axis*	77°	71°	58°
HPBW y *axis*	21°	14°	14°
Gain	11.28 dBi	12.57 dBi	12.71 dBi

Table 3.1: Key Parameters Obtained from the Characterization of the Radiation Pattern of the ARTE Antenna

Given the complexity of the ARTE antenna design, meeting the initial requirements seemed challenging to build. However, these requirements were successfully achieved, except for the desired HPBW.

3.1.3 Microwave receiver

The microwave receiver, initially designed as part of an undergraduate thesis [29], was intended for use in ARTE. Note that while this section draws upon that development, it underwent several modifications during the integration and assembly process to enhance its performance. These adjustments were made to address issues such as *harmonic* and *intermodulation distortion*, *crosstalk*, *saturation*, and more, which will be discussed in detail throughout this section.

The final design of the receiver chain is illustrated in Figure 3.11. Initially, this design included a 3 dB attenuator between the last low-noise amplifier ZX60-2534MA [30] and ROACH2. The purpose of this attenuator was to mitigate standing waves resulting from reflections and to prevent saturation of the ROACH2 ADCs. However, it was subsequently replaced with a 20 dB attenuator, positioned between the ZEQ-8-222S+ [31] equalizer and the final amplifier ZX60-2534MA [30]. This modification aimed to prevent saturation in the mentioned amplifier, as its IP_{3dB} is relatively low.

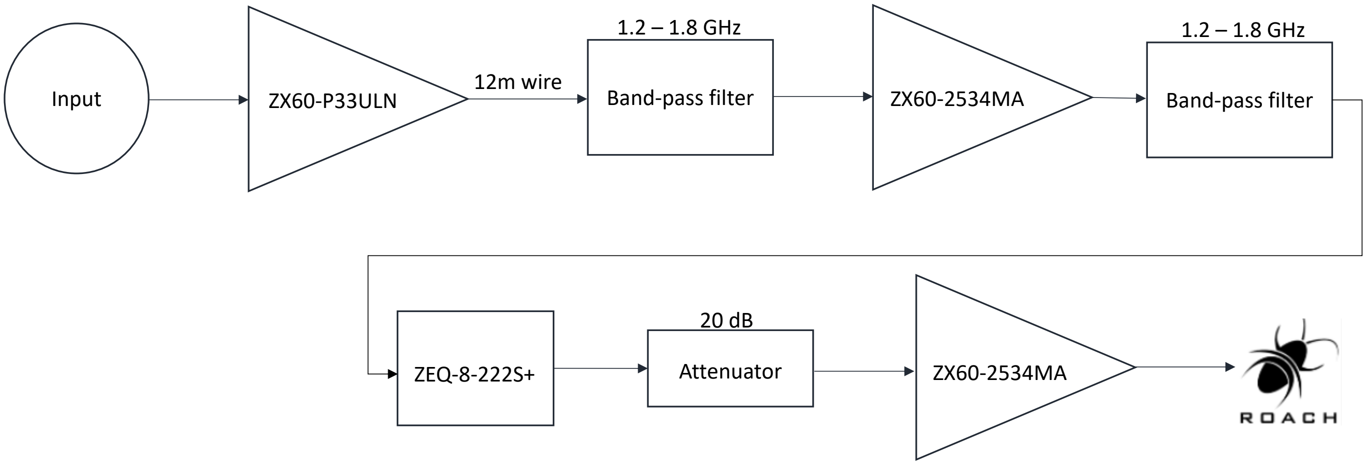

Figure 3.11: Block diagram of the entire amplification chain

Concerning the design proposed in [29], three significant modifications were implemented, which are subsequently mentioned and briefly justified as follows:

- Exchange of attenuation and increase from 3–20 dB. This modification was undertaken because intermodulation interference was measured, as explained in Chapter 2. This interference occurred because, in the final amplification stage, the ZX60-2534MA [30] amplifier occasionally operated in the saturation region.

- Separation of amplification chains into individual aluminum enclosures. Owing to the crosstalk issue discussed in Chapter 2, it was deemed necessary to isolate each of the amplification chains due to their undesirable interaction.

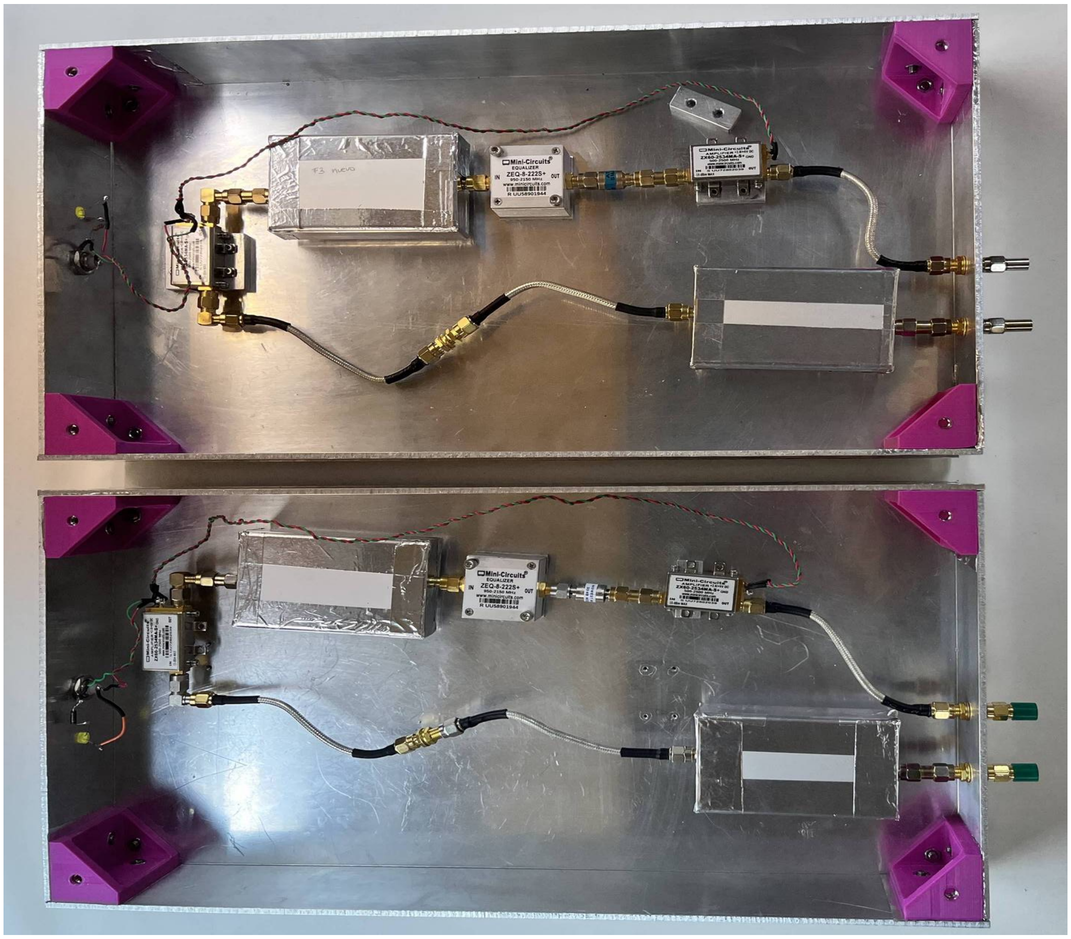

Figure 3.12: Two identical amplification chains in separate enclosures.

- Change of the first amplifier in the ZX60-P333ULN [32] chain. This modification was carried out due to the relocation of the receiver and antenna, resulting in a separation distance of over 8 meters, necessitating an extension of approximately 12 meters for the RF connection. As explained in Chapter 2, the noise temperature of a cascaded system is primarily influenced by the noise temperature of the first element 2.43. To reduce the noise temperature of the chain, the ultra-low-noise (ULN) amplifier was positioned as the first component.

3.1.4 Calibration method

Noise sources are devices designed to provide known noise power levels. They are typically characterized by the excess noise ratio (ENR), which represents the ratio between the noise power of a noise source and the noise power of a load at room temperature, measured in decibels (dB). The

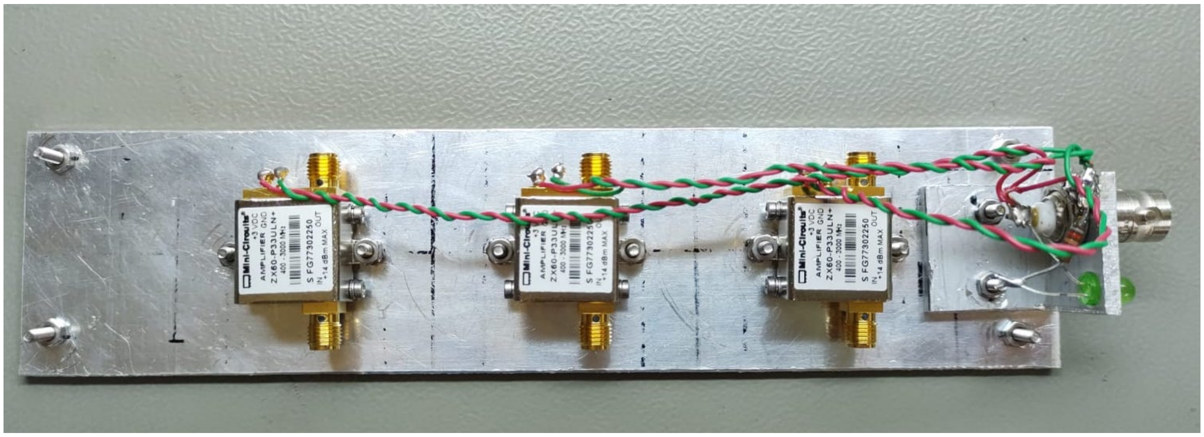

Figure 3.13: Assembly of ZX60-P333ULN [32] ULN amplifiers with their respective biasing connections. It is noteworthy that the board is positioned on the ground plane of the antenna, immediately following the analog combination of sub-arrays.

purpose of characterizing them with ENR is to achieve a calibrated output noise that accurately determines the noise figure (NF).

In particular, the Agilent 346B noise source [33] operates in the frequency range of 10 MHz to 18 GHz. It is designed to maintain a low standing wave ratio (SWR) to minimize measurement reflections.

$$\mathrm{ENR} = 10^{\frac{\mathrm{ENR_{dB}}}{10}} \tag{3.1}$$

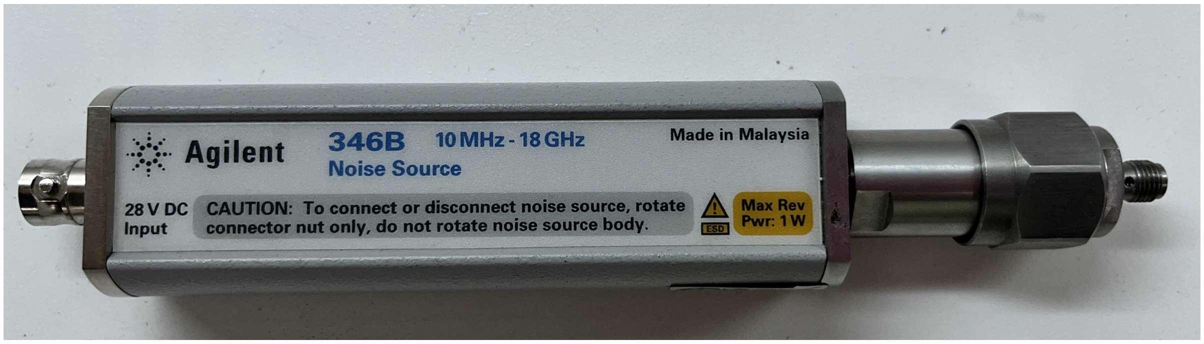

Figure 3.14: Agilent Noise Source 346B [33].

For calibration, the noise source depicted in Figure 3.14 is used in conjunction with the switch AS179-92LF [6] shown in Figure 3.16. The method involves connecting each of the three subarrays to one of the switch outputs, while the common noise source is connected to the other output. This common noise source is combined using a power splitter, as illustrated in Figure 3.17.

The objective is to alternate between the noise source and the sky using a switch. During a specified period, which in this case is 0.5 seconds, the noise source is observed to be active, providing a known noise temperature for the frequency of interest. Then, for the next 0.5 seconds, the noise source is turned off, equivalent to an ambient temperature load.

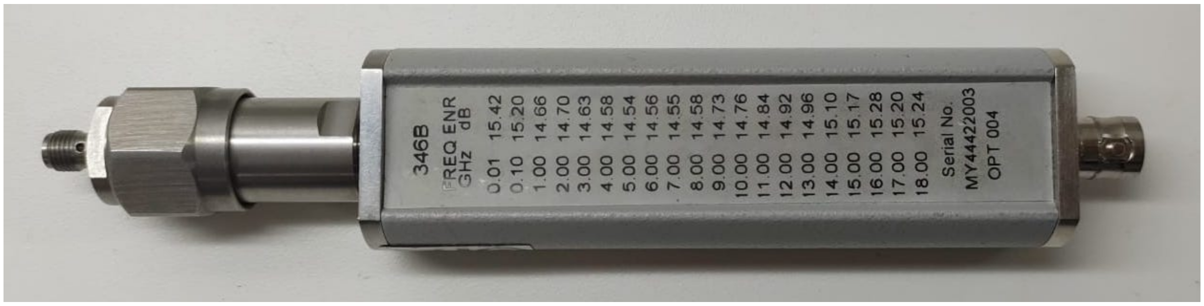

Figure 3.15: Agilent Noise Source 346B [33] back view

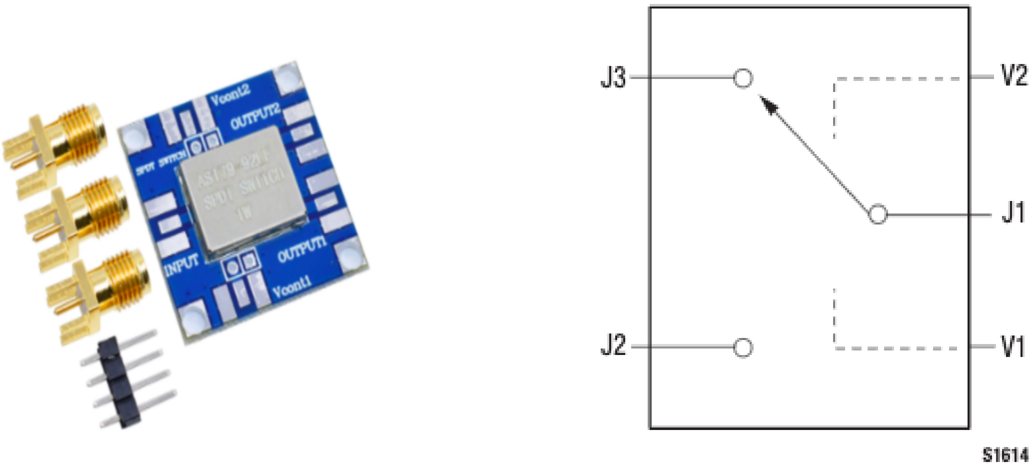

(a) Switch reference photo.

(b) Switch block diagram.

Figure 3.16: Switch AS179-92LF [6] used for the calibration setup.

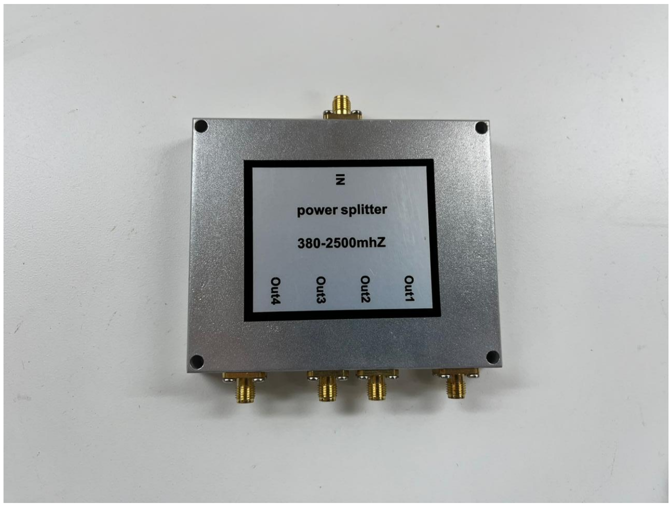

Figure 3.17: Power splitter illustrative photo

This approach allows for the calculation of an equivalent noise temperature based on the Y-factor. Subsequently, this equivalent noise temperature enables the determination of the receiver's noise temperature, and from there, the calculation of the system temperature. Below, you will find curves and equations that characterize this method.

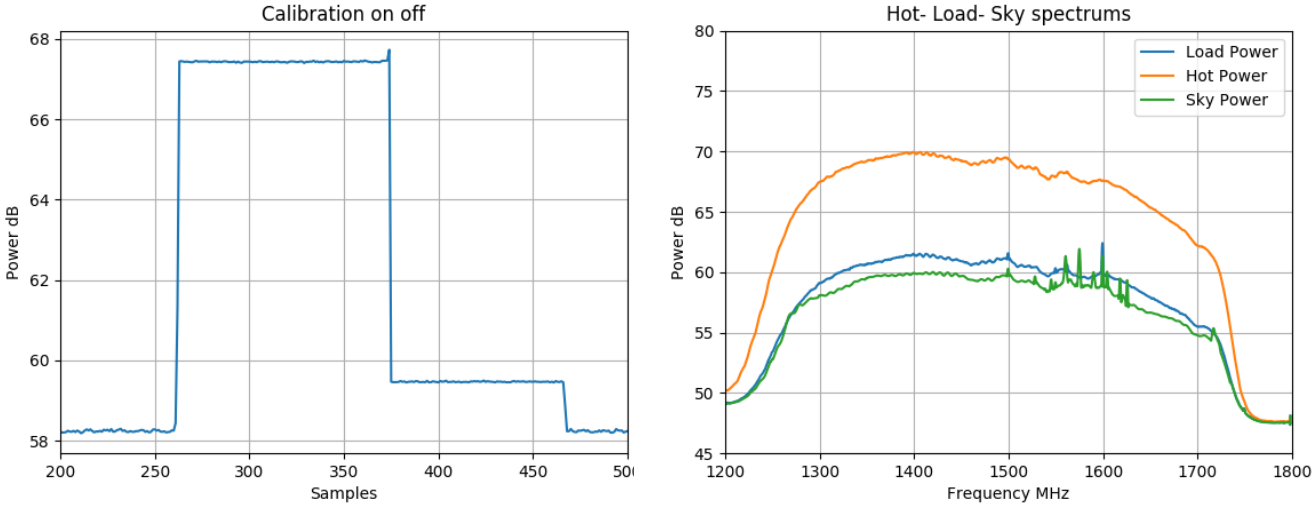

(a) Hot-Load-Sky calibration

(b) Hot-load-sky power spectrums

Figure 3.18: Hot-load-sky calibration

Figure 3.18a illustrates the power level differences in decibels for three power levels. The highest level corresponds to when the noise source is turned on, representing the power level denoted as $\mathrm{P_{hot}}$. The intermediate power level is obtained when the noise source is turned off, denoted as $\mathrm{P_{load}}$. The lowest value corresponds to the sky's power level, denoted as $\mathrm{P_{sky}}$.
Meanwhile, in Figure 3.18b, average power spectra are presented for the noise source when it's active (orange), turned off (blue), and for the sky (green), the latter showing the presence of RFI around 1600 MHz.

The ENR provided by the noise source 3.15 for the frequency of interest is obtained approximately as follows:

$$\mathrm{ENR_{ns}} = \frac{14.85 + 14.74}{2} = 14.795 \tag{3.2}$$

Therefore, it follows that:

$$\mathrm{t_{hot}} = 10^{\frac{14.795 - \mathrm{L}}{10}} \cdot \mathrm{t_{load}} + \mathrm{t_{load}} \tag{3.3}$$

In this manner, a known value is established for the temperature of the noise source, denoted as $\mathrm{t_{hot}}$, as determined by the expression 3.3. Furthermore, by employing the Y-factor method and solving for the receiver's noise temperature, we arrive at the following:

$$\mathrm{t_{rx}} = \frac{\mathrm{t_{hot}} \cdot \mathrm{P_{load}} - \mathrm{t_{load}} \cdot \mathrm{P_{hot}}}{\mathrm{P_{hot}} - \mathrm{P_{load}}} \tag{3.4}$$

Finally, from the following expression, the system temperature is derived as a function of the observed sky power denoted by $\mathrm{P_{sky}}$ and the previously obtained receiver temperature variation

t_{rx}.

$$t_a = \frac{P_{sky}}{P_{load}} \cdot (t_{rx} + t_{load}) - t_{rx} \tag{3.5}$$

It's worth noting that this value is a vector, as it varies for each spectral channel.

Noise temperature comparison, between a simulation of one complete chain in AWR and the measured noise temperature from each chain in the ARTE's whole setup.

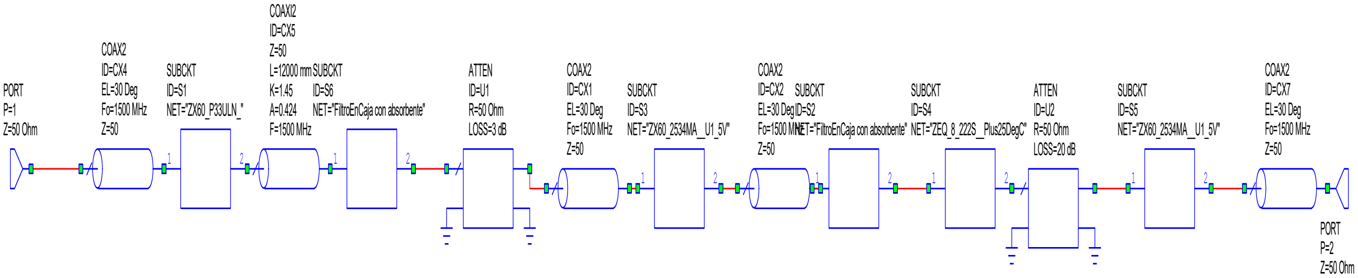

Figure 3.19: AWR's receiver chain model

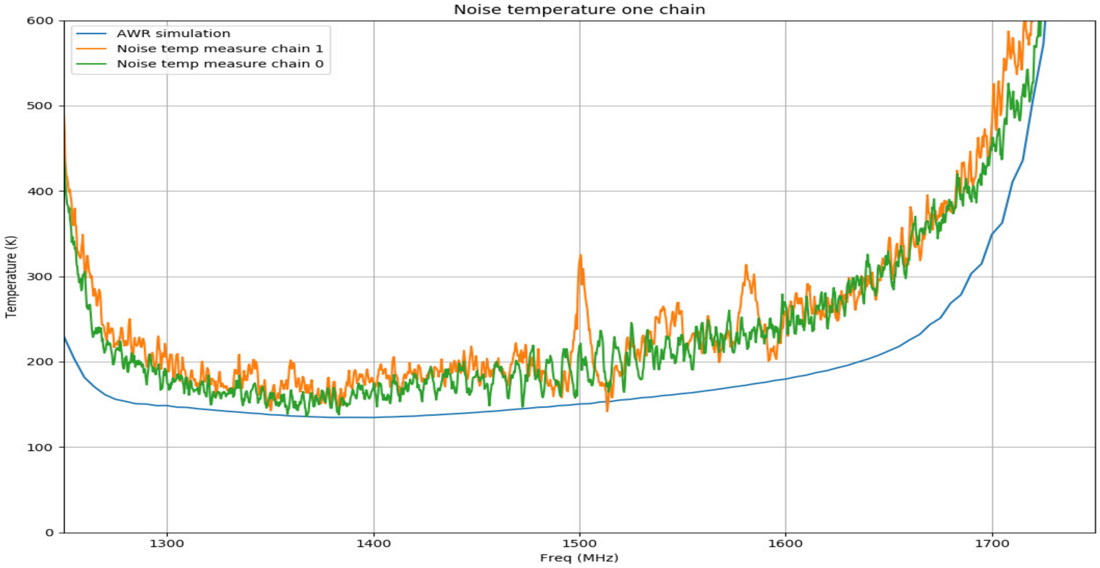

Figure 3.20: Noise temperature comparison

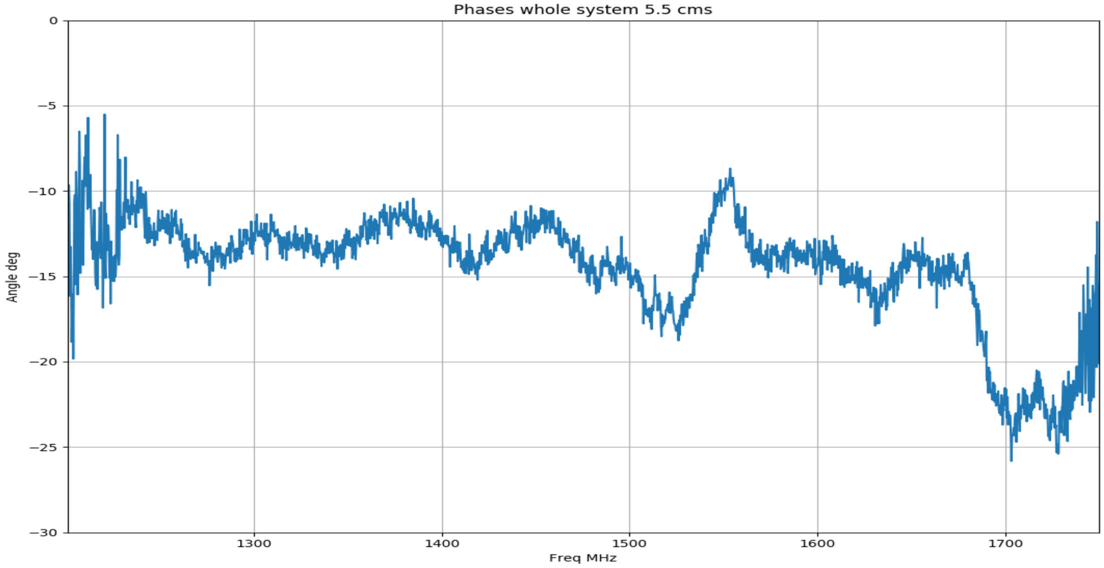

Figure 3.21: Phase between chain 0 and 1 used for the synthesized beam

Figure 3.21 shows a phase imbalance of less than ±5 degrees between the two amplification chains used for the synthesized beam. Moreover, an offset ∼ 12 degrees could be corrected digitally in FPGA, according to each frequency.

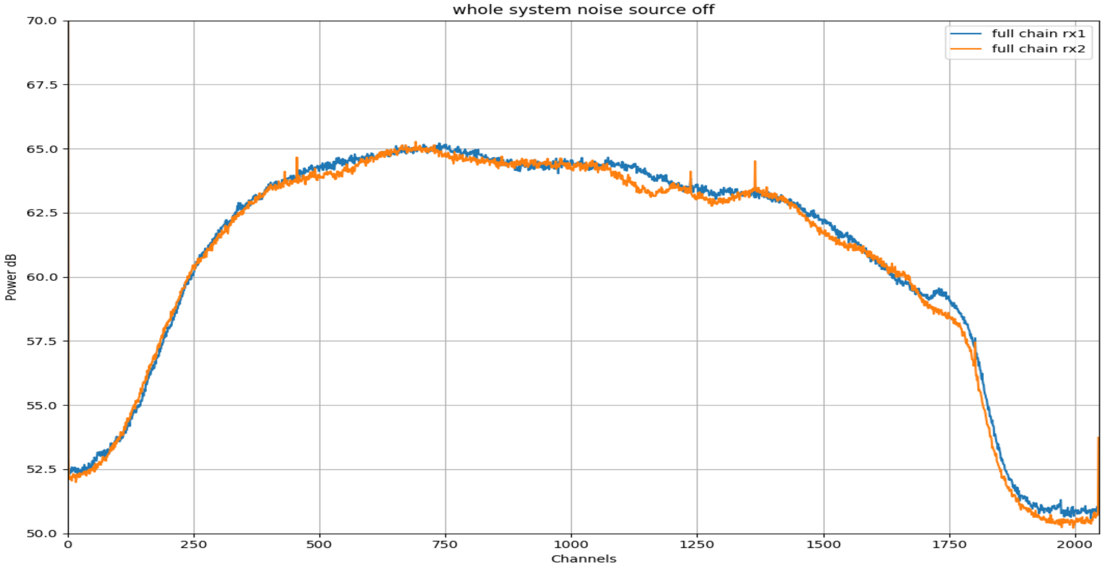

Figure 3.22: Gain comparison between chain 0 and 1 with load an ambient temperature

3.1.5 Spectral flux density calculations

This special flux density S_υ calculation is in particular for 1.5 GHz, due to this, each variable that depends on the frequency is obtained for 1.5 GHz.

$$\mathrm{t_a} = \frac{\mathrm{A_e} \cdot \mathrm{S}_\upsilon}{2\mathrm{k_B}} \tag{3.6}$$

Therefore,

$$\mathrm{S}_\upsilon = \frac{\mathrm{t_a} \cdot 2\mathrm{k_B}}{\mathrm{A_e}} \tag{3.7}$$

In the expression above 3.7, k_B corresponds to the Boltzmann constant, A_e the effective area, and T_a a temperature variation in the antenna, measured in Kelvin (K).
In this manner, for a 5 K temperature variation at the antenna, the spectral flux density is given by:

$$\mathrm{S}_\upsilon = \frac{5 \cdot 2 \cdot 1.38 \cdot 10^{-23}}{0.084} \tag{3.8}$$

$$\mathrm{S}_\upsilon = 1.6428 \cdot 10^{-21} \left[\mathrm{s^{-1}Kg}\right] \tag{3.9}$$

$$\mathrm{S}_\upsilon = 164.3\,[\mathrm{kJy}] \tag{3.10}$$

3.1.6 Sensitivity calculations

The sensitivity Γ for the ARTE antenna is calculated with the following expression, which relates the effective area A_e perpendicular to the incoming wavefront and is measured in K Jy^{-1}. And is given by,

$$\Gamma = \frac{\mathrm{A_e}}{2\mathrm{k_B}} \tag{3.11}$$

Therefore, replacing in the equation 3.11 it is obtained that,

$$\Gamma = \frac{0.084}{2 \cdot 1.38 \cdot 10^{-23}} \tag{3.12}$$

$$\Gamma = 3.04 \cdot 10^{-5} \left[\mathrm{KJy^{-1}}\right] \tag{3.13}$$

It is worth mentioning that as for the spectral flux density, the sensitivity calculations were performed for a frequency of 1.5 GHz.

3.1.7 Fluence calculations

$$\mathrm{F} = \Gamma^{-1} \frac{\mathrm{SNR} \cdot \mathrm{t_{sys}} \cdot \tau}{\sqrt{\Delta\upsilon \cdot \tau}} \tag{3.14}$$

Where, $\Delta\upsilon$ is the bandwidth of interest that in our case is 600 MHz, τ the time resolution of 10 ms, SNR the signal noise ratio, and t_{sys} the noise temperature of the system that is to $\sim$ 250 K, given by the equation 3.15.

$$\mathrm{t_{sys}} = \mathrm{t_{rx}} + \mathrm{t_a} \tag{3.15}$$

Finally, using the ARTE parameters:

$$\mathrm{F} = \frac{10^5}{3.04} \frac{5 \cdot 250 \cdot 10^{-2}}{\sqrt{6 \cdot 10^8 \cdot 10^{-2}}} \tag{3.16}$$

$$\mathrm{F} = 167.86[\mathrm{kJy} \cdot \mathrm{ms}] \tag{3.17}$$

3.1.8 Back-end

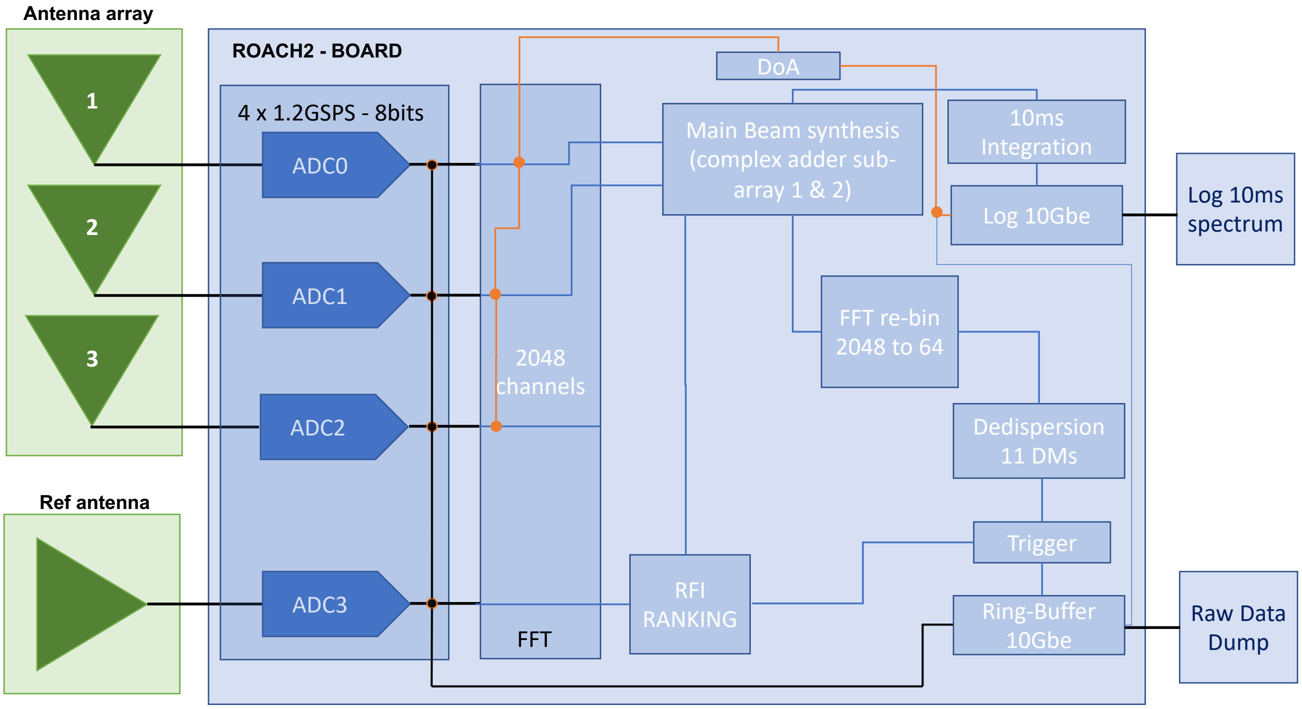

Figure 3.23: Backend's general block diagram

Figure 3.23 shows a block diagram depicted a general overview of the ARTE Back-end. The diagram is read from left to right, beginning with the antenna array, consisting of three subarrays, denoted as 1, 2, and 3, respectively. Each of the signals originating from the sky undergoes analog-to-digital conversion, followed by the application of the fast Fourier transform (FFT). Subsequently, real-time analysis is conducted on this data, enabling the detection of specific patterns or signals.

Following the FFT stage, the primary beam is synthesized using subarrays 1 and 2. This primary beam is integrated at 10-millisecond intervals and stored for offline processing. Additionally, the dimension of the primary beam is reduced, and it is subject to real-time analysis by eleven respective dedispersers. In the event of detection, these dedispersers trigger the temporal data to be saved in a ring buffer and subsequently baseband dump written to disk. Regarding subarray 3, it is employed in conjunction with subarrays 1 and 2 to apply the DoA detection algorithm. In the case of the reference antenna, it undergoes digitization and FFT processing. This enables statistical analysis to be performed, facilitating the distinction between data originating from celestial sources and RFI.

- **ADCs** The ADC block converts analog inputs to digital outputs. Every clock cycle, the inputs are sampled and digitized to 8-bit binary point numbers in the range of [-1, 1) and are then output by the ADC.

- **FFT** In this block, the fast Fourier transform calculation is performed. It is noteworthy that this calculation is carried out for each clock cycle, with a clock frequency of 150 MHz. For every cycle, an FFT is computed, yielding four spectral channels, which are then grouped to obtain the 2048 frequency channels comprising a complete spectrum. This calculation is executed for all 4 antennas (the three sub-arrays and the reference antenna). Additionally, to enhance the FFT result, a polyphase filter bank (PFB) block is employed beforehand. This block filters the signal from the ADCs based on phase, thereby improving the FFT response.

- **Dedispersors** These eleven blocks were designed to apply the technique of incoherent dedispersion, which essentially involves applying real-time delays to the dispersed signal, depending on the dispersion measure (DM) being targeted. In particular, ARTE has implemented this for the following dispersion measures 45, 90, 135, 180, 225, 270, 315, 360, 405, 450, and 495.
- **RFI Ranking** This block performs various statistical calculations based on data from the reference antenna and the antenna array, correlating and autocorrelating the information. The detailed development of this analysis can be studied in the undergraduate thesis [34].
- **Log files** This is the name given to the files saved to disk, which contain the information of integrated spectra every ten millisecond. Specifically, only the spectrum of the synthesized beam is stored. This data is transmitted over optical fiber.

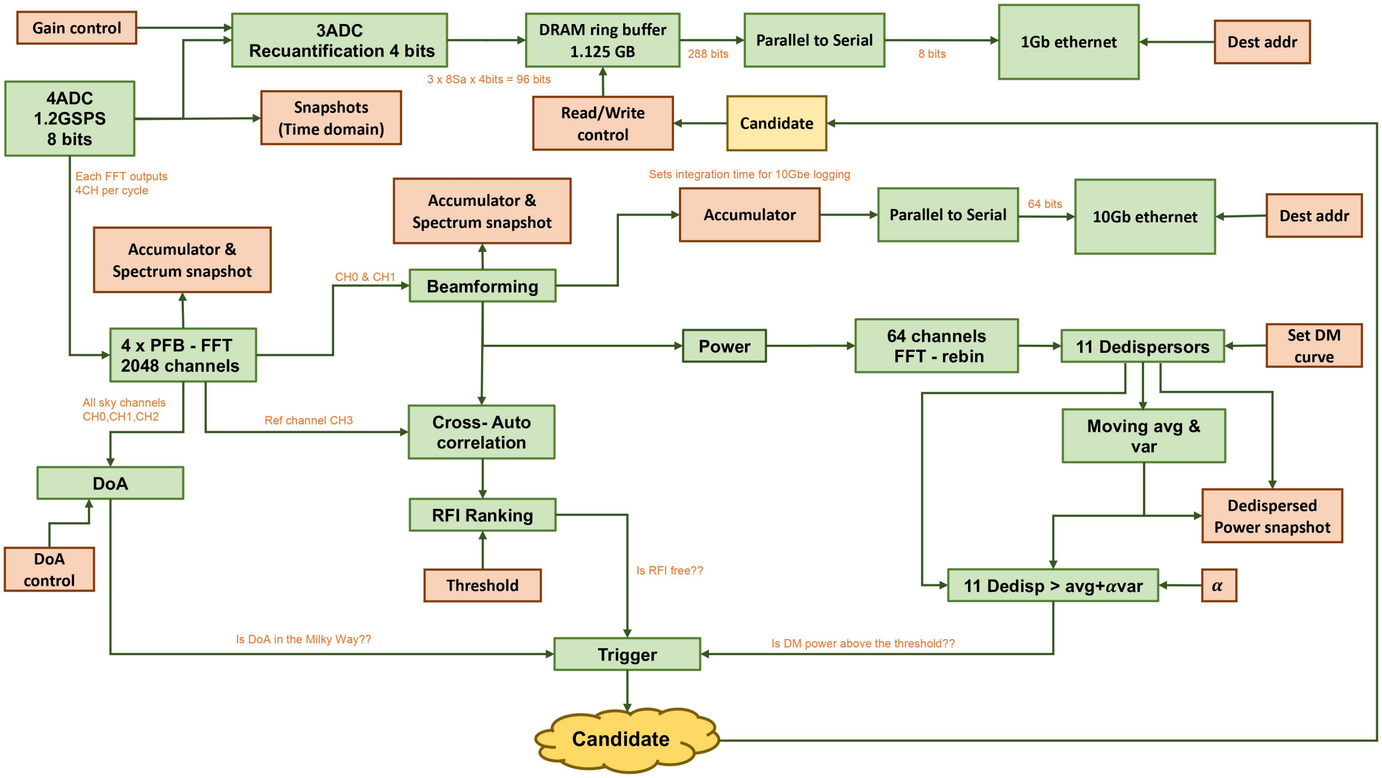

Figure 3.24: Backend's detailed block diagram

In the block diagram shown in Figure 3.24, three color classifications are presented. The green boxes represent implemented blocks, the orange ones denote signal control blocks that interact directly with the user, and the yellow blocks correspond to potential detection candidates.

The diagram in Figure 3.24 provides a more detailed explanation of Figure 3.23 and is read from left to right.

To begin, there are four ADCs, each sampling at a rate of 1.2 GSPS (Giga Samples Per Second). Eight bits are used to sample the signals from the subarrays. If we continue the analysis from the top part of the diagram, a process of re-quantization takes place. Instead of using 8-bits to describe the signals, only 4-bits are employed to provide more space for data storage. This requantized data contains temporal signal information and is saved in a ring buffer (a ring memory topology) in case the necessary conditions for considering a detection candidate are met. The amount of data stored in the ring buffer is 1.125 GB and is subsequently written to disk at a rate of 1 GB per second via the V6NET connector directly from the FPGA to the computer where data analysis will occur.

Moving on to the second branch originating from the ADCs, the signal is digitized and then passes through a PFB and FFT stage, resulting in a frequency domain signal composed of 2048 frequency channels. It's worth noting that the FFT is applied in every clock cycle of the FPGA and provides 4 spectral channels per cycle.

These 2048 spectral channels are simultaneously used for three distinct operations. The first operation considers the information from all three subarrays and feeds into the DoA detection algorithm. The same information from the three subarrays enters a beamforming block, where the complex sum of the signals from subarrays one and two is performed to synthesize the main beam. This beam has an elongated radiation pattern for observing the center of the galaxy. Additionally, the signal resulting from the complex sum enters a cross-correlation and auto-correlation block, where it is correlated with the spectra from the reference antenna and with itself. This correlation process is used by the RFI Ranking block to determine whether the signal originates from celestial sources or is the result of interference due to radio frequency.

Furthermore, after the complex sum is computed, signal accumulation occurs in 10-millisecond periods. These accumulated spectra are stored in log files and sent to disk at a rate of 10 GB per second via optical fiber.

On another note, the signal obtained from the complex sum at the output of the beamforming block undergoes power calculation and is reduced from 2048 spectral channels to 64 channels. It then enters the dedispersion block, which includes eleven dedispersers. These dedispersers apply the technique of incoherent dedispersion in real-time, which essentially involves delaying the signal by time intervals dependent on the dispersion measure (DM) to be detected. The dedispersed power is subject to a moving average and variance calculation to obtain a variable threshold. This threshold is compared with the power of the dedispersed signal for each DM. Finally, it reaches a trigger block, which, along with information from the RFI ranking and DoA, provides a candidate for a possible FRB detection.

3.1.9 Post processing

The post-processing of ARTE data currently relies on the development of two codes. One is designed for the visualization of spectrograms, where various image processing techniques are applied to enhance the graphics in a way that makes them sensitive to different signals of interest while reducing noise presence. Additionally, it includes average power plots with indicators of ADC saturation.

On the other hand, there is a transient detection algorithm that classifies different candidates into categories of interest, which are stored in separate folders for subsequent analysis. This algorithm

underwent evaluation by measuring the detection percentage, achieved by injecting synthetic FRBs into the system and triggering FRBs generated by an arbitrary signal generator.
It's worth mentioning that these analyses are performed using the $logfiles$ corresponding to spectra stored at a sampling rate of $\frac{1}{10\mathrm{ms}}$.
For more details about the back-end models and offline processing, see [35].

3.1.10 Assembly

At this stage, each of the subsystems detailed earlier are integrated. To reduce RFI, two Faraday cages are constructed to electromagnetically isolate the CPU, router, and screen in one cage, and in the other, the Rigol power supply for the receivers and the rack containing the receivers and the ROACH. Additionally, these cages are situated within a partially shielded office, lined with aluminum. Lastly, an air conditioning unit (AC) is positioned outside the office due to the presence of RFI identified as a result of its usage.

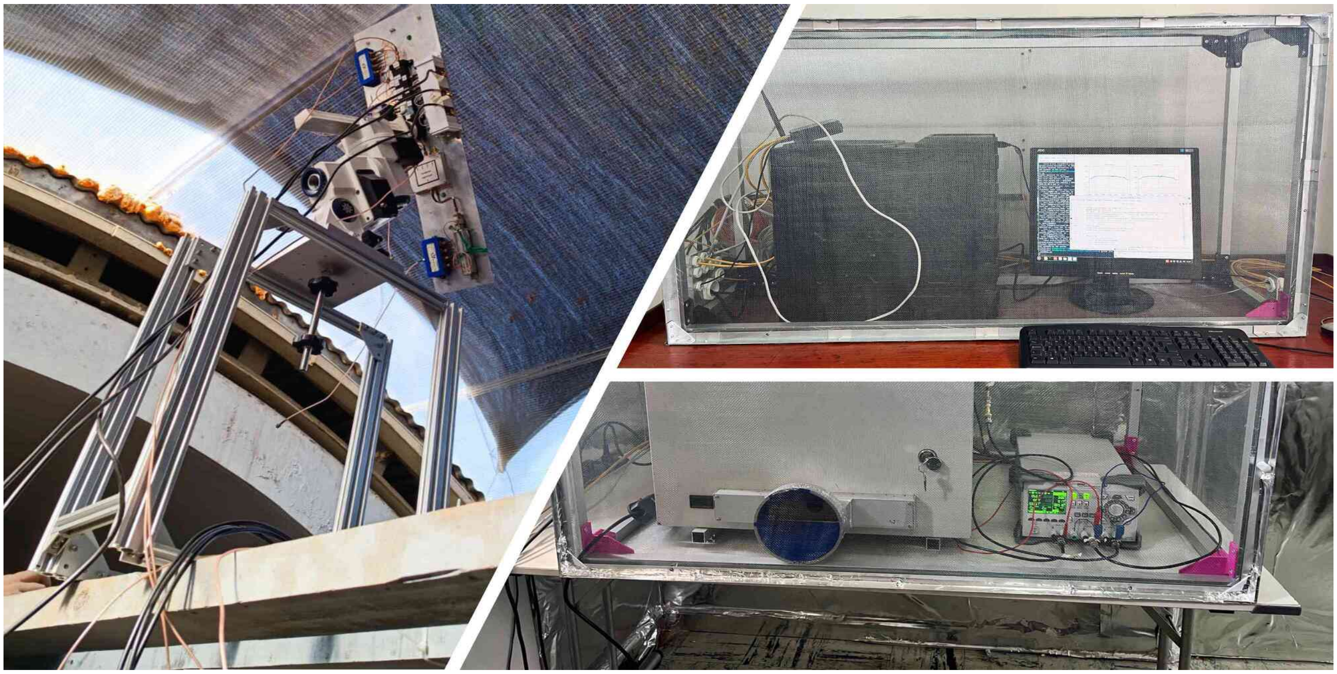

Figure 3.25: Final assembly of the ARTE radio relescope located at the national astronomical observatory

3.2 RFI measurements

This section presents the results of Radio Frequency Interference (RFI) measurements conducted at two astronomy-dedicated sites. The first site analyzed is the National Astronomical Observatory (OAN) [1], located on Cerro Calán, the primary candidate for ARTE installation. The second measured site was the University Católica Observatory (OUC) [2], situated on Hacienda Santa Martina.

---

[1] http://www.oan.uchile.cl/

[2] https://astro.uc.cl/observatorio-uc/

Figure 3.26: Left: National Astronomical Observatory. Rigth: University Católica Observatory.

3.2.1 RFI measurements setup

This RFI measurement was made with two antenna types, an omnidirectional and an antenna array. The measurement was conducted in a band from 1.2 – 1.8 GHz, the filter bandwidth of the microwave receiver, and the ARTE's operational bandwidth. Moreover, the spectrums were logged each 10 ms with ROACH. The chain of the microwave was formed for two amplifiers, two passband filters, and an equalizer, shown in Figure 3.27b.

Based on the Friis equation, the theoretical noise temperature of the receiver chain is given by,

$$\mathrm{T_{rx}} = \mathrm{T_{ULN}} + \frac{\mathrm{T_{F_1}}}{\mathrm{G_{ULN}}} + \frac{\mathrm{T_{LNA}}}{\mathrm{G_{ULN}} \cdot \frac{1}{\mathrm{L_{F_1}}}} + \frac{\mathrm{T_{F_2}}}{\mathrm{G_{ULN}} \cdot \frac{1}{\mathrm{L_{F_1}}} \cdot \mathrm{G_{LNA}}} + \frac{\mathrm{T_{EQ}}}{\mathrm{G_{ULN}} \cdot \frac{1}{\mathrm{L_{F_1}}} \cdot \mathrm{G_{LNA}} \cdot \frac{1}{\mathrm{L_{F_2}}}} \tag{3.18}$$

And, the gain of the amplification chain is given by,

$$\mathrm{G_{rx}} = \mathrm{G_{ULN}} - \mathrm{G_{filter}} + \mathrm{G_{LNA}} - \mathrm{G_{filter}} - \mathrm{G_{EQ}} \tag{3.19}$$

$$\mathrm{G_{rx}} = 14.8 - 1.6 + 43 - 1.6 - 9 = 45.6[\mathrm{d}B] \tag{3.20}$$

The receiver noise temperature shown in Figure 3.28 is close to 100 K. Furthermore, the S21 parameter of the receiver has a value close to 45.4 dB, which is consistent with the theoretical calculation shown in equation 3.20.

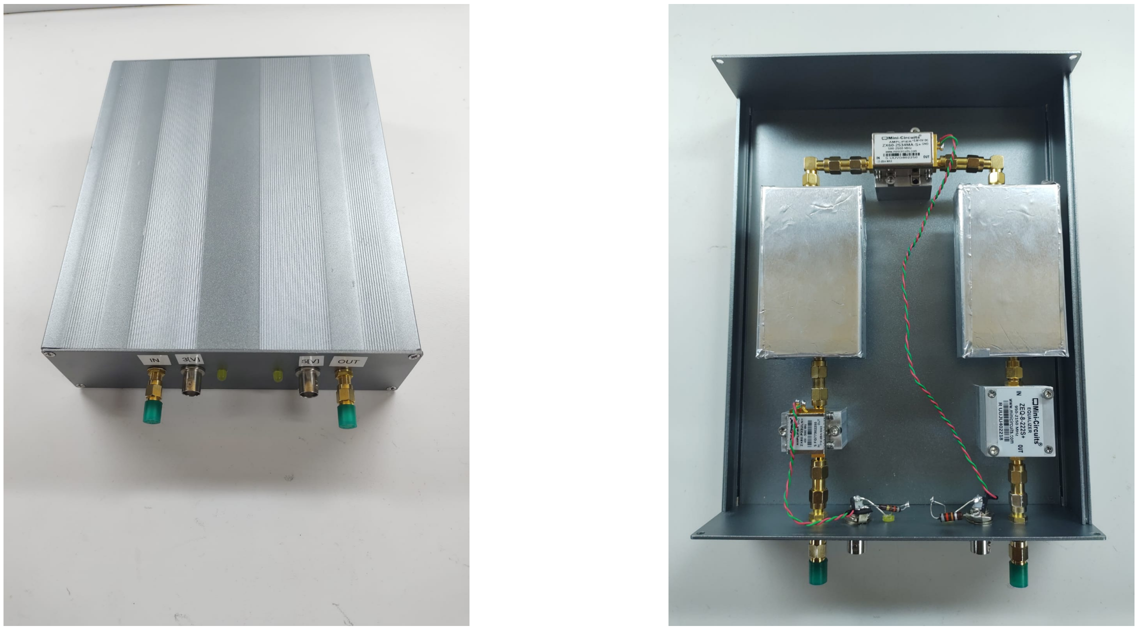

(a) Microwave receiver.

(b) Top view microwave receiver

Figure 3.27: Microwave receiver used at Cerro Calán and Santa Matina RFI measurement

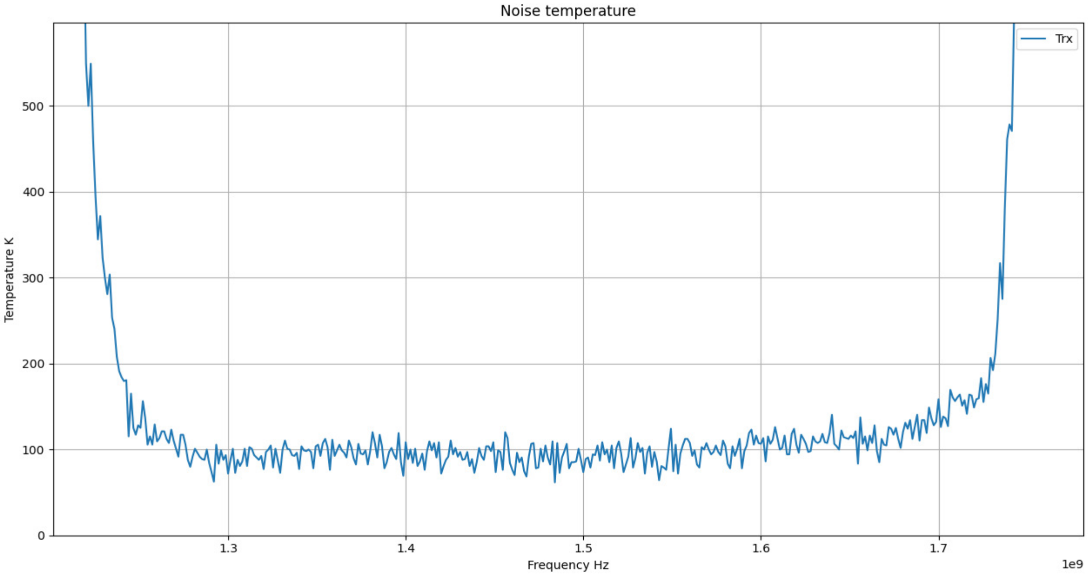

Figure 3.28: Noise temperature

3.2.2 Omni-directional versus array antenna

The reflection coefficient of the omni-directional antenna Figure 3.29a can be seen in Figure 3.29b. The results of the first measurements are shown in Figure 3.30.

From these measurements, it is clear that at the Santa Martina site, the RFI is significantly lower than the RFI at the Cerro Calán site. Even in the rejection areas of the filter, RFI can be seen at Cerro Calán. For this reason it was necessary to apply many techniques to reduce the RFI in the ARTE band, and for future work will mount another radio telescope at Santa Martina Observatory.

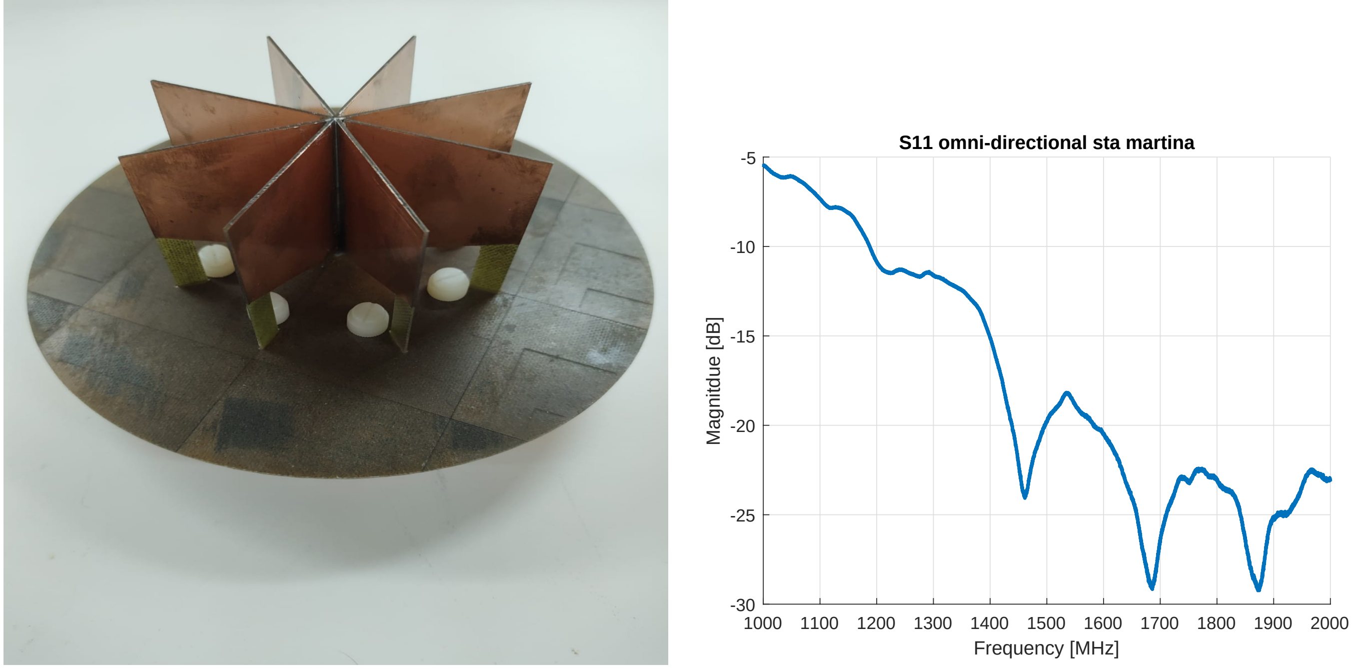

(a) Used omni antenna for measurements.

(b) Input reflection coef of Omni antenna used.

Figure 3.29: Indicating antenna used for RFI measurements and its reflection coefficient over the used frequency band.

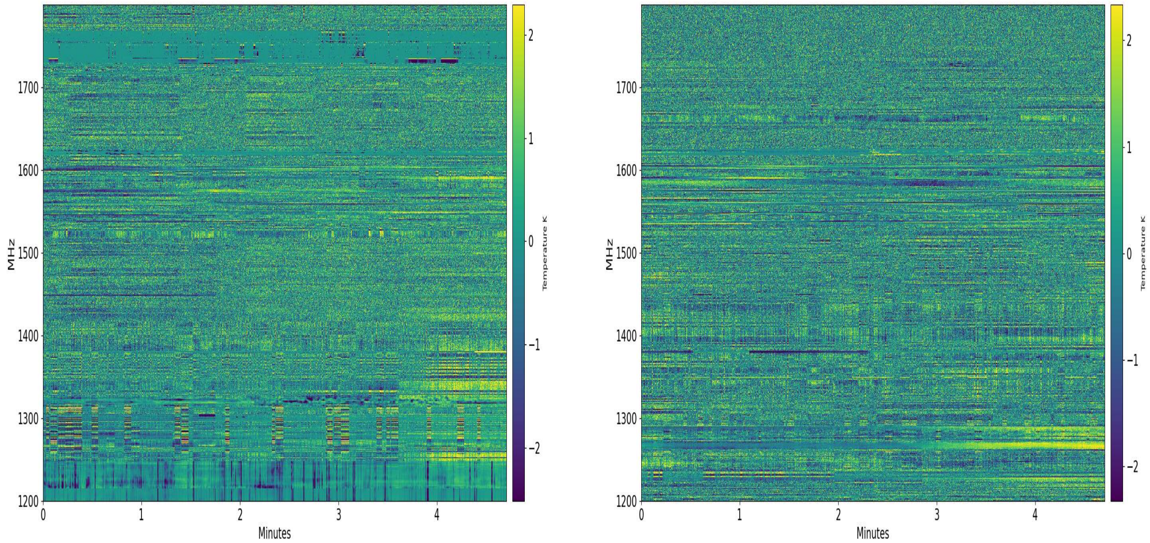

(a) RFI spectrum obtained at Cerro Calán

(b) RFI spectrum obtained at Sta Martina

Figure 3.30: RFI measurement results at Cerro Calán and Santa Martina using the omnidirectional antenna.

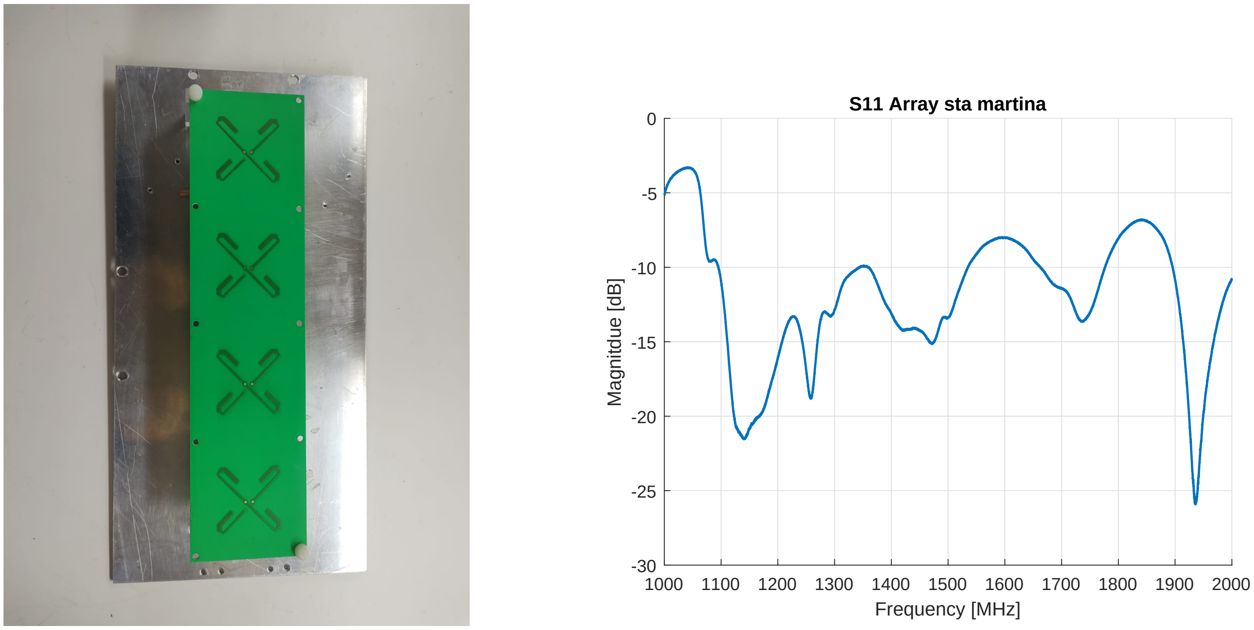

(a) Used antenna array for measurements. (b) Input reflection coef of an array antenna used.

Figure 3.31: Indicating antenna used for RFI measurements and its reflection coefficient over the used frequency band.

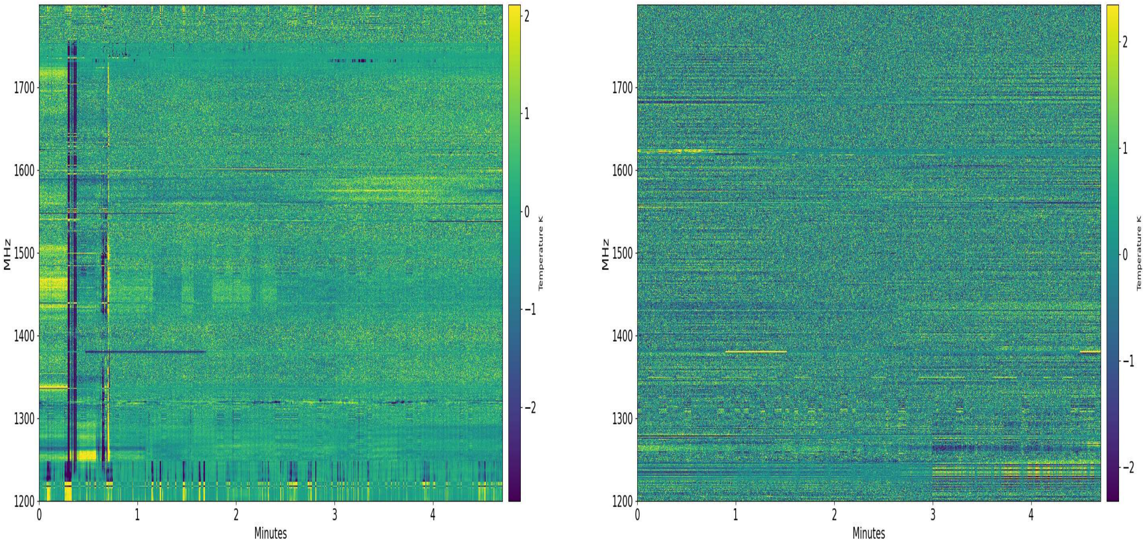

(a) RFI spectrum obtained at Cerro Calán (b) RFI spectrum obtained at Santa Martina

Figure 3.32: RFI measurement results at Cerro Calán and Santa Martina using the array antenna.

Chapter 4

Technical and instrumental challenges

4.1 Introduction

Throughout the integration of each subsystem, as briefly described in Chapter 3, various challenges emerged that were not extensively explored. Therefore, this chapter documents some of the technical and instrumental difficulties. It provides a reference to resolve them in the future or for potential developments when encountering similar issues.

4.1.1 RFI mitigation and coupling

In this subsection, we address the primary issue identified during the operation of the radio telescope and discuss various hardware techniques implemented to mitigate undesired radio frequency interference (RFI).

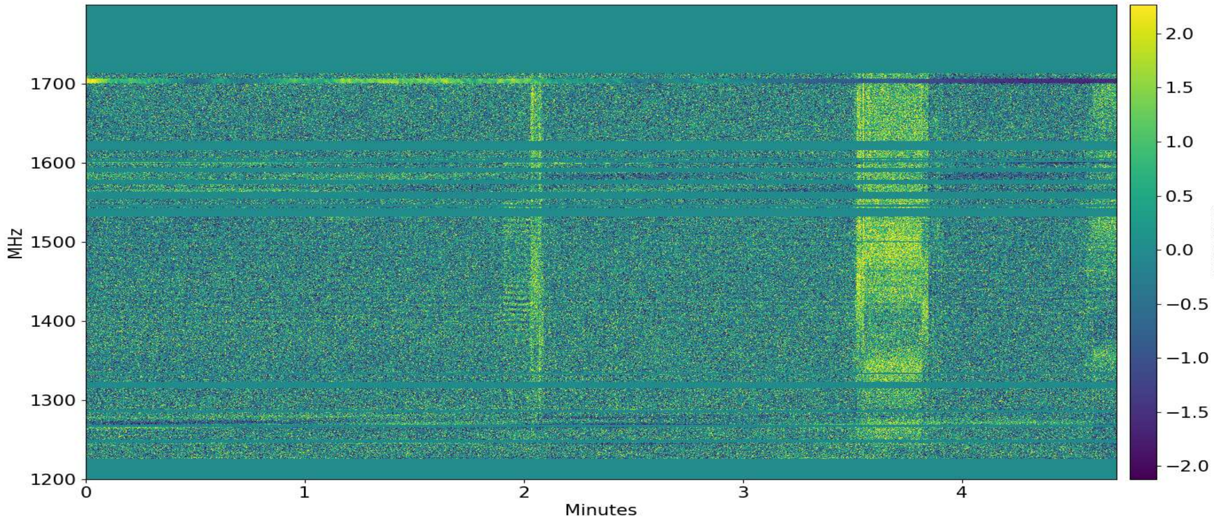

Figure 4.1: Spectrogram depicting radio frequency interference (RFI).

First of all, electronic feedback between the microwave receiver and the antenna was detected.

As a result, it was decided to separate them by a distance exceeding ten meters. Additionally, electromagnetic isolation of equipment was developed by constructing Faraday cages. Furthermore, cable shielding was employed, with segregation based on power, data, and RF signal cables. In conjunction with these measures, the rack was positioned (housing ROACH2 and microwave receivers) within a completely isolated office space, as illustrated in Figure 4.2.

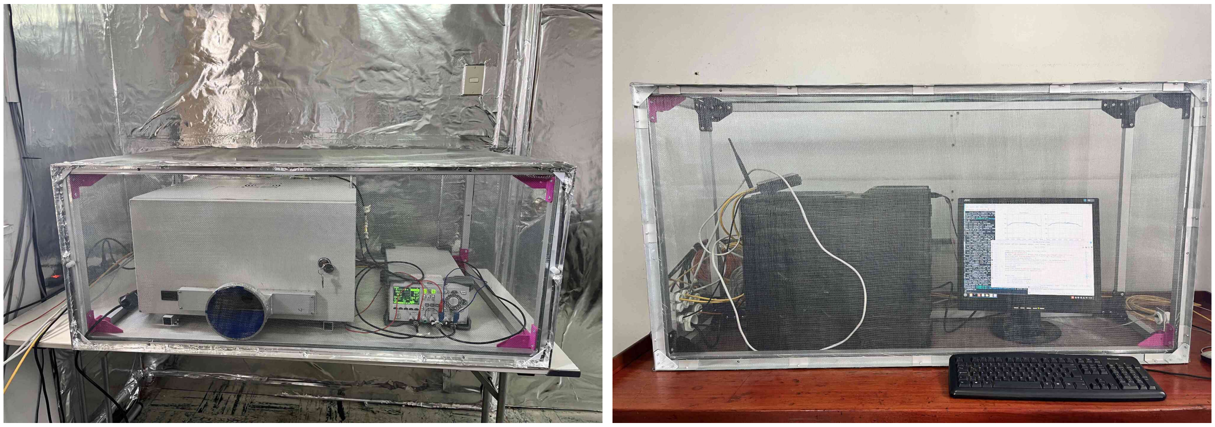

(a) Receiver, ROACH2 and power supply.

(b) CPU, monitor, and router.

Figure 4.2: Two Faraday cages built to isolate the above equipment.

It is of no surprise that the antenna from the microwave receivers at a greater distance entailed an increase in the system's noise temperature. Consequently, this necessitated a modification to the microwave receiver hardware, as detailed in Chapter 3. This modification involved relocating the first amplifier immediately after the analog combination of each sub-array. Subsequently, a twelve-meter-long SMA LM200 cable was extended to connect the remaining chains.

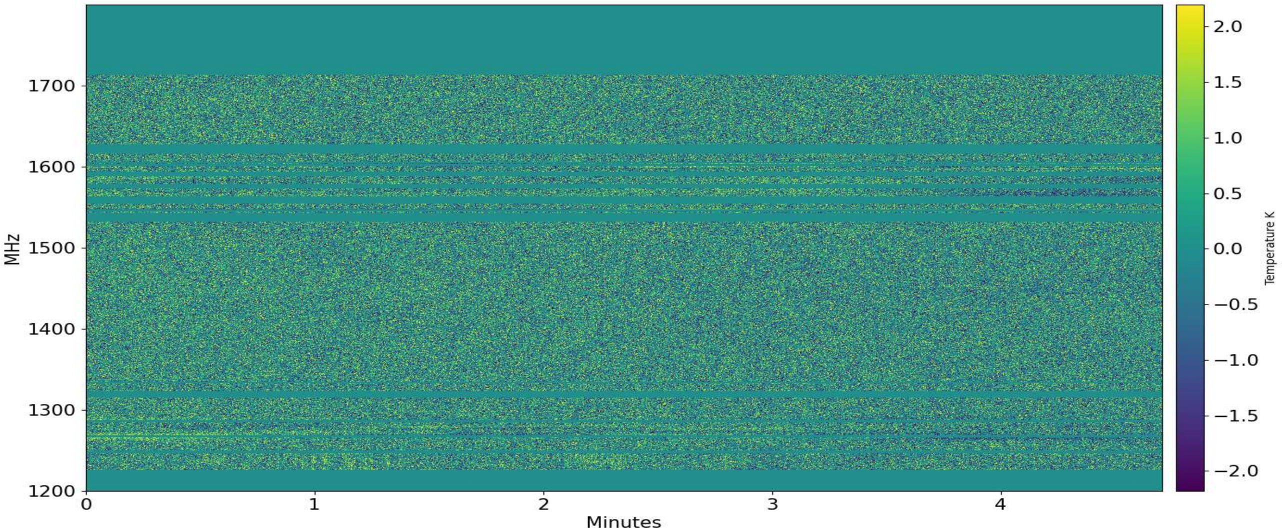

Figure 4.3: Clean spectrogram in the bandwidth of interest with flagged zones.

While many of the events generating RFI were mitigated through the aforementioned and detailed setup modifications some RFI remains. This is especially true concerning sudden RFI occurrences, as mentioned earlier. These events have the potential to trigger false positives in a regular basis when activating the dedispersers.

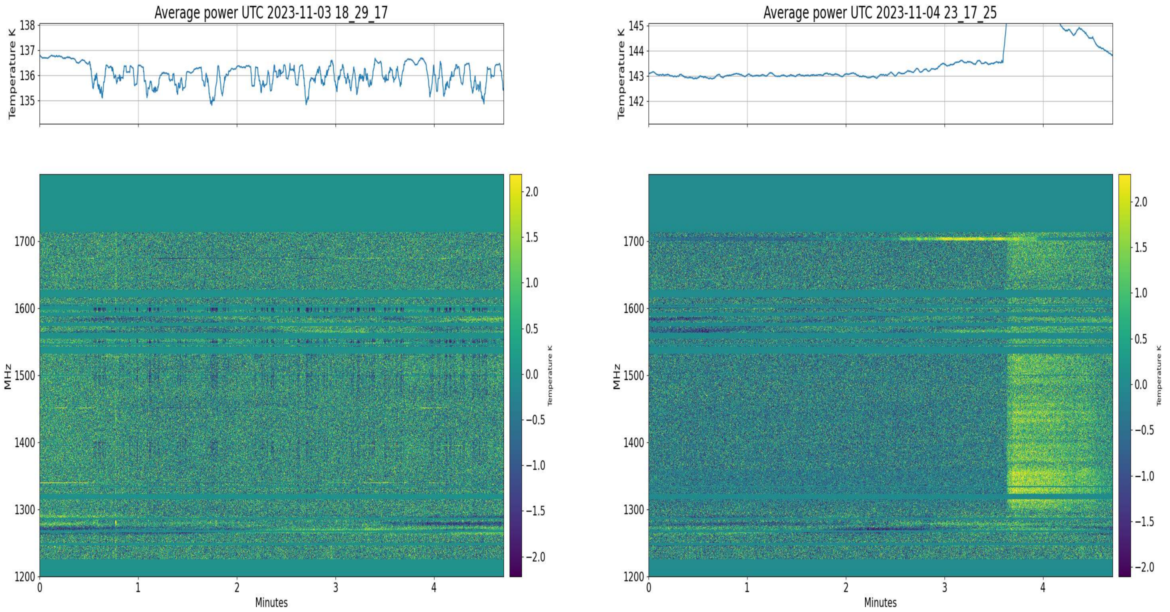

(a) Intermittent and strong RFI event.

(b) Strong and long RFI event

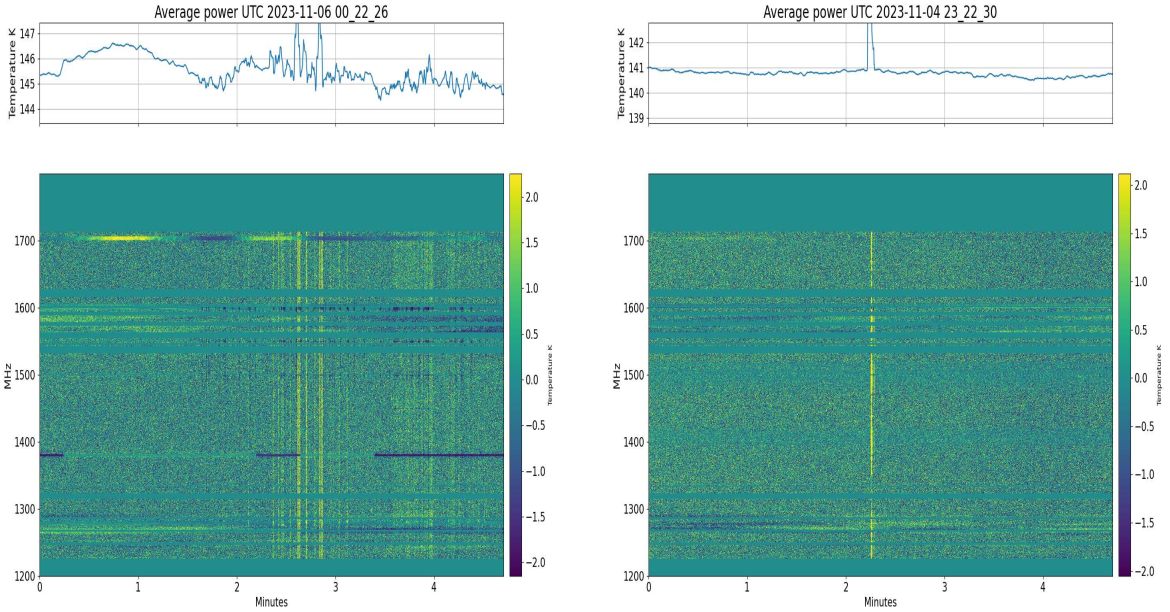

(c) Intermittent and soft RFI event.

(d) Single and strong RFI event.

Figure 4.4: Different spectrograms with RFI events

4.1.2 Data loss

This subsection addresses the issue of data loss that occurred during the operation of the ARTE radio telescope. To identify the data loss and subsequently debug where the transmission problem was occurring, a series of analyses had to be conducted.
Initially, the spectrograms depicting data loss appeared as shown in Figure 4.5, in contrast to regularly obtained spectrograms as depicted in Figure 4.6.

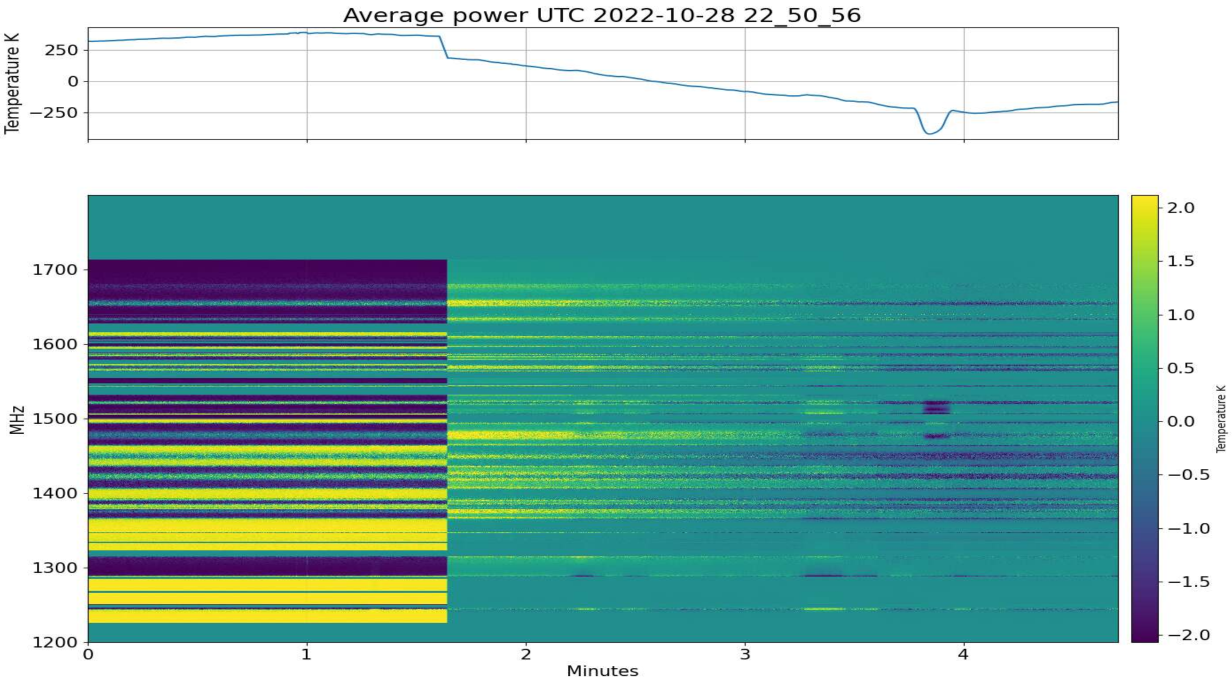

Figure 4.5: Spectrogram with a clear time incoherence due to data loss.

In Figure 4.5, the upper panel of the average temperature illustrates an oscillation of the noise temperature around 250 K during the first minute and a half. Suddenly, it sharply drops to negative temperatures, which is unrealistic. This anomaly is also evident in the spectrogram, where a clear inconsistency exists between the first minute and the rest of the time. It is worth mentioning that after a couple of months of relatively stable measurements, as shown in Figure 4.6, these phenomena shown in 4.5 began to occur, leading to a possible attribution of data loss given the abruptness of the variation.

Later, to validate the hypothesis regarding data loss, headers were incorporated into the $log files$, indicating whether the data had experienced packet loss during transmission or not, as depicted in the plots in 4.7.

Armed with this information, it became feasible to commence hardware debugging to identify the malfunctioning device. The initial culprit focused on the optical fiber, but the issue persisted. Consequently, a decision was made to replace the network card, ultimately resolving the data loss problem.

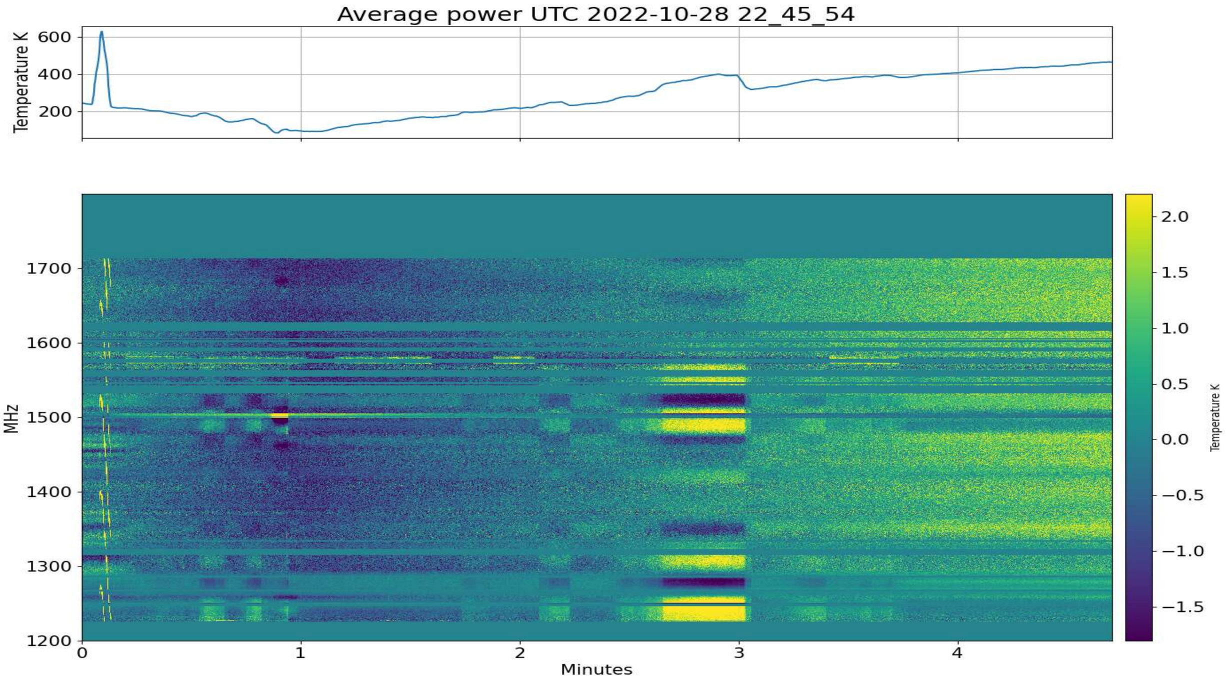

Figure 4.6: Spectrogram with coherence in time, but with some RFI events.

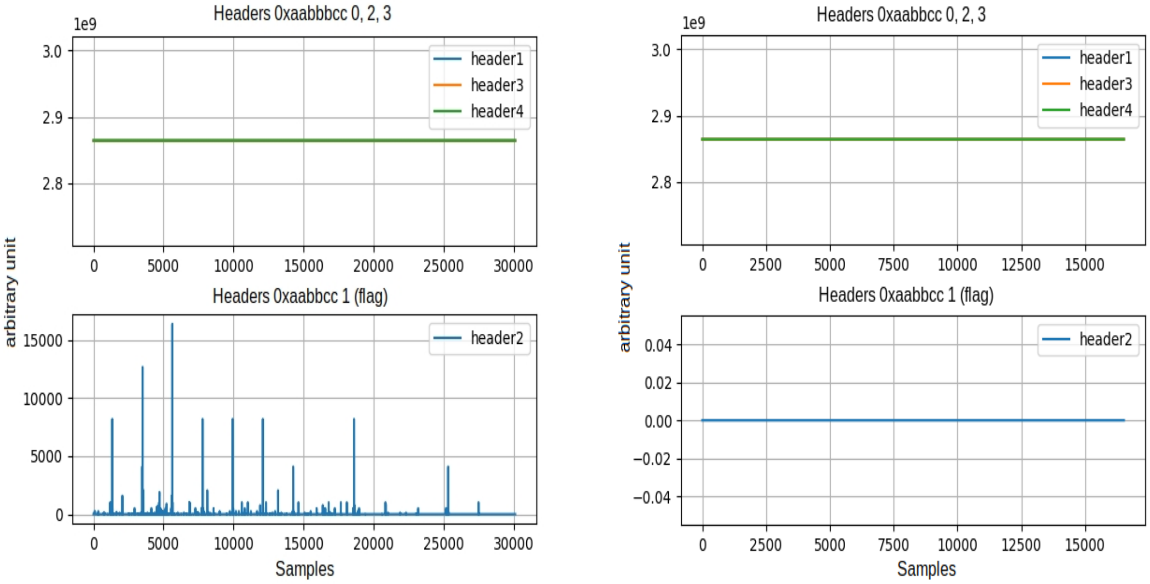

(a) Header in a data loss case

(b) Header without data loss

Figure 4.7: Plots of the headers in both cases

4.1.3 Cooling system

As mentioned in the literature review chapter, the radio telescope's back-end was developed using FPGAs, which are programmable logic gate arrays known for their programming versatility and high computing capacity due to their ability to parallelize repetitive processes. However, a crucial issue arises from the fact that each logic gate is composed of semiconductors, which naturally dissipate energy in the form of heat. Consequently, a cooling system was implemented, primarily consisting of fans within the ROACH2 and a larger fan within the rack housing the microwave receivers and the ROACH2. Despite these cooling systems, temperature escalation became problematic, with the FPGA reaching temperatures close to 70°C, exceeding the optimal operating range. Consequently, after monitoring the temperature of key devices within the radio telescope, the integration of an air conditioning unit became necessary to maintain the appropriate temperature for correct operation.

A dedicated cooling unit was chosen for the rack containing the electronics requiring operation within specific thermal parameters. Initially, an aluminum tube was used to route air to the rack housing the microwave receivers and the ROACH2. The cooling measure proved successful in achieving optimal temperatures, even on sunny days with maximum temperatures.

However, this setup modification introduced additional challenges related to radio frequency interference.

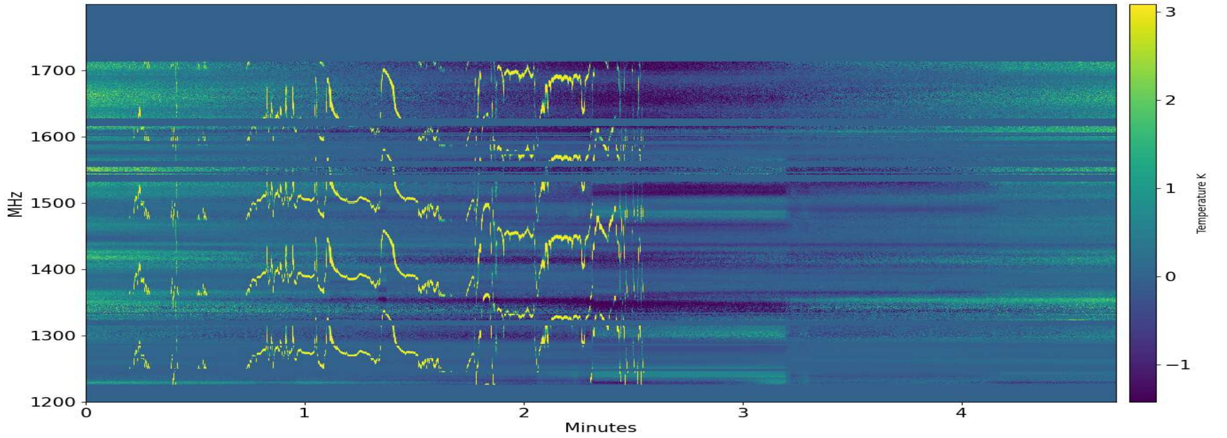

Figure 4.8: Example of air conditioning-induced RFI

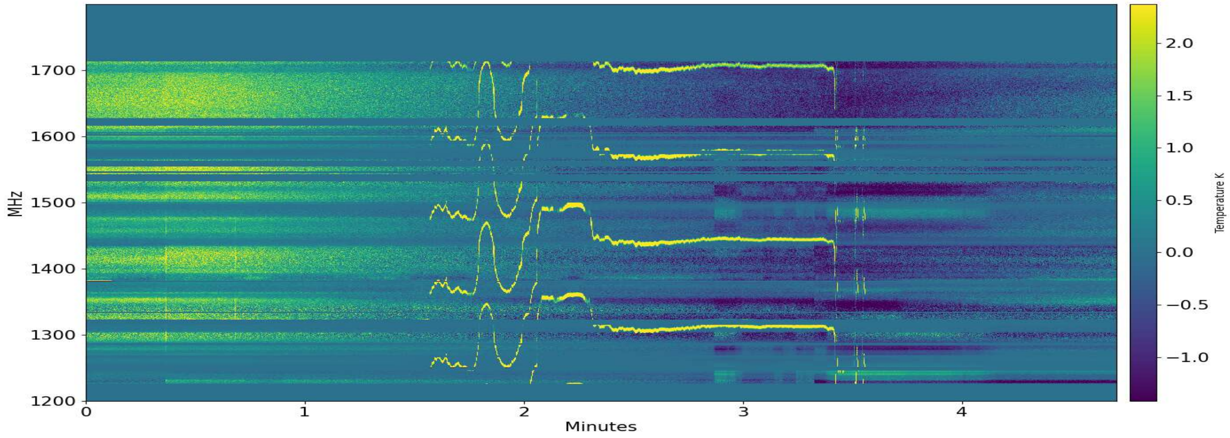

Figure 4.9: Example of air conditioning-induced RFI

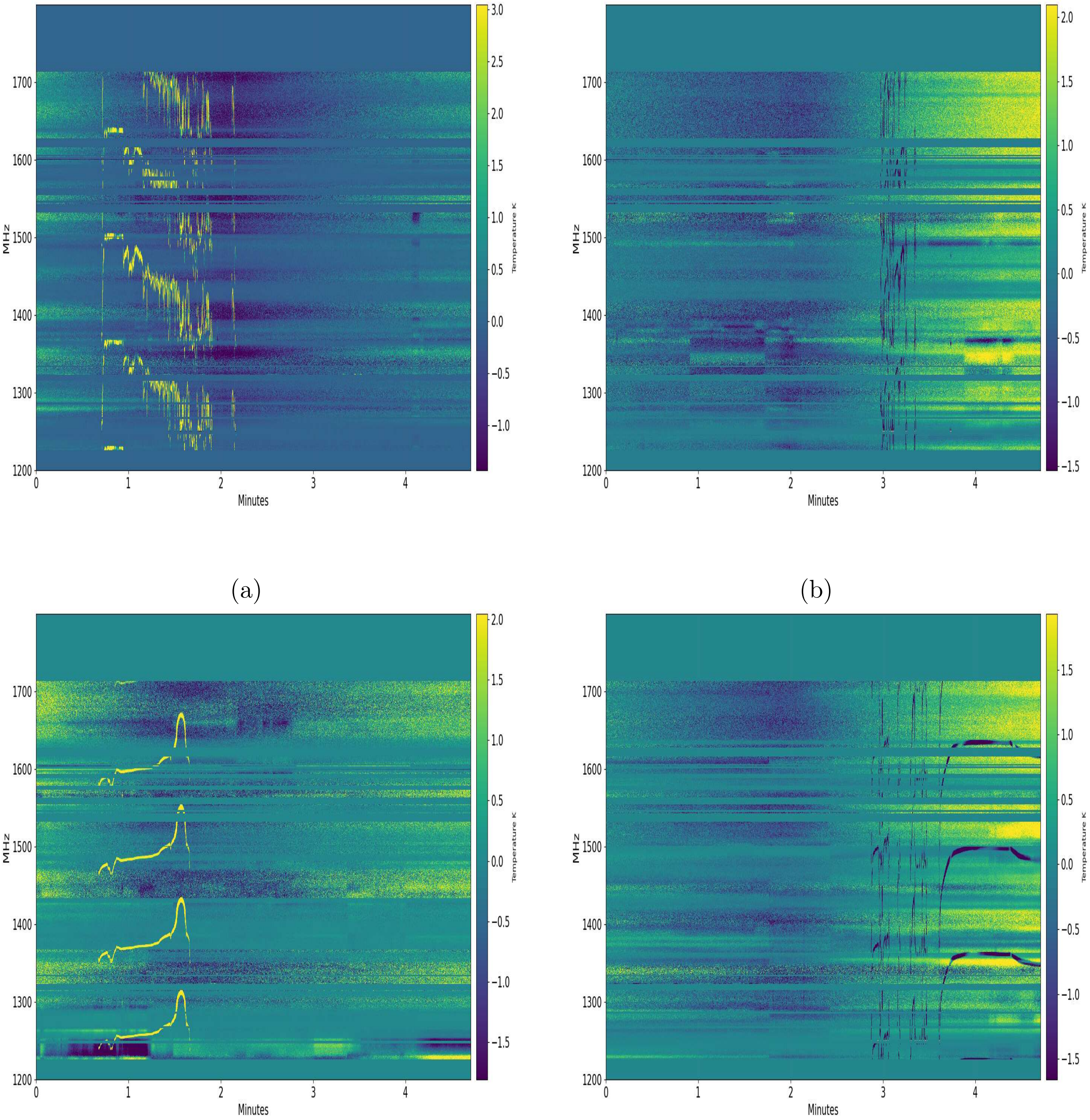

(a)

(b)

(c)

(d)

Figure 4.10: Examples of air conditioning-induced RFI

Chapter 5

Results and discussion

5.1 Introduction

This chapter presents the primary results from the operation of the ARTE radio telescope for approximately one year. It specifically addresses the detection of weather satellites, synthetic aperture radars, and various RFI detections associated with different devices, and concludes with the report of a solar flare detected within ARTE's operational band, with a spectral flux density approaching 10^4 kJy.

5.1.1 Synthetic aperture radar

This section presents the transit of the argentine satellite SAOCOM [1]. The SAOCOM 1 satellite mission has diverse objectives based on the synthetic aperture radar (SAR) information capabilities. It can independently measure meteorological conditions with a spatial resolution ranging from ten to one hundred meters at different observation angles. Among the valuable information derived from the radar data are soil moisture maps, which have various impacts on the population. Additionally, it has applications related to environmental emergencies, such as detecting hydrocarbon spills in the sea and monitoring water coverage during floods.

SAOCOM 1 is a microwave-range constellation consisting of two identical satellites, named A and B, respectively. SAOCOM 1A was launched on October 7, 2018, and SAOCOM 1B on August 30, 2020. Each satellite is expected to have an estimated lifespan of five years. Finally, it is noteworthy that this project is developed in collaboration with the Italian Space Agency (ASI).

Figure 5.1 illustrates SAOCOM 1-A, presenting the dimensions of its main components and some technical characteristics, such as weight and orbital period.

The main technical characteristics of the SAR are presented in Table 5.1.

Subsequently, in Figure 5.2, four spectrograms are presented, showcasing different observations of transits associated with the argentine satellite SAOCOM using the Synthetic Aperture Radar (SAR), each with varying durations and intensities.

---

[1] https://www.argentina.gob.ar/ciencia/conae/misiones-espaciales/saocom/objetivos

Figure 5.1: Reference illustration of SAOCOM satellite from [7].

Name	SAR polimetric L band
Description	Meteorological
Country	Argentina
Central frequency	1275 [MHz]
Spatial Resolution	10 to 100 [m]
Incidence Angle	20 to 50 [°]
Dynamic Range	-35 to 5 [dB]
Orbit	Heliosincrónica
Altitude	620 [Km]

Table 5.1: Key Parameters of the SAOCOM satellite

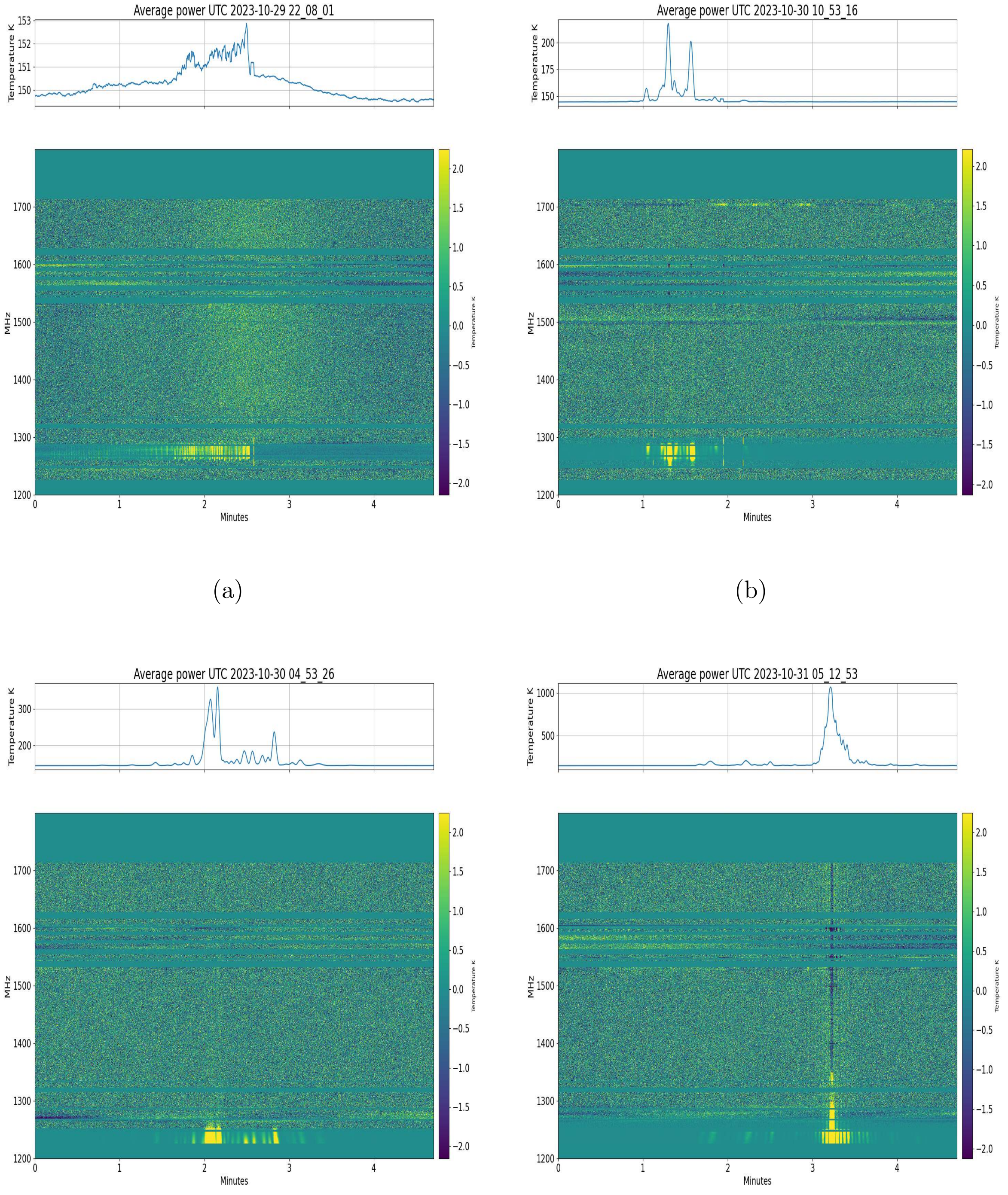

(a) (b)

(c) (d)

Figure 5.2: Four spectrograms showcasing different SAOCOM transits

5.1.2 Weather satellites

As mentioned earlier, the operational bandwidth of the ARTE radio telescope is 600 MHz, spanning from 1200 MHz to 1800 MHz. This characteristic enables the observation of various phenomena occurring within this frequency range. Throughout the measurements, ARTE detected several satellites, primarily dedicated to meteorological purposes, traversing the beam at intervals ranging from 2 to 5 minutes. These satellites were identified at frequencies approximately between 1.68 GHz and 1.74 GHz. Some of the identified satellites include NOAA-15, NOAA-18, NOAA-19, Metop B and C, METEOR M2 2, YUN HAI 1, etc. It's worth mentioning that each satellites belong to different countries, such as the USA, Russia, China, Argentina, etc.

Each of the analyzed satellites was subsequently compared with the information provided by the Orbitron software [2], which allowed for the association and identification of each satellite and the prediction of future transits to verify the classification made. It is worth noting that the in-depth analysis was conducted by a student and reported in [3].

This subsection presents four spectrograms depicting the transit of different weather satellites around 1700 MHz. Additionally, the respective curves of average temperature in Kelvin are shown, displaying a smooth pattern during the satellite's movement and reaching peak intensity when directly over the main lobe of the radio telescope's primary antenna.

Table 5.2 displays the satellites sighted by ARTE, which were also predicted using the Orbitron software. They are classified based on their country of origin, central operating frequency, bandwidth, and orbital period.

Name	Description	Country	Central frequency [MHz]	Bandwidth [MHz]	Period (Hrs:Min:Sec)
NOAA-15	Meteorological satellite	USA	1702.5	3	01:40:57
NOAA-18	Meteorological satellite	USA	1707	3	01:41:55
NOAA-19	Meteorological satellite	USA	1698	3	01:41:56
Metop B	Meteorological satellite	Europe	1701.3	6	01:41:18
Metop C	Meteorological satellite	Europe	1701.3	6	01:41:18
METEOR M2 2	Meteorological satellite	Russia	1700	3	01:41:08
YUN HAI 1	Meteorological satellite	China	1704	4	01:40:39
YUN HAI 1-02	Meteorological satellite	China	1704	4	01:40:30
YUN HAI 1-03	Meteorological satellite	China	1704	4	01:40:30
Saocom 1A	Observation	Argentina	1275	150	01:37:09
ALOS-2	Observation	Japan	1236*	42*	01:37:19

Table 5.2: Satellites general information [3].

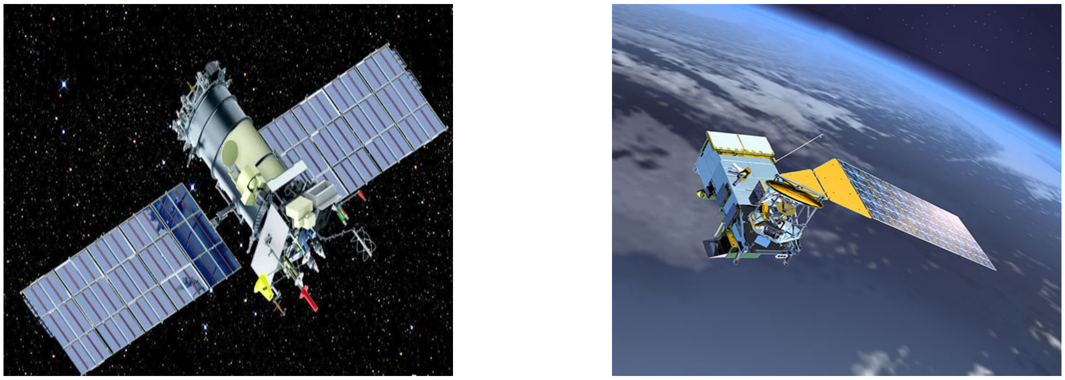

(a) Rusian Satellite METEOR [36]

(b) American Satellite NOAA [37]

Figure 5.3: Ilustrative image from both weather satellites

---

[2] http://www.stoff.pl/

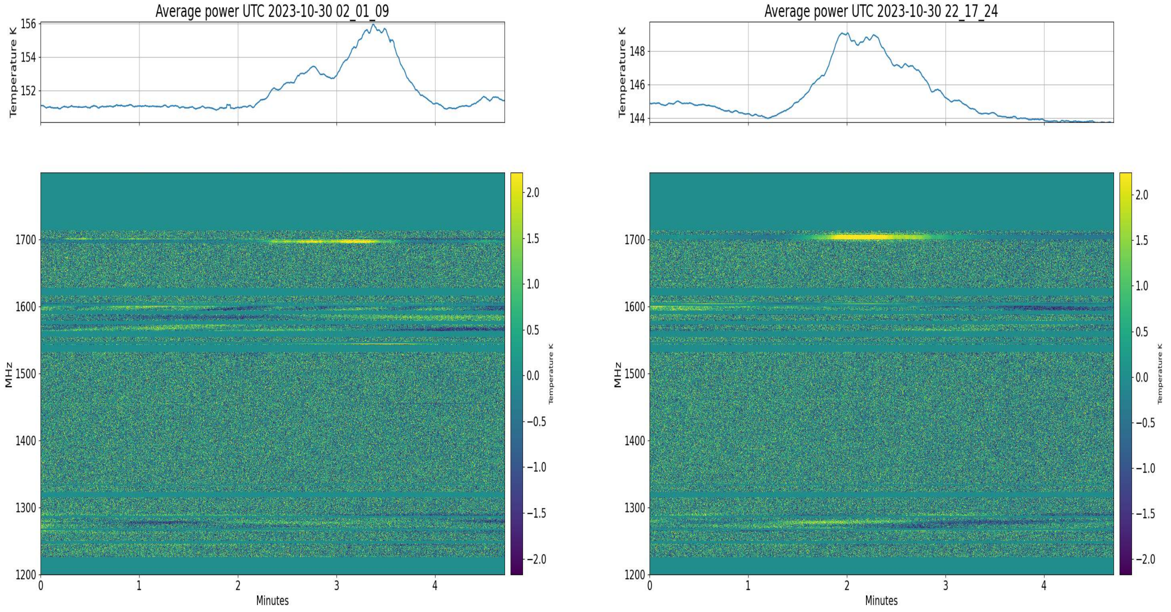

(a) October 29th

(b) October 30th

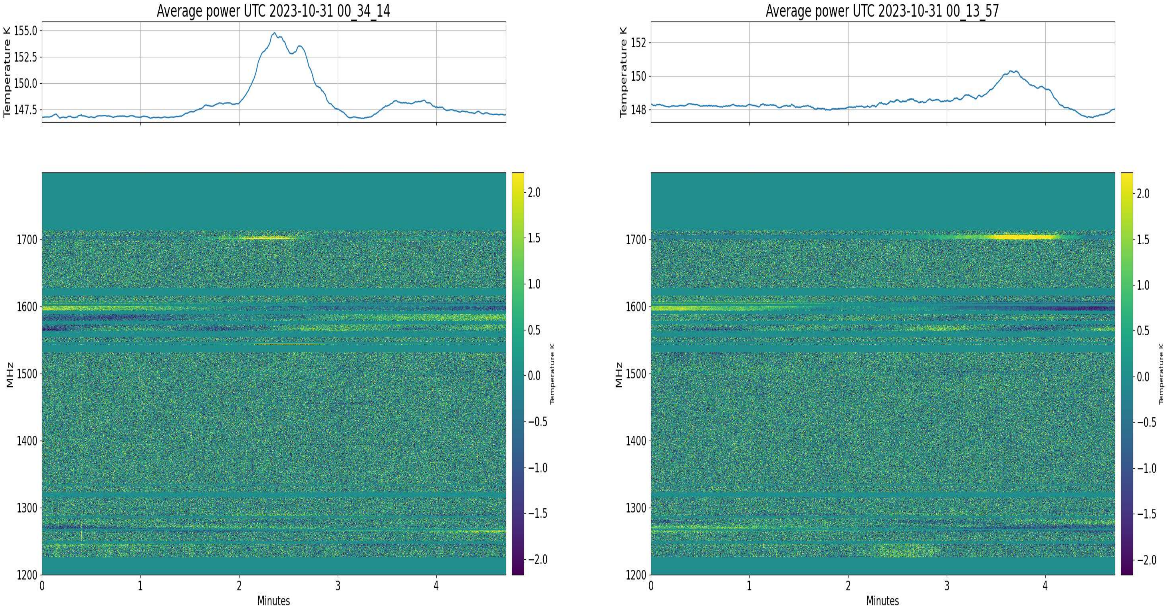

(c) October 30th

(d) October 31

Figure 5.4: Examples of different weather satellites transits

5.1.3 RFI

This subsection presents some of the most interesting detections classified as radio frequency interference (RFI). While the previous chapter had a dedicated section on RFI, focusing on solutions for mitigating these unwanted signals, this section showcases results from observations on various measurement days. These observations are linked to man-made signals, both intentional, such as those from cell phones, and unintentional, like effects produced by the air conditioning unit (AC).

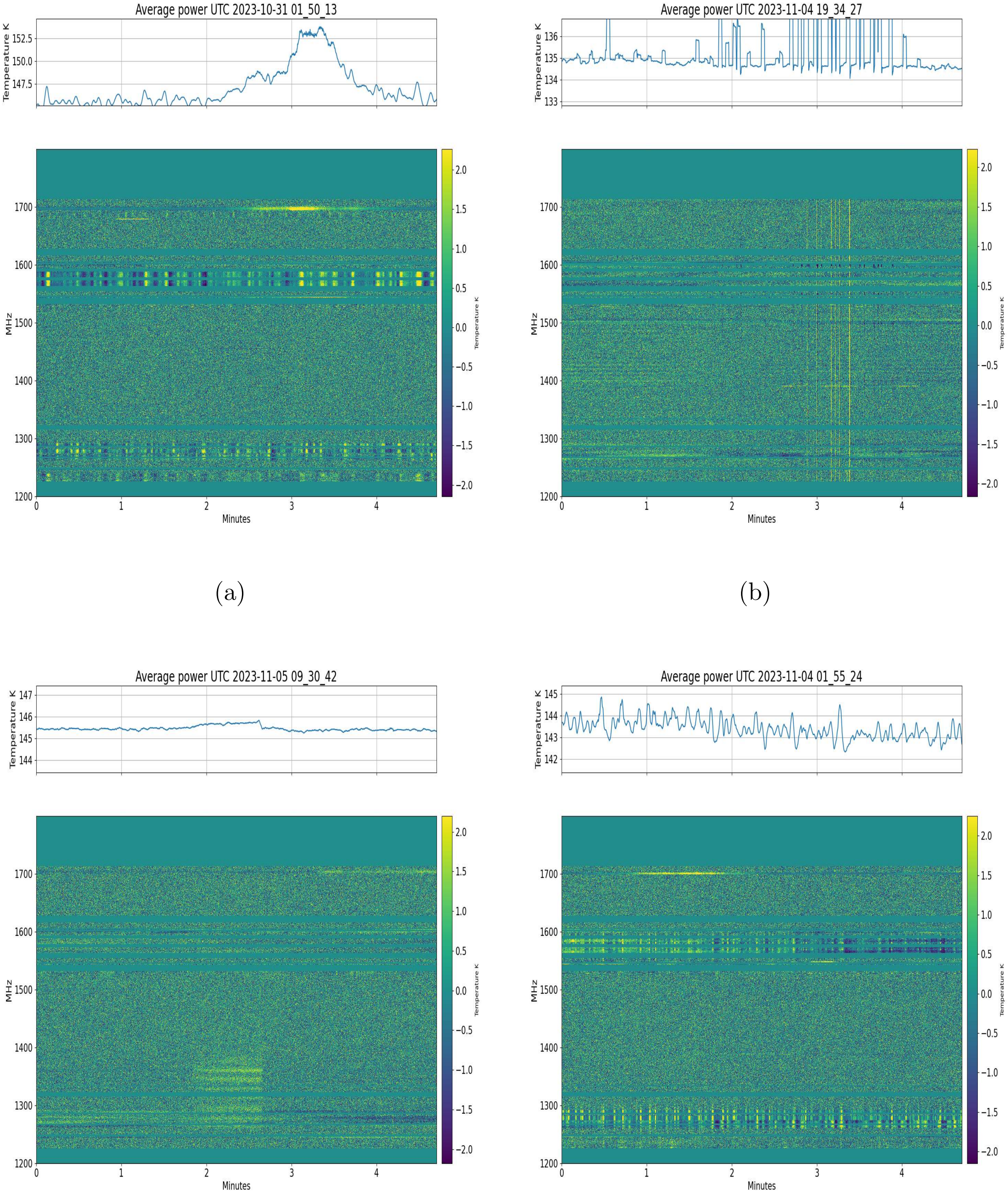

(a) (b)

(c) (d)

Figure 5.5: Examples of different RFI events for different frequencies.

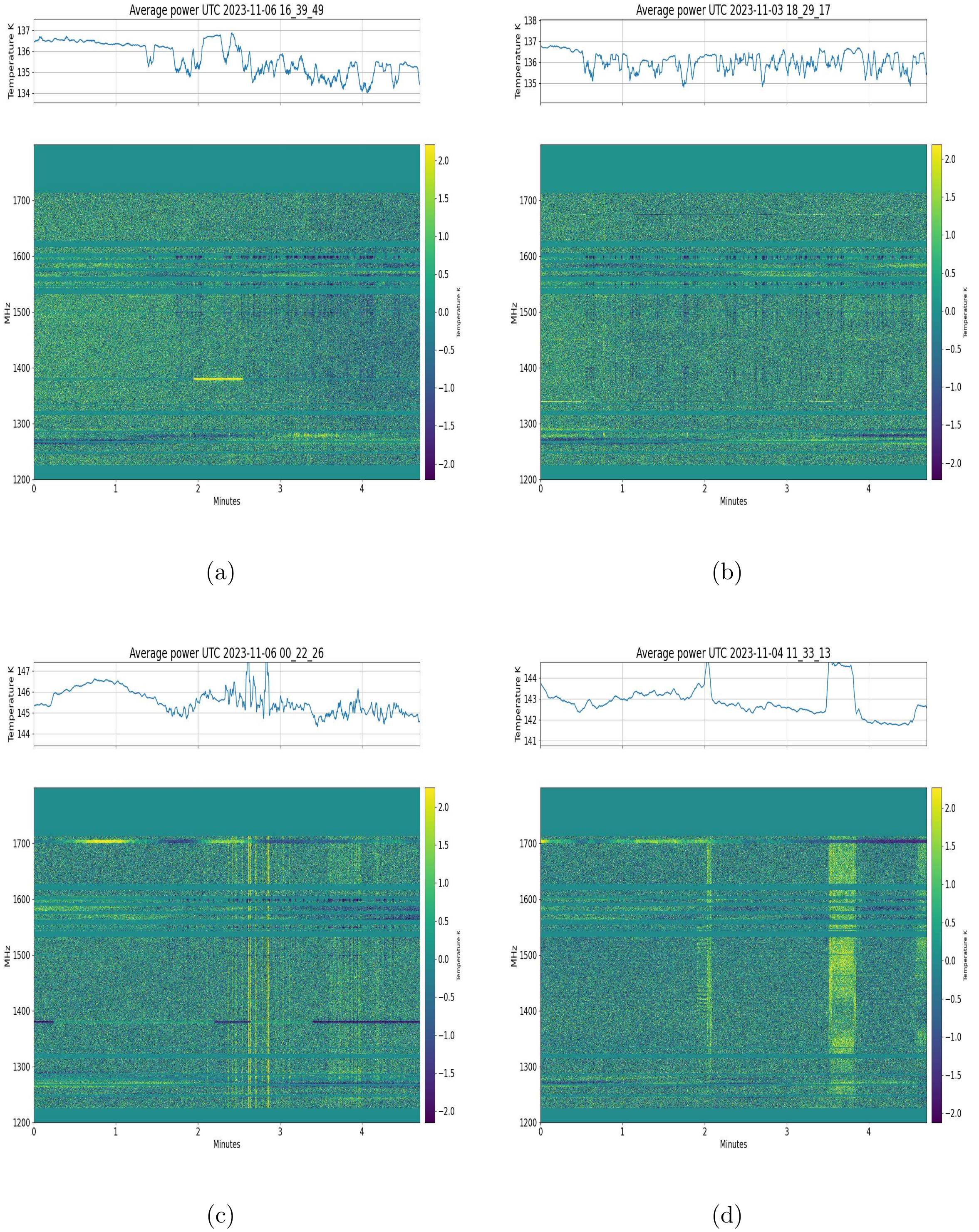

(a) (b)

(c) (d)

Figure 5.6: Examples of differents RFI events for differents frequencies.

5.1.4 Solar flare

This section presents the first astronomical result observed by the ARTE radio telescope during May 2023. It corresponds to a long-duration solar flare, M4.2 GOES class, observable across the

entire L-band, with a peak spectral density flux exceeding 10^4 kJy at around 1212.7 MHz.
In Figure 5.7, the upper part displays the solar dynamic spectrogram of the event measured by the ARTE radio telescope in Kelvin. It is worth mentioning, that the compressed spectrogram of approximately 35 minutes of observation is depicted, highlighting the event. Meanwhile, on the lower side, the EOVSA solar dynamic spectrogram is shown, obtained using the available EOVSA data from [3].

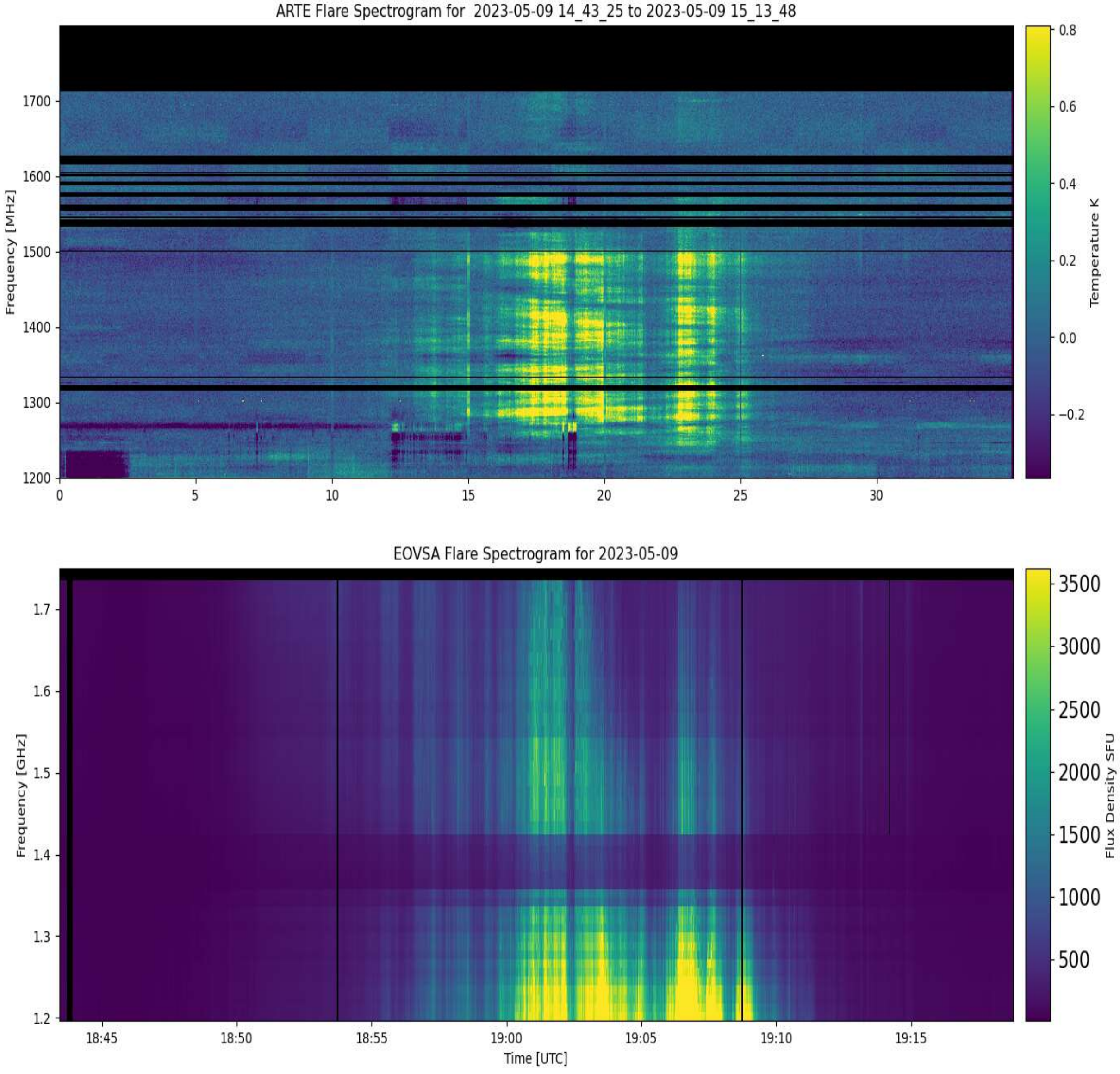
ARTE Flare Spectrogram for 2023-05-09 14_43_25 to 2023-05-09 15_13_48

EOVSA Flare Spectrogram for 2023-05-09

Figure 5.7: Comparison between ARTE & EOVSA flare dynamic spectra

---

[3] `http://ovsa.njit.edu/browser/?suntoday_date=2023-05-09`

The plots shown in 5.8 are referred to as the first solar flare detected by ARTE shown in 5.7. In this way, the power plot corresponds to a 35-minute event duration. This detection was verified with EOVSA flare list information, available on the official website [4].

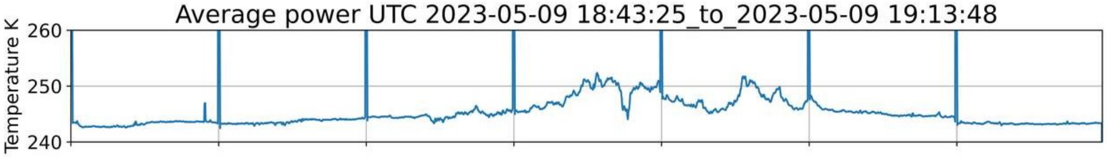

(a) Average power detected by ARTE

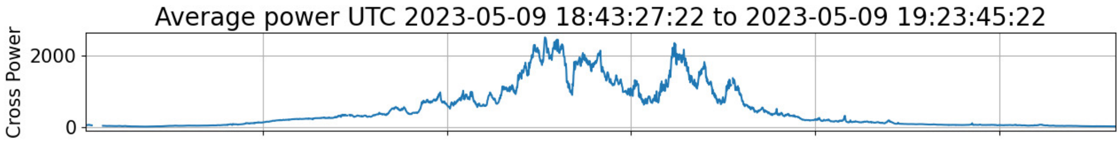

(b) Cross power reported by EOVSA

Figure 5.8: Comparison between the power curves from ARTE and EOVSA

Solar flares detected

In this subsection, four solar flares detected by ARTE are presented and each of these flares are compared with EOVSA data and plotted together. The black lines in the dynamic spectrograms of ARTE data correspond to frequency band flags due to RFI.
These four measurements were made after tracking the sun with a test-tracking Python script. For simplicity, a table shows the main information of each detection:

Date	UTC Time	GOES Class	Position
2024-05-09	17:28:59	X1.1	S17 W28
2024-05-06	18:19:11	C3.7	N24 W44
2024-05-14	16:43:34	X8.8	S18 W89
2024-05-17	17:03:09	C4.4	N25 W43

Table 5.3: Solar flares general information.

---

[4] `http://www.ovsa.njit.edu/wiki/index.php/File:EOVSA_20230509_M4flare_log.png`

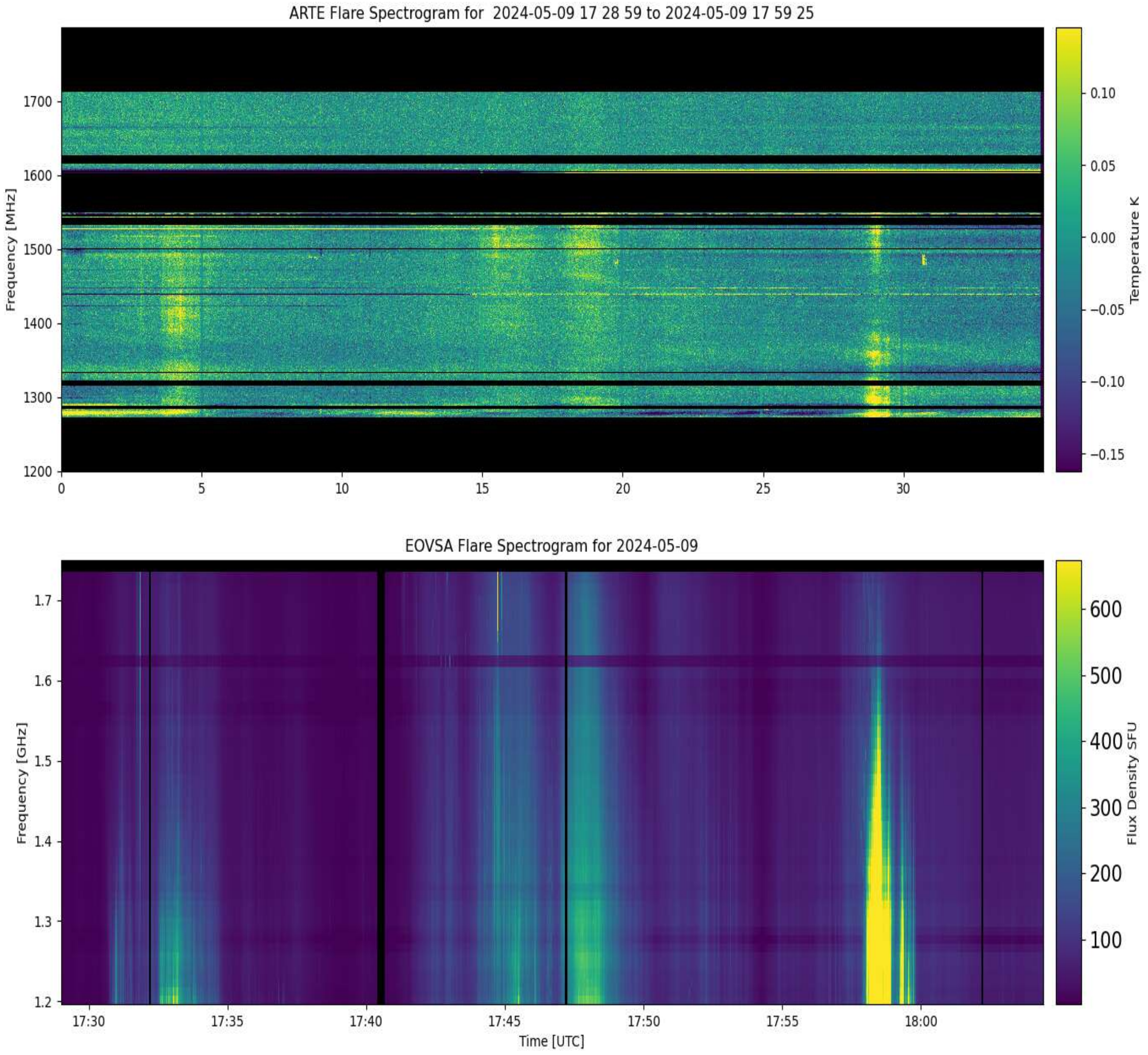

Figure 5.9: Comparison between ARTE & EOVSA flare dynamic spectra on May 09, 2024 at 17:28:59 UTC

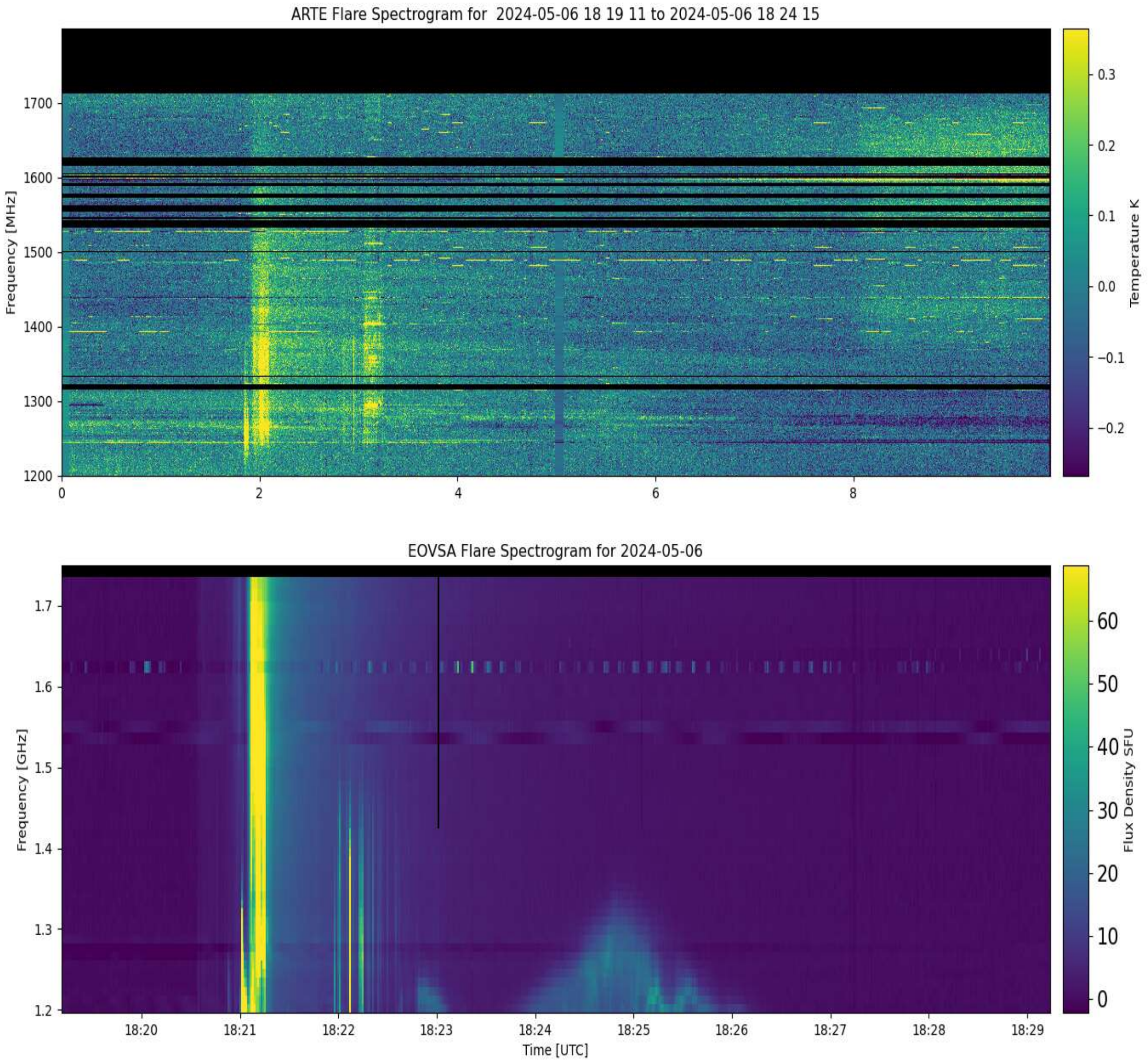

Figure 5.10: Comparison between ARTE & EOVSA flare dynamic spectra on May 06, 2024 at 18:19:11 UTC

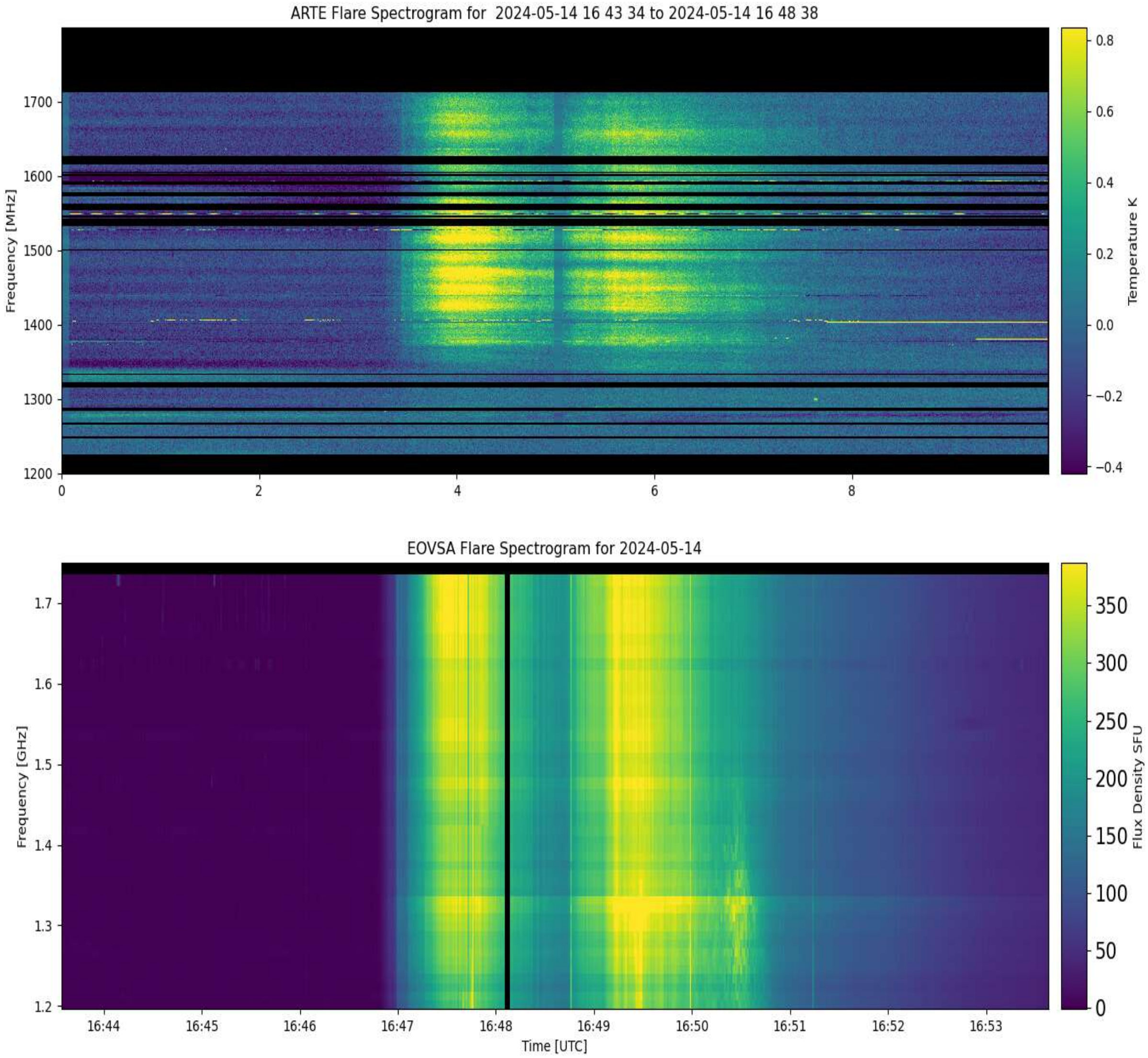

Figure 5.11: Comparison between ARTE & EOVSA flare dynamic spectra on May 06, 2024 at 16:43:34 UTC

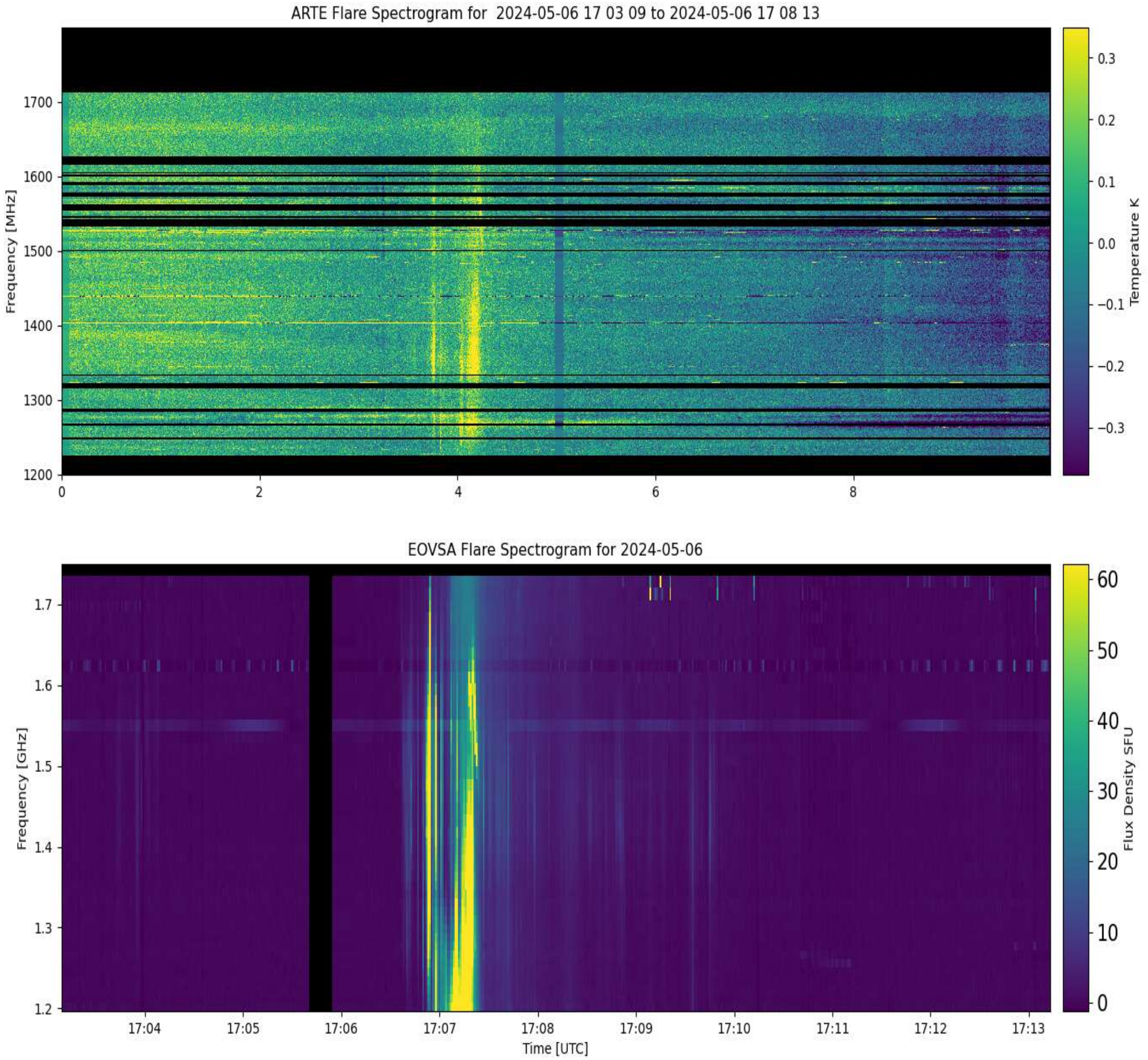

Figure 5.12: Comparison between ARTE & EOVSA flare dynamic spectrogram on May 06, 2024 at 17:03:09 UTC

Chapter 6

Conclusions

In this thesis project, we successfully integrated, assembled, and commissioned the ARTE radio telescope aimed at the detection of fast radio bursts (FRBs) originating within the Milky Way.

A hot-ambient calibration system was developed by utilizing a conventional Agilent 364B noise source. Additionally, a custom noise source was fabricated and calibrated to operate within the parameters obtained from the mentioned commercial noise source.

Regarding the microwave receiver, it was determined to relocate the ULN amplifier (ZX60-P33ULN+). This decision was made by the final system configuration, where the microwave receiver's antenna is located at a distance greater than eight meters, necessitating the use of a twelve-meter-long SMA cable. To prevent a decrease in sensitivity, it was decided to position the first amplifier of each receiver's chain in the ground plane of the main antenna.

Due to the intermodulation distortion within the chains, it was concluded that the final amplifier in the chain (ZX60-2534MA+) was operating in the saturation zone at certain times. Therefore, it was decided to add 20 dB attenuation just before the final amplifier.

Additionally, due to the cross-talk identified between the microwave receiver amplification chains, a decision was made to isolate them in separate aluminum enclosures. These chains were subsequently characterized, resulting in phase imbalances of less than ± 5 degrees in the bandpass between chains as is shown in Chapter3, amplitude imbalances of ± 0.5 dB, and noise temperatures on the order of ~ 200 K.

Post-processing data algorithms were implemented to analyze the spectra stored every ten milliseconds, including calibration, baseline removal, and the final generation of spectrograms with absolute power scaling.

Synthetic FRBs were injected, both into the antenna and directly into the data file. In both scenarios, the signals could be distinguished in the majority of the events. The results of this measurement and deepest analysis are reported in [38].

Due to the undesired presence of RFI in ARTE's operational band, it became necessary to construct two Faraday cages to isolate the system from RFI. Additionally, the equipment (i.e., microwave receiver, power supply, ROACH, and router) had to be relocated to a special room, which was shielded by covering its walls with aluminum foil.

Regarding the detections, periodic artifacts associated with RFI were detected, introduced by cell phones with UP-Link signals within ARTE's operational band. The presence of GPS signals around $\sim$ 1.4 GHz was identified. Several events around $\sim$ 1.7 GHz were observed, which were associated with transits of various weather satellites. Once detected, these transits were predicted using the Orbitron software to classify them. Synthetic Aperture Radars (SAR) were also detected, among other signals.

Finally, the first astronomical source was detected to be a solar flare. This flare was observable both in the dynamic spectra and in the total power curve. The signal was compared against the data from the EOVSA observations, and ARTE detections were consistent with sensitivity. As it was calculated in Chapter 3 ARTE should be sensitive to signals over 164.3 kJy and the minimum solar flare detected has a spectral flux density lower than 200 kJy, so it's consistent reported sensitivity.

6.1 Future work

For future work a range of improvements are proposed, including the replacement of certain hardware components that, while functioning as intended, could enhance their performance. Additionally, future tasks are mentioned that were not fully implemented during this thesis.

1. Replace the reference antenna with one with a higher gain towards the horizon, so to increase its sensitivity to RFI.
2. Track the Galaxy using previously developed code. Three brief scripts are appended in annexes to make simple moves with the mount, the second for tracking the sun for a while and the third for tracking the Milky Way center having elevation and lap restrictions. For more details about the telescope control see [35].
3. Dump detections to disk. To achieve this, it is necessary to set the detection thresholds for the eleven implemented dedispersers, based on analysis of the stored data. Utilize the previously implemented RFI ranking to eliminate contaminated data.
4. Post-process the data using available software and compare the results with the ARTE's algorithm. In particular, the existing software is PRESTO, primarily designed to search pulsars [39].
5. Enhance the cooling system, to mitigate the RFI and improve the cooling system efficiency.
6. Implement a second receiver at Santa Martina Observatory to validate detection and discard RFI.
7. Implement and execute the DoA detection algorithm.
8. Duplicate receiver chains and back-end to operate with dual polarization.

Bibliography

[1] C. Bochenek, D. McKenna, K. Belov, J. Kocz, S. Kulkarni, J. Lamb, V. Ravi, and D. Woody, "Stare2: Detecting fast radio bursts in the milky way," *Publications of the Astronomical Society of the Pacific*, vol. 132, p. 034202, 03 2020.

[2] http://www.ovsa.njit.edu/. Accessed: 2023-10-18.

[3] S. Ocampo, "Sky-proceeding signals and observations analysis," tech. rep., Universidad de Chile, 2023.

[4] C. Balanis, *Advanced Engineering Electromagnetics*. CourseSmart Series, Wiley, 2012.

[5] D. Gallardo, "Diseño y Medición de un Arreglo de Antenas Para la Detección de FRBs Galácticos," tech. rep., Universidad de Chile, 2023.

[6] https://www.mouser.com/datasheet/2/472/200176G-18773.pdf. Accessed: 2024-04-15.

[7] https://www.imagine-it.cl/single-post/2018/10/09/saocom-1a-el-sat Accessed: 2023-11-15.

[8] D. R. Lorimer, M. Bailes, M. A. McLaughlin, D. J. Narkevic, and F. Crawford, "A Bright Millisecond Radio Burst of Extragalactic Origin," *Science*, vol. 318, p. 777, Nov. 2007.

[9] https://www.frbcat.org/. Accessed: 2024-04-16.

[10] M. Amiri, B. C. Andersen, K. Bandura, S. Berger, M. Bhardwaj, M. M. Boyce, P. J. Boyle, C. Brar, D. Breitman, T. Cassanelli, P. Chawla, T. Chen, J.-F. Cliche, A. Cook, D. Cubranic, A. P. Curtin, M. Deng, M. Dobbs, F. (Adam) Dong, G. Eadie, M. Fandino, E. Fonseca, B. M. Gaensler, U. Giri, D. C. Good, M. Halpern, A. S. Hill, G. Hinshaw, A. Josephy, J. F. Kaczmarek, Z. Kader, J. W. Kania, V. M. Kaspi, T. L. Landecker, D. Lang, C. Leung, D. Li, H.-H. Lin, K. W. Masui, R. Mckinven, J. Mena-Parra, M. Merryfield, B. W. Meyers, D. Michilli, N. Milutinovic, A. Mirhosseini, M. Münchmeyer, A. Naidu, L. Newburgh, C. Ng, C. Patel, U.-L. Pen, E. Petroff, T. Pinsonneault-Marotte, Z. Pleunis, M. Rafiei-Ravandi, M. Rahman, S. M. Ransom, A. Renard, P. Sanghavi, P. Scholz, J. R. Shaw, K. Shin, S. R. Siegel, A. E. Sikora, S. Singh, K. M. Smith, I. Stairs, C. M. Tan, S. P. Tendulkar, K. Vanderlinde, H. Wang, D. Wulf, and A. V. Zwaniga, "The first chime/frb fast radio burst catalog," *The Astrophysical Journal Supplement Series*, vol. 257, p. 59, Dec. 2021.

[11] E. Petroff, J. Hessels, and D. Lorimer, "Fast radio bursts," *The Astronomy and Astrophysics Review*, vol. 27, 05 2019.

[12] C.-H. Niu, K. Aggarwal, D. Li, X. Zhang, S. Chatterjee, C.-W. Tsai, W. Yu, C. J. Law, S. Burke-Spolaor, J. M. Cordes, Y.-K. Zhang, S. K. Ocker, J.-M. Yao, P. Wang, Y. Feng, Y. Niino, C. Bochenek, M. Cruces, L. Connor, J.-A. Jiang, S. Dai, R. Luo, G.-D. Li, C.-C. Miao, J.-R. Niu, R. Anna-Thomas, J. Sydnor, D. Stern, W.-Y. Wang, M. Yuan, Y.-L. Yue, D.-J. Zhou, Z. Yan, W.-W. Zhu, and B. Zhang, "A repeating fast radio burst associated with a persistent radio source," *Nature*, vol. 606, pp. 873–877, jun 2022.

[13] NASA Citizen Scientists, "Introduction to the electromagnetic spectrum." `http://science.nasa.gov/ems/01_intro`. Accessed: 2023-9-26.

[14] T. L. Wilson, K. Rohlfs, and S. Hüttemeister, *Tools of radio astronomy.* Springer, 6 ed., 2013.

[15] M. D.R.Lorimer, *Handbook of pulsar astronomy.* Cambridge University, 205.

[16] A. Lyne and F. Graham-Smith, *3 Telescopes and techniques*, p. 27–48. Cambridge Astrophysics, Cambridge University Press, 2012.

[17] W. Liu, Q. Meng, C. Wang, C. Zhou, S. Yao, and I. Tariq, "A real-time, pipelined incoherent dedispersion method and implementation in fpga," *Publications of the Astronomical Society of the Pacific*, vol. 134, p. 015008, jan 2022.

[18] F. A. Curotto, "Design, implementation and characterization of a radio frequency interference digital adaptive filter using a field-programmable gate array," Master's thesis, Universidad de Chile, 2019.

[19] https://chime-experiment.ca/en. Accessed: 2023-10-12.

[20] N. Gohar and C. Flynn, "Detecting FAST RADIO BURSTS in the MILKY WAY," *Monthly Notices of the Royal Astronomical Society*, vol. 509, pp. 5265–5274, nov 2021.

[21] L. Connor, K. A. Shila, S. R. Kulkarni, J. Flygare, G. Hallinan, D. Li, W. Lu, V. Ravi, and S. Weinreb, "Galactic radio explorer: An all-sky monitor for bright radio bursts," *Publications of the Astronomical Society of the Pacific*, vol. 133, p. 075001, July 2021.

[22] http://www.gmrt.ncra.tifr.res.in/. Accessed: 2023-10-12.

[23] V. R. Marthi, T. Gautam, D. Z. Li, H.-H. Lin, R. A. Main, A. Naidu, U.-L. Pen, and R. S. Wharton, "Detection of 15 bursts from the fast radio burst 180916.J0158+65 with the upgraded Giant Metrewave Radio Telescope," *Monthly Notices of the Royal Astronomical Society: Letters*, vol. 499, pp. L16–L20, 09 2020.

[24] D. J. Griffiths, *Introduction to electrodynamics; 4th ed.* Boston, MA: Pearson, 2013. Republished by Cambridge University Press in 2017.

[25] W. L. Stutzman and G. A. Thiele, *Antenna Theory and Design.* John Wiley Sons, 1998.

[26] IEEE, "Ieee standard definitions of terms for antennas," *IEEE Std 145-1993*, pp. 1–32, 1993.

[27] D. M. Pozar, *Microwave engineering.* John wiley & sons, 2012.

[28] D. Gallardo, R. Finger, F. Solis, D. Monasterio, S. Jorquera, J. Pizarro, J. Riquelme, F. Curotto, F. Pizarro, and L. Bronfman, "An ultra-wideband dual polarization antenna array for the detection and localization of bright fast radio transients in the milky way," *Journal of Astronomical Instrumentation*, vol. 0, no. ja, p. null, 0.

[29] M. Prieto, "Diseno, implementacion y caracterizacion de un receptor astronomico de microondas para la deteccion de rafagas rapidas de radio (frb) en la via lactea," B.S. Thesis, Universidad de Chile, 2021.

[30] https://www.minicircuits.com/pdfs/ZX60-2534MA+.pdf. Accessed: 2024-04-15.

[31] https://www.minicircuits.com/pdfs/ZEQ-8-222S+.pdf. Accessed: 2024-04-15.

[32] https://www.minicircuits.com/pdfs/ZX60-P33ULN+.pdf. Accessed: 2024-04-15.

[33] https://www.testequipmenthq.com/datasheets/Keysight-346B-Datasheet.pdf. Accessed: 2024-04-15.

[34] D. Bravo, "Design, implementation and testing of a real-time electromagnetic interference detector and classifier for the five-hundred-meter aperture spherical telescope (fats)," Master's thesis, Universidad de Chile, 2021.

[35] https://github.com/sebajor/ARTE-control. Accessed: 2024-01-11.

[36] https://www.russianspaceweb.com/meteor-m2-1.html. Accessed: 2023-11-15.

[37] https://eospso.nasa.gov/missions/noaa-poes. Accessed: 2023-11-15.

[38] S. Verwer, "Developing an algorithm for the detection of fast radio bursts," tech. rep., 2023.

[39] https://github.com/scottransom/presto. Accessed: 2024-04-16.

ANNEXES

Annex A Moves with LX85 using PyIndi and KStars

The following Python script is the simplest way to start to control the German Equatorial Mount LX85.

```
#################################################################################
# Before running this Python script it's necessary the appropriate configuration
# of KStars desktop application, explained in detail in the ARTE manual.
#################################################################################

# imports
import time, datetime, math
import PyIndi

# parameters
INDI_SERVER_HOST="localhost"
INDI_SERVER_PORT=7624
TELESCOPE_DEVICE="LX200 Autostar"#"EQMod Mount"

# client definition
indiclient = PyIndi.BaseClient()
indiclient.setServer(INDI_SERVER_HOST, INDI_SERVER_PORT)
indiclient.watchDevice(TELESCOPE_DEVICE)
device=None

#try to connect to the server
print("Connecting server "+indiclient.getHost()+":"+str(indiclient.getPort()))
serverconnected=indiclient.connectServer()
if(serverconnected):
    print('Server successfully connected')
else:
    raise Exception('Cant connect to the server')

#try to connect to the de device
device = indiclient.getDevice(TELESCOPE_DEVICE)
if not(device):
    device=indiclient.getDevice(TELESCOPE_DEVICE)
    while not(device):
        print("Trying to get device "+TELESCOPE_DEVICE)
        time.sleep(0.5)
        device=indiclient.getDevice(TELESCOPE_DEVICE)
```

```
print("Got device "+TELESCOPE_DEVICE)

if not(device.isConnected()):
    device_connect=device.getSwitch("CONNECTION")
    while not(device_connect):
        print("Trying to connect device "+TELESCOPE_DEVICE)
        time.sleep(0.5)
        device_connect=device.getSwitch("CONNECTION")
if not(device.isConnected()):
    device_connect[0].s=PyIndi.ISS_ON  # the "CONNECT" switch
    device_connect[1].s=PyIndi.ISS_OFF # the "DISCONNECT" switch
    indiclient.sendNewSwitch(device_connect)
if(device.isConnected()):
    print('Device successfully connected')
time.sleep(0.5)

if(not device.isConnected()):
    indiclient.disconnectServer()
    server_proc.terminate()
    raise Exception('Cant connect to the mount!')

tel_on_coord_set = device.getSwitch("ON_COORD_SET")

##set the parameters
tel_on_coord_set[0].s=PyIndi.ISS_ON  # TRACK
tel_on_coord_set[1].s=PyIndi.ISS_OFF # SLEW
tel_on_coord_set[2].s=PyIndi.ISS_OFF # SYNC
indiclient.sendNewSwitch(tel_on_coord_set)

##get coordinates
radec=device.getNumber("EQUATORIAL_EOD_COORD")


radec[0].value = radec[0].value +10.01
radec[1].value = radec[1].value +3
indiclient.sendNewNumber(radec)
```

Annex B Tracking the Sun with LX85 using PyIndi and KStars

The following Python script is for tracking the sun for a particular time, controlling the German Equatorial Mount LX85.

```
##################################################################################
# Before running this Python script it's necessary the appropriate configuration
# of KStars desktop application, explained in detail in the ARTE manual.
##################################################################################
# imports
import time, datetime, math
import PyIndi
import astropy.coordinates as coord
from astropy.time import Time
import numpy as np

## test parameters
refresh_time = 2    ##minutes
test_time = 3       ##hrs
iters = test_time*60//refresh_time
data = np.zeros(5)

filename = "logger_sun_pos_date_version"
##create log file
f = open(filename, 'w')
f.close()

# parameters
INDI_SERVER_HOST="localhost"
INDI_SERVER_PORT=7624
TELESCOPE_DEVICE="LX200 Autostar"#"EQMod Mount"

# client definition
indiclient = PyIndi.BaseClient()
indiclient.setServer(INDI_SERVER_HOST, INDI_SERVER_PORT)
indiclient.watchDevice(TELESCOPE_DEVICE)
device=None

#try to connect to the server
print("Connecting server "+indiclient.getHost()+":"+str(indiclient.getPort()))
serverconnected=indiclient.connectServer()
if(serverconnected):
    print('Server successfully connected')
else:
    raise Exception('Cant connect to the server')

#try to connect to the de device
device = indiclient.getDevice(TELESCOPE_DEVICE)
if not(device):
    device=indiclient.getDevice(TELESCOPE_DEVICE)
    while not(device):
        print("Trying to get device "+TELESCOPE_DEVICE)
        time.sleep(0.5)
        device=indiclient.getDevice(TELESCOPE_DEVICE)
```

```
print("Got device "+TELESCOPE_DEVICE)

if not(device.isConnected()):
    device_connect=device.getSwitch("CONNECTION")
    while not(device_connect):
        print("Trying to connect device "+TELESCOPE_DEVICE)
        time.sleep(0.5)
        device_connect=device.getSwitch("CONNECTION")
if not(device.isConnected()):
    device_connect[0].s=PyIndi.ISS_ON  # the "CONNECT" switch
    device_connect[1].s=PyIndi.ISS_OFF # the "DISCONNECT" switch
    indiclient.sendNewSwitch(device_connect)
if(device.isConnected()):
    print('Device successfully connected')
time.sleep(0.5)

if(not device.isConnected()):
    indiclient.disconnectServer()
    server_proc.terminate()
    raise Exception('Cant connect to the mount!')
######################################################

## GEOGRAPHIC_COORD reconfirmation
geographic_pos = device.getNumber("GEOGRAPHIC_COORD")
geographic_pos[0].value   # LAT Site latitude (-90 to +90), degrees +N
geographic_pos[1].value   # LONG Site longitude (0 to 360), degrees +E
geographic_pos[2].value   # ELEV Site elevation, meters
indiclient.sendNewNumber(geographic_pos)

## UTC time verification
utc_time = device.getText("TIME_UTC")
utc_time[0].text
utc_time[1].text
print(utc_time[0].text)
print(utc_time[1].text)
indiclient.sendNewText(utc_time)

########################################################
####### SUN parameters for tracking  ###################
for i in range(iters):

    t = Time.now()
    sun_pos = coord.get_sun(t)
    RA= sun_pos.ra.hour
    DEC = sun_pos.dec.deg

    # Now let's make a go to the sun
    # Beware that ra/dec is in decimal hours/degrees
    sun = {'ra': RA, 'dec': DEC }
    ## Save the data in the previous np.array
    data[0] = time.time()
    data[1] = RA
    data[2] = DEC

    # We want to set the ON_COORD_SET switch to engage tracking after goto
    # device.getSwitch is a helper to retrieve a property vector
```

```
    tel_on_coord_set = device.getSwitch("ON_COORD_SET")
    while not(tel_on_coord_set):
        time.sleep(0.5)
        tel_on_coord_set = device.getSwitch("ON_COORD_SET")
    # The order below is defined in the property vector,
    # look at the standard Properties page
    tel_on_coord_set[0].s=PyIndi.ISS_ON   # TRACK
    tel_on_coord_set[1].s=PyIndi.ISS_OFF # SLEW
    tel_on_coord_set[2].s=PyIndi.ISS_OFF # SYNC
    indiclient.sendNewSwitch(tel_on_coord_set)
    # We set the desired coordinates
    radec = device.getNumber("EQUATORIAL_EOD_COORD")
    print("Current position from device :\n"+"RA: {:.4f} DEC: {:.4f}"
                        .format(radec[0].value, radec[1].value))
    radec[0].value = sun['ra']
    radec[1].value = sun['dec']
    indiclient.sendNewNumber(radec)
    print("Current position for track :\n"+"RA: {:.4f} DEC: {:.4f}"
                        .format(radec[0].value, radec[1].value))
    while not(radec):
        time.sleep(0.5)
        radec = device.getNumber("EQUATORIAL_EOD_COORD")
    radec[0].value = sun['ra']
    radec[1].value = sun['dec']
    indiclient.sendNewNumber(radec)
    print("Current position :\n"+"RA: {:.4f} DEC: {:.4f}"
                        .format(radec[0].value, radec[1].value))
    # and wait for the scope has finished moving
    data[3] = radec[0].value
    data[4] = radec[1].value
    while (radec.getState()==PyIndi.IPS_BUSY):
        print(radec.getState())
        print("Scope Moving ", radec[0].value, radec[1].value)
        time.sleep(2)

    with open(filename, 'ab') as f:
        f.write(b'\r\n')
        np.savetxt(f, [data], delimiter=',')

time.sleep(5)
# Try to disconnect from the server
print("Disconnecting server "+indiclient.getHost()+":"+str(indiclient.getPort()))
serverconnected=indiclient.disconnectServer()
```

Annex C Tracking the Milky Way center with LX85 using PyIndi and KStars

The following Python script is for tracking the Milky Way center, for a particular set of restrictions like the elevation, and the number of azimuth laps to protect the wires tangled and projected the beam on the Galactic plane. Controlling the German Equatorial Mount LX85.
An important thing to mention, this is the main code and we call many functions from coords.py Python scripts saved in the following path, on ARTE's computer.
Path: `Workspace/ARTE-control/tracking_fran/src/coords.py`.

```
# imports
import os
import glob
import importlib

import time, datetime, math
import PyIndi
import numpy as np
from astropy import units as u
from astropy.time import Time
from astropy.coordinates import SkyCoord, EarthLocation, AltAz

import src.logging
importlib.reload(src.logging)
from src.logging import *

import src.coords
importlib.reload(src.coords)
from src.coords import *

# loggin directory
directory = 'tracking_logs'

# absolute lap
min_abs_lap = 0 * u.deg
max_abs_lap = 360 * u.deg

# indi parameters
INDI_SERVER_HOST="localhost"
INDI_SERVER_PORT=7624
TELESCOPE_DEVICE="LX200 Autostar"#"EQMod Mount"

# client definition
indiclient = PyIndi.BaseClient()
indiclient.setServer(INDI_SERVER_HOST, INDI_SERVER_PORT)
indiclient.watchDevice(TELESCOPE_DEVICE)
device=None

# server connection
print("Connecting server "+indiclient.getHost()+":"+str(indiclient.getPort()))
serverconnected=indiclient.connectServer()
if(serverconnected):
    print('Server successfully connected')
else:
    raise Exception('Cant connect to the server')
```

```
#try to connect to the de device
device = indiclient.getDevice(TELESCOPE_DEVICE)
if not(device):
    device=indiclient.getDevice(TELESCOPE_DEVICE)
    while not(device):
        print("Trying to get device "+TELESCOPE_DEVICE)
        time.sleep(0.5)
        device=indiclient.getDevice(TELESCOPE_DEVICE)
print("Got device "+TELESCOPE_DEVICE)

if not(device.isConnected()):
    device_connect=device.getSwitch("CONNECTION")
    while not(device_connect):
        print("Trying to connect device "+TELESCOPE_DEVICE)
        time.sleep(0.5)
        device_connect=device.getSwitch("CONNECTION")
if not(device.isConnected()):
    device_connect[0].s=PyIndi.ISS_ON  # the "CONNECT" switch
    device_connect[1].s=PyIndi.ISS_OFF # the "DISCONNECT" switch
    indiclient.sendNewSwitch(device_connect)
if(device.isConnected()):
    print('Device successfully connected')
time.sleep(0.5)

if(not device.isConnected()):
    indiclient.disconnectServer()
    server_proc.terminate()
    raise Exception('Cant connect to the mount!')

# ON_COORD_SET initial setup
telescope_on_coord_set = device.getSwitch("ON_COORD_SET")
while not(telescope_on_coord_set):
    time.sleep(0.5)
    telescope_on_coord_set = device.getSwitch("ON_COORD_SET")

# Galactic Center initial values
ref = 0*u.deg
Altitud, Azimuth, MW_centre, MW_offset = get_GC_coords()

#Get last absolute_lap
if directory_exists(directory):
    last_filename = sorted(os.listdir(directory))
else:
    os.mkdir(directory)
    last_filename = sorted(os.listdir(directory))

first_iteration = False

if len(last_filename) == 0:
    print('no first file created... skipping')
    absolute_lap = 0* u.deg
    first_iteration = True

    current_ra, current_dec, current_alt, current_az = get_current_coords(device)
    latest = generate_tracking_log_line(current_ra,
```

```
                                        current_dec,
                                        current_alt,
                                        current_az,
                                        absolute_lap)
    write_log(directory, get_log_file_name(directory), latest)


else:
    if load_last_line_from_log(os.path.join(directory,last_filename[-1])) == None:
        print('no last line recorded... please make sure everything is ok')
        absolute_lap = 0* u.deg

        current_ra, current_dec, current_alt, current_az = get_current_coords(device)
        latest = generate_tracking_log_line(current_ra,
                                            current_dec,
                                            current_alt,
                                            current_az,
                                            absolute_lap)
        write_log(directory, get_log_file_name(directory), latest)
    else:
        absolute_lap = load_last_line_from_log(os.path.join(directory,last_filename[-1]))[-1]

        if check_abs_lap(absolute_lap, min_abs_lap, max_abs_lap) == -1:
            reset_abs_lap(device, absolute_lap)

while(device.isConnected()):

    Altitud, Azimuth, MW_centre, MW_offset = get_GC_coords()

    if Altitud > ref:
        print('MW observable')

        ##### Checks absolute lap
        if check_abs_lap(absolute_lap, min_abs_lap, max_abs_lap) == -1:
            print('absolute lap overlap\n')
            reset_abs_lap(device, absolute_lap)

        ##### Moving

        Altitud, Azimuth, MW_centre, MW_offset = get_GC_coords()

        print(f'GC coords:\n
                RA: {MW_centre["ra"]}\n
                DEC: {MW_centre["dec"]}\n
                Alt: {Altitud}\n
                Az:{Azimuth}\n\n
                Sending coords...')

        telescope_on_coord_set[0].s = PyIndi.ISS_ON  # TRACK we want track de MW
        telescope_on_coord_set[1].s = PyIndi.ISS_OFF # SLEW
        telescope_on_coord_set[2].s = PyIndi.ISS_OFF # SYNC
        indiclient.sendNewSwitch(telescope_on_coord_set)

        telescope_radec = device.getNumber("EQUATORIAL_EOD_COORD")

        telescope_radec = device.getNumber("EQUATORIAL_EOD_COORD")
```

```
        telescope_radec[0].value = MW_centre['ra']
        telescope_radec[1].value = MW_centre['dec']
        indiclient.sendNewNumber(telescope_radec)
        print("Current position :\n"+"RA: {:.4f} DEC: {:.4f}".format(telescope_radec[0].value,
                                                                    telescope_radec[1].value))
        # and wait for the scope has finished moving

        while not(telescope_radec):
            time.sleep(0.5)
            telescope_radec = device.getNumber("EQUATORIAL_EOD_COORD")
            telescope_radec[0].value = MW_centre['ra']
            telescope_radec[1].value = MW_centre['dec']
            indiclient.sendNewNumber(telescope_radec)
            print("Current position :\n"+"RA: {:.4f} DEC: {:.4f}".format(telescope_radec[0].value,
                                                                        telescope_radec[1].value))
            # and wait for the scope has finished moving
        while (telescope_radec.getState()==PyIndi.IPS_BUSY):
            print("Scope Moving ", telescope_radec[0].value, telescope_radec[1].value)
            time.sleep(1)

        ##### Logging
        print('logging...')
        prev_date, prev_ra, prev_dec, prev_alt, prev_az, prev_abs_lap = load_last_line_from_log(
                                                                            os.path.join(
                                                                                directory,
                                                                                get_log_filenames(
                                                                                    directory)[-1]))
        current_ra, current_dec, current_alt, current_az = get_current_coords(device)

        absolute_lap = absolute_lap + current_az - prev_az

        latest = generate_tracking_log_line(current_ra,
                                            current_dec,
                                            current_alt,
                                            current_az,
                                            absolute_lap)
        write_log(directory, get_log_file_name(directory), latest)
        time.sleep(3)

    if not(Altitud > ref):
        print(Altitud.to_value(u.deg))
        # the order below is defined in the property vector, look at the standard Properties
        # TRACK
        telescope_on_coord_set[0].s = PyIndi.ISS_OFF
        # SLEW we want to slew to a coordinate and stop upon receiving coordinates.
        telescope_on_coord_set[1].s = PyIndi.ISS_ON
        # SYNC
        telescope_on_coord_set[2].s = PyIndi.ISS_OFF
        indiclient.sendNewSwitch(telescope_on_coord_set)

        # We set the desired coordinates
        telescope_radec =  device.getNumber("EQUATORIAL_EOD_COORD")
        while not(telescope_radec):
            time.sleep(0.5)
            telescope_radec = device.getNumber("EQUATORIAL_EOD_COORD")
            telescope_radec[0].value = MW_offset['ra']
```

```
            telescope_radec[1].value = MW_offset['dec']
            indiclient.sendNewNumber(telescope_radec)
            print("Current position :\n"+"RA: {:.4f} DEC: {:.4f}".format(telescope_radec[0].value,
                                                                        telescope_radec[1].value))
        # and wait for the scope has finished moving
        while (telescope_radec.getState()==PyIndi.IPS_BUSY):
            print("Scope Moving ", telescope_radec[0].value, telescope_radec[1].value)
            time.sleep(2)

print('device disconnected')


#imports
from astropy import units as u
from astropy.time import Time
from astropy.coordinates import SkyCoord, EarthLocation, AltAz
import astropy.coordinates as coord

import numpy as np
import math
import importlib

import logging
importlib.reload(logging)
from logging import *

directory = 'tracking_logs'

def get_current_coords(device):
    radec =  device.getNumber("EQUATORIAL_EOD_COORD")
    ra = radec[0].value
    dec = radec[1].value
    radec = SkyCoord(ra=ra*u.hour, dec=dec*u.deg, frame='icrs')
    # Calan GEOGRAPHIC_COORD
    calan_obs = EarthLocation(lat=-33.3961*u.deg, lon=-70.537*u.deg, height=867*u.m)
    now = Time.now()
    altaz_frame = AltAz(obstime=now,location=calan_obs)
    altaz = radec.transform_to(altaz_frame)
    alt = altaz.alt
    az = altaz.az
    return ra * u.hour, dec * u.deg, alt, az

def check_abs_lap(absolute_lap, min_abs_lap, max_abs_lap):
    if type(absolute_lap) != float:
        return "no record"
    if absolute_lap < min_abs_lap or absolute_lap > max_abs_lap:
        print('absolute lap out of bounds... resetting to 0')
        return -1
    else:
        return 0

def reset_abs_lap(device, absolute_lap):
    #park ...
    absolute_lap = 0 * u.deg
    ra, dec, alt, az = get_current_coords(device)
    latest = generate_tracking_log_line(ra, dec, alt, az, absolute_lap)
```

```
    write_log(directory, get_log_file_name(directory), latest)
    print('absolute lap reset to 0... antenna parked')

def get_GC_coords():
    GC = SkyCoord.from_name('Galactic Center')
    A = GC.galactic.l.value # lon 0 360
    D = GC.galactic.b.value # lat -90 90
    ra_hr   = GC.ra.hour
    dec_deg  = GC.dec.deg
    MW_centre = {'ra': ra_hr, 'dec': dec_deg }

    dec_deg2  = GC.dec.deg + 5
    MW_offset = {'ra': dec_deg2, 'dec': dec_deg2 }
    ############################
    a = 73.0/2
    be = 26.0/2
    epsilon = 0.01 #0.01

    # define ellipse on the tangent plane
    # ellipse with center coordinates (A,D)
    # (A,D) galactic longitude and latitude
    anxi = np.arange(A-a, A+a, epsilon)
    aneta = be * np.sqrt(1 - (anxi-A)**2 / a**2)

    angle_xi =  np.concatenate((anxi, anxi))
    angle_eta = D + np.concatenate((-aneta, aneta))

    XI = np.tan(angle_xi / 180.0 * np.pi)   #rad gal
    ETA = np.tan(angle_eta / 180.0 * np.pi) #rad gal

    for xi, eta in zip(XI, ETA):

        alpha = np.arctan( xi /( np.cos(D/ 180.0 * np.pi) - eta * np.sin(D/ 180.0 * np.pi)) ) + ...
        A/ 180.0 * np.pi
        delta = np.arctan((eta * np.cos(D/ 180.0 * np.pi) + np.sin(D/ 180.0 * np.pi)) * ...
        np.sin(alpha - A/ 180.0 * np.pi) / xi)

        alpha_d = math.degrees(alpha) #deg gal
        delta_d = math.degrees(delta) #deg gal

        gal = SkyCoord(l = alpha_d*u.deg, b = delta_d*u.deg, frame ='galactic')
        eq = gal.fk5
        #Calan GEOGRAPHIC_COORD
        calan_obs = EarthLocation(lat=-33.3961*u.deg, lon=-70.537*u.deg, height=867*u.m)
        now = Time.now()
        altaz_frame = AltAz(obstime=now,location=calan_obs)
        eq_to_altaz = eq.transform_to(altaz_frame)

        Altitud = eq_to_altaz.alt
        Azimuth = eq_to_altaz.az
        return Altitud, Azimuth, MW_centre, MW_offset
```